UNIVERSITÉ DU QUÉBEC

MÉMOIRE

PRÉSENTÉ À

L'UNIVERSITÉ DU QUÉBEC À CHICOUTIMI

COMME EXIGENCE PARTIELLE

DE LA MAÎTRISE EN INGÉNIERIE

PAR

PASCAL GAUTHIER, B. Ing.

CORROSION BEHAVIOUR STUDY OF THE FORGED

AA6082 ALUMINUM ALLOY FROM DIFFERENT FEEDSTOCK

DÉCEMBRE 2010

RÉSUMÉ

Des essais préliminaires industriels de forgeage et de nettoyage du lubrifiant à la soude caustique effectués sur des lopins coulé-homogénéisé avaient soulevé certaines interrogations sur la résistance à la corrosion de ce nouveau matériau comparativement au matériel extrudé traditionnellement utilisé. Cette étude en corrosion a pour objectif principal d'assurer la qualité et la possibilité d'utiliser ce matériel comme base pour l'industrie du forgeage. Le comportement en corrosion de l'alliage d'aluminium AA6082 a été étudié par l'utilisation de méthodes comparatives entre le matériel coulé-forgé et extrudé-forgé dans différents états métallurgiques (-T6). La conclusion majeure de cette étude révèle que la différence de susceptibilité en corrosion des deux matériaux n'est pas suffisamment significative pour favoriser un impact négatif sur les produits finaux de forgeage.

Une investigation métallurgique avant et après le forgeage a permis d'identifier des patrons spécifiques de microstructures et des différences chimiques entre les matériaux de base. Cette analyse microstructurale met en perspective deux matériaux qui pourraient avoir des affinités différentes pour le forgeage et leur comportement en corrosion, surtout avec la présence de couches spéciales en surface. Le matériel coulé présente une structure ayant des grains équiaxes et une couche de ségrégation enrichie d'éléments d'alliages tandis que le matériel extrudé expose une structure fibreuse ayant une couche périphérique de gros grains recristallisés. La texture microstructurale allongée pour le matériel coulé-forgé se transforme en une fine microstructure après le traitement thermique -T6. Cette même étape produit des résultats opposés pour le matériel extrudé-forgé en révélant une recristallisation statique qui engendre une structure grossière à gros grains.

Les trois essais caractéristiques en corrosion sur l'alliage d'aluminium AA6082 ont démontré de légères variations concernant les résultats de dégradation mais pas suffisamment pour distinguer un matériel plus résistant que l'autre. L'acquisition des courbes électrochimiques OCP a montré que le temps nécessaire pour

atteindre l'état d'équilibre dans le domaine passif du matériel coulé-forgé était plus long que celui extrudé-forgé après 24 heures d'immersion dans une solution de 3.5% m/v de NaCl. Des essais de polarisation anodique ont permis d'identifier un potentiel de piqûration (E_{pit}) entre -0.63 à -0.54 V/SCE pour toutes les conditions métallurgiques. Le matériel coulé a affiché un phénomène de piqûration continu après avoir atteint le potentiel critique E_{pit}. Par contre, ce même matériel semblait avoir une résistance légèrement supérieure à la piqûration en affichant un potentiel plus noble équivalent à -0.54 V/SCE. Les analyses de microscopie optique sur les spécimens corrodés ont dévoilé un patron de petites piqûres de forme ronde et uniforme pour le matériel coulé-forgé et un aspect asymétrique avec quelques larges piqûres de corrosion pour le matériel extrudé-forgé.

L'analyse d'image quantitative par le logiciel CLEMEX sur les spécimens corrodés par brouillard salin a révélé une surface moins affectée du matériel extrudé-forgé sans traitement thermique comparativement à celui coulé-forgé (13.46% coulé-forgé vs 6.77% extrudé-forgé). Après traitement -T6, les deux matériaux de base ont obtenu des résultats similaires du pourcentage d'aire corrodé (3.62% vs 3.68%). Aucune variation significative en résistance à la fatigue-corrosion n'a été décelée sur les deux types de matériel de base. Dans l'air, les courbe S-N ont affiché deux tendances qui caractérisent chacun des matériaux. Le matériel coulé-forgé a obtenu une meilleure résistance à la fatigue avec de faibles contraintes appliquées, tandis que le matériel extrudé-forgé a révélé une résistance accrue à la fatigue durant l'imposition de contraintes sévères. L'ajout d'un environnement corrosif autour des spécimens a eu comme effet d'abaisser la durée de vie en fatigue d'un facteur $1x10^3$ pour les deux matériaux. L'analyse macroscopique des ruptures a révélé un faciès granuleux et plat pour les échantillons appartenant au matériel coulé-forgé comparativement à d'importantes zone de clivage pour les surfaces du matériel extrudé-forgé. Plusieurs spécimens de fatigue corroboraient la présence d'un mécanisme de propagation par striation avec bandes de cisaillement persistantes. Le facteur additif de corrosion a joué un rôle d'adoucissement des stries de fatigue pour les deux matériaux de forgeage.

SUMMARY

Preliminary forging and caustic cleaning tests were carried out on cast-homogenized materials and raised some further questions on the corrosion resistance of this material compared to the conventional extruded feedstock. This corrosion study serves as a milestone key to ensure the quality and the possibility of using this material as feedstock in the forging industry. The corrosion behavior of the forged-T6 AA6082 aluminum alloy was studied by comparing cast-forged and extruded-forged materials in both forged and aged tempers. The main conclusion of this comparative study is that no significant difference that could have a possible negative impact on the final product has been measured in corrosion susceptibilities between these two forging feedstocks.

A metallographical investigation before and after forging allowed to highlight microstructural patterns and chemical differences between forging feedstocks. The microstructural analysis puts into perspective two materials that could have different affinities to forging and corrosion assessment, especially due to the presence of special layers at the surface. The cast material has an equiaxed grain structure with an enriched surface layer in segregated alloying elements and the extruded material has a fibrous structure having a recrystallized surface layer with a fine grain structure. The elongated texture generated for the cast-forged condition changed to a recrystallized fine microstructure after the T6 heat treatment. This thermal treatment produced an opposite result for the extruded-forged material by revealing a static recrystallization that promotes a coarse grain structure.

Corrosion tests were conducted on the AA6082 aluminum alloy to focus on the susceptibility in corrosion of both forging materials. Three tests show slight variations on the corrosion results but not enough to distinguish a better feedstock material resistance. The OCP curves have shown that the times necessary for a passive state equilibrium of cast-forged materials were longer than those extruded-forged after 24 hours

immersion in a 3.5 w/v% NaCl solution. Similar anodic polarizations of impressed voltage permitted to identify E_{pit} between -0.63 to -0.54 V/SCE for all conditions. Cast feedstock conditions showed a continuous pitting phenomenon after E_{pit}. The cast feedstock T6 condition seemed to have a slightly better pitting resistance when the voltage was applied with the nobler E_{pit} result at -0.54 V/SCE. Optical microscopy analyses revealed uniform round corroded pit patterns for the metallurgically cast-forged conditions and an asymmetrical aspect with large corrosion pits for the extruded-forged material.

Image analyses by the CLEMEX© software on salt sprayed corroded specimens identified a better resistance of the extruded-forged material without subsequent solutionizing and aging heat treatments when compared with the same cast-forged condition (13.46% cast-forged-T6 vs 6.77% extruded-forged-T6). The T6 thermal treatment on both forged materials appears to have obtained the same percentage of area affected by pitting corrosion (3.62% cast-forged-T6 vs 3.68% extruded-forged-T6) in the cabinet exposure test. No significant variation in corrosion-fatigue resistance was identified in the two types of materials. In the air environment, fatigue S-N curves established two cases for both forged materials: the cast-forged material shows a better fatigue resistance at low stresses and the extruded-forged material revealed an improved fatigue resistance during the high stresses applied. In a devastating corrosive environment addition, the corrosion-fatigue test results into a decrease in the number of cycles by a factor of $1x10^3$ on both types of forged-T6 materials.

The macroscopic fatigue fractures analyses revealed flat and grainy facies of cast-forged samples opposed to important cleavage zones for the extruded-forged surfaces. Many fatigue specimens seem to rupture with a striation propagation mechanism with persistent shear bands (PSB). The corrosion factors during fatigue-corrosion tests have an impact on the softening of microscopic fatigue striations for both materials.

ACKNOWLEDGEMENTS

CONTENTS

FIGURE LISTS

TABLE LISTS

1

INTRODUCTION

Improved methods of semi-continuous casting has allowed the availability of small aluminum billets (<152 mm or 6 inches) with a superior surface finish. This material seems to be very promising and has multiple beneficial properties such as a homogeneous fine grain structure with quasi-isotropic deformation behavior to forging. These DC casting technologies perform most of the cooling through direct water quenching, resulting in a shallow sump and a very thin-shelled, uniform-grained billet with excellent surface smoothness. This new development during the solidification process minimizes the outer skin produced (segregation, defects and oxides) on cast aluminum billets where the final forging part must avoid this outer skin to keep an extremely good surface quality. Therefore, with this material it is now possible to go directly to the forging process without using the extrusion process to reduce the diameter and to increase the surface quality of these billets.
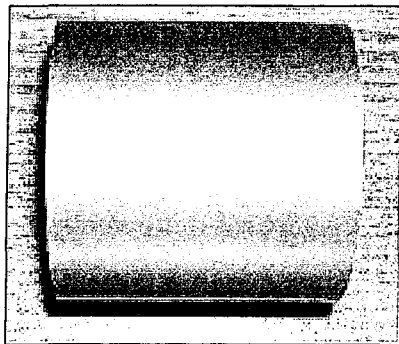
Figure 1.1: High surface quality obtained on 50 mm aluminum cast billets produced by new VDC technologies as forging feedstock [1,2]

Many benefits can be identified by using these casting technologies to produce small aluminum billets as forging feedstock:

- A high cooling rate during solidification that produces a small shell zone on billets;

- A shorter homogenization cycle and faster casting speeds;

- A homogeneous, fine grain structure with tight dimensional tolerances;

- Elimination of most surface defects and production of a low surface roughness;

- Quasi-isotropic deformation behavior for further thermomechanical processes use;

- Small shell zone allowing faster extrusion speeds.

This new method allows the manufacturing of small ready-to-forge cast billets without any intermediate processes *(Figure 1.2a vs 1.2b)*. Transitional processes such as machining or extrusion were previously used to reduce the billet diameter and to ensure a smooth surface.
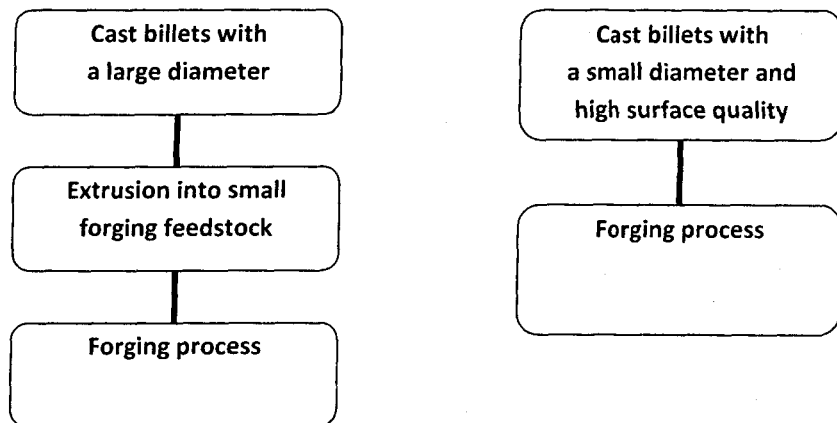
a) Traditional way to produce forging feedstock

b) New technological way to produce forging feedstock

Figure 1.2: Technological flowsheet paths to produce aluminum billets as forging feedstock

1.1. Investigation on surface anomalies of directly cast-forged products

Initial forging trials were done by Rio Tinto Alcan with the cast aluminum feedstock to evaluate its general formability and resulting properties *(see example of an automotive suspension arm at Figure 1.3)*.
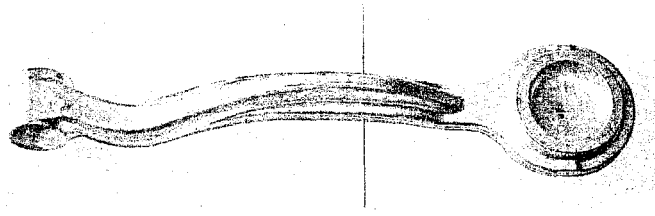
Figure 1.3: AA6082 aluminum suspension arm forged with the cast feedstock material in industrial trials (Courtesy of Rio Tinto ALCAN).

After hot forging, and due to the presence of graphite used as lubricant during the deformation process, a cleaning procedure must be performed on the forged specimens. Chemical solutions used to clean the residual graphite from the aluminum specimens are normally solvents, alkaline and acidic products. Specific cleaning steps (pickling) of forged specimens include a first stage of degreasing followed by a series of sodium hydroxide (NaOH 10% w/v), water cleaning, concentrated nitric acid (HNO_3) and hot water bath immersions. During this process, specific areas on parts were preferentially attacked by creating irregular brightness from the bottom at some places *(Figure 1.4)*.

Forged area with a bright metallic gray color

Forged area with a matt gray color
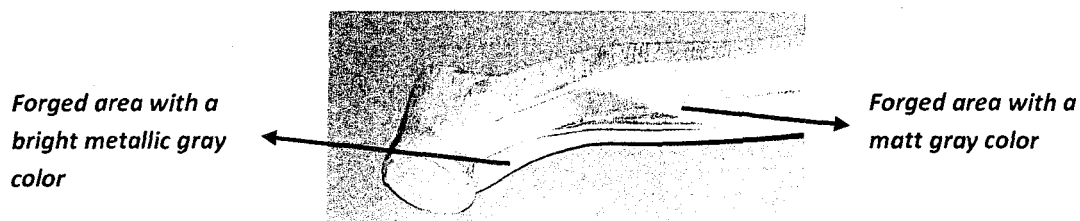
Figure 1.4: Abnormal color tints identified on industrial parts that were forged directly from AA6082 aluminum cast material (Courtesy of Rio Tinto Alcan).

Evident dissolutions were revealed on metallographic profiles for several forged aluminum parts *(Figure 1.5)*. These surface anomalies, identified during compression trials, could produce fluctuations on the general properties of the industrial parts especially made by this cast material.
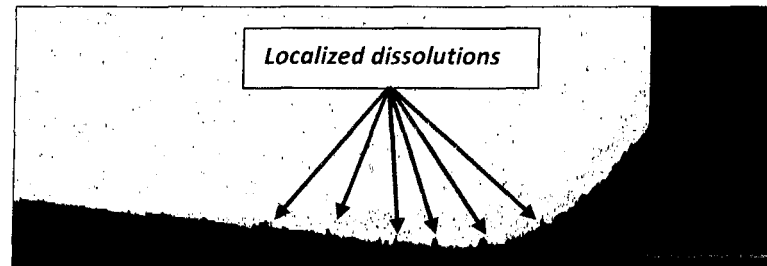
Figure 1.5: Preferential attack of aluminum cast-forged parts during cleaning steps (100X Magnification, courtesy of Rio Tinto Alcan)

1.2. Objectives of thesis

The main objective of this thesis is to study the « *Corrosion behavior of the forged-T6 AA6082 aluminum alloy from different feedstock* ».

The detailed objectives of this project are to:

1. Investigate and highlight microstructural and chemical differences between cast and extruded feedstock;

2. Quantify the corrosion susceptibility of cast-forged and extruded-forged aluminum parts with standard corrosion tests along with the impact of a T6 aging treatment;

3. Develop and use a system to evaluate the corrosion-fatigue susceptibility of aluminum forgings from different feedstock and the effect of adding a T6 heat treatment.

2

LITERATURE REVIEW

Firstly, a quick review of the manufacturing steps can well recognize the complexity surrounding these materials eventually produced. Four important stages are involved: 1) the vertical semi-continuous casting (VDC), 2) the extrusion process, 3) the forging process and 4) the heat treatments. These stages can explain all variables and process subtleties. The two last sections act as an introduction to understand the mechanisms and corrosion testing in order to advance the first investigation done by Rio Tinto Alcan on directly cast-forged products.

2.1. Production of forging billets (feedstock)

The following paragraphs explain the parameters instead of the stakes of each stage necessary to manufacture aluminum forged parts and help understand all variables associated with these processes.

2.1.1. Step 1: Semi continuous - DC casting processes

The raw material is melted in a furnace to prepare the specific aluminum alloy to cast. The molten metal processing is continuously performed in-line, and includes the elimination of H_2 gas, harmful trace elements and the separation of non-metallic inclusions in the molten aluminum. All these treatment steps are necessary to achieve a good ingot quality. *Figure 2.1* shows an overview of all molten processes to produce a good metal quality before the DC casting process.
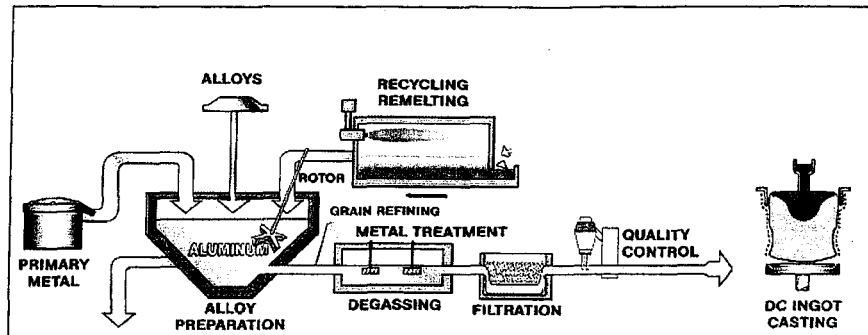
Figure 2.1: Schematic diagram of molten metal processes to DC cast aluminum billets (Courtesy of Rio Tinto Alcan)

From the furnace that preparing alloys, the molten metal is transferred via refractory culverts to degassing, filtration and quality control steps before accessing to final DC moulds. Two casting systems exist to regulate the liquid metal flow that enters the metallic molds: float and dip tubes where the level is controlled by a floater and, a level pour where the flow is controlled by keeping a certain level in the tundish. Continuous casting layouts feed several molds from the same tundish. When the molten metal is in contact with the casting mould, a primary cooling happens and produces a solid layer at the surface called the « shell zone » *(Figure 2.2)*. After this first step, water jets inside the molds produce a secondary cooling to completely solidify the aluminum ingot.
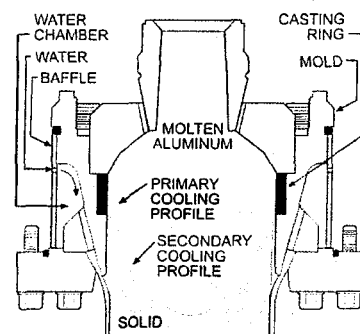
Figure 2.2: Aluminum DC casting mold diagram during the metal solidification [1]

Solidification discontinuities produced by normal vertical casting technologies can affect extruded and forged processed parts. They are sub-divided into four main categories: 1) gas porosity (entrainment of air and hydrogen H_2), 2) shrinkage (macroporosity and microporosity), 3) hot tearing and cracks and 4) inclusions and segregations. The last discontinuities category which includes macro and microsegregations may have important detrimental effects on surface, mechanical and corrosion properties. In continuous and semi-continuous direct chill (DC) casting, solidification occurs predominantly when heat escapes the solidifying ingot after the ingot exits the mold bore, and comes into direct contact with a stream of water. To a lesser extent, heat is also removed through the mold wall. The heat removal causes a thin skin or shell to form around the molten sump. Therefore, the shell thickness and strength are affected by how much heat is removed during the primary cooling and the alloy that is being solidified. During the shell formation, a variation in the concentration of alloying elements occurs. The area where this difference in concentration happens is often referred to the «Shell zone». It is composed of an enriched layer as the inverse segregated region, and is followed by a depleted layer (*Figure 2.3*).
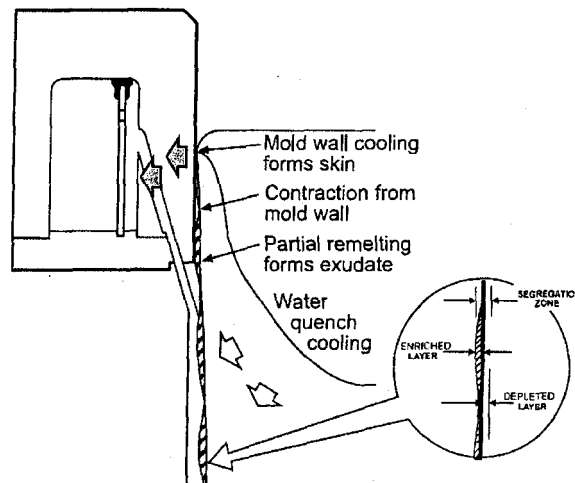
Figure 2.3: Segregation on a cast billet produced by the exudation phenomenon [3]

In microsegregation, solute rejection occurs during cell formation creating a solute-rich, low-melting point solution that is outside the grain boundaries and between the cells. In the next step, this low-melting point solution is transported to the surface due to freezing and partial remelting follows. Initially, heat lost through the mold wall solidifies the surface of the ingot. The surface then begins to shrink and pulls away from the mold wall. As this happens, heat from the molten sump remelts the low-melting temperature material. This liquid is then forced to exudate due to the metal static head and capillary pressures.

The result of these phenomena is a layer, largely depleted of solutes, being created just behind the enriched layer. Optimizing the water quench with a mold bore length and mold wall heat transfer can greatly reduce this segregation zone. As-cast microstructural studies of cross sectional slices of vertical direct chill cast billets of AA6082 and other aluminum alloys were investigated to identify and characterize these segregated layers [4,5,6,7]. *Figure 2.4* shows a typical segregation layer at the surface of AA6082 as-cast billets.

Enriched layer or Inverse segregated layer

Billet surface

Depleted zone after the inverse segregated zone

Figure 2.4: A typical view of microstructural features of the SSZ (Surface Segregation Zone) in an AA6082 aluminum alloy [4].

An EPMA approach (chemical analysis by an Electron Probe Microanalysis technique) was used to identify intermetallic phases in the segregated surface zone. The bright particles were identified to be $Al_{15}(FeMn)_3Si_2$ and the dark particles Mg_2Si *(Figure 2.5a)*. Linear composition analysis with EPMA technology allows the quantification of major elements in the first 120 µm of the as-cast billet surface *(Figure 2.5b)*.

| a) EPMA composition results showing intermetallic particles in the SSZ. | Distribution of the various alloying elements present in the AA6082 across 120 μm. |
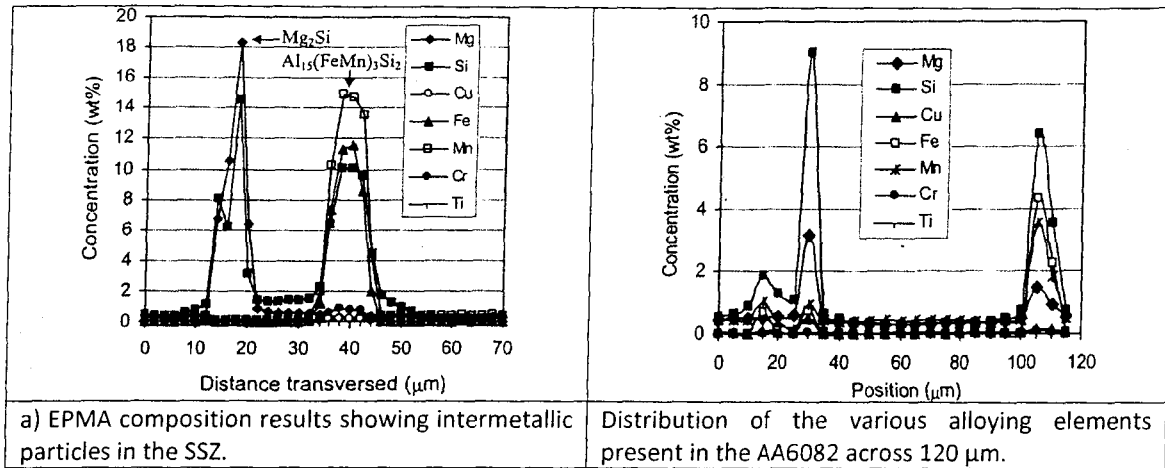
Figure 2.5: EPMA analysis to identify intermetallic phase particles in the SSZ [8]

2.1.2. Step 2: Extrusion or Rotating scalping process

The term extrusion is normally designated when a hot cylindrical aluminum ingot is pushed through a shaped die to make a product with a specific profile definition *(Figure 2.6)*. The resulting profile can be used in different applications such as mechanical structures, automotive components, aesthetic parts, forging materials, etc. The extrusion process is often used before forging in order to reduce the billet diameter to generate feedstock with a diameter of less than 152 mm with a smooth surface.
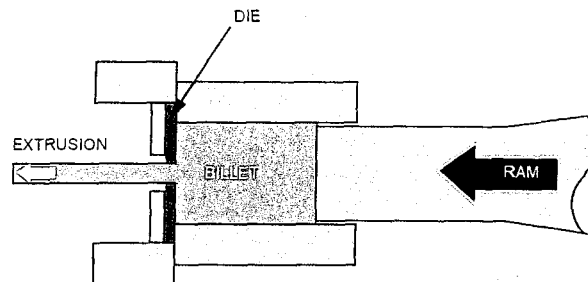
Figure 2.6: Diagram of an aluminum billet deformed by a steel die during the extrusion process [9]

Fundamental features for the extrusion process are described in the following steps.

1) A preheated aluminum log from DC cast products is put into a heated container where the temperature varies according to the alloy and other operational conditions. Normally, common AlMgSi alloys use a temperature range around 450 to 500°C.

2) At these temperatures, plastic flow stress properties of aluminum alloys are very low and give the possibilities to deform the billet easily through an applied high pressure. This force is created by a ram located at the end of the billet and pushed on a high strength steel die located at the other end of the container.

3) The pressure applied on the aluminum billet will force the metal to enter and take the shape associated with the steel die. As the metallurgical history states, many parameters can influence the final extruded product the preheating temperature, the ram speed, the extrusion temperature and the cooling system. Normally, a good parameter adjustment allows the extruder to obtain two types of microstructures with this process. The first option is a fully recrystallized grain structure and the second possibility is a partially recrystallized grain at the surface with a fibrous structure in the center *(Figures 2.7a and 2.7b)*.

a) Longitudinal extruded rod section with a fully recrystallized structure	b) Longitudinal extruded rod section with a partially recrystallized structure at the surface with a fibrous structure in the center
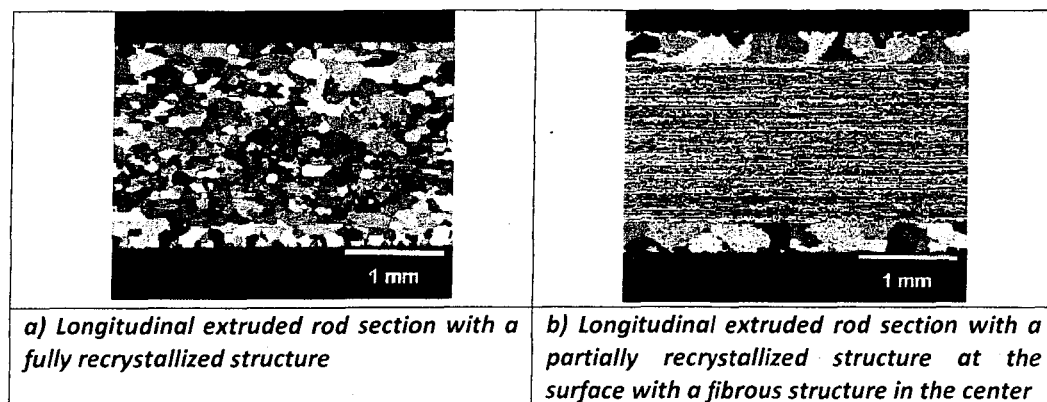
Figure 2.7: Typical macrostructures of hot extrusion with specific parameters [10]

Finally, other processes exist to prepare DC cast billets for the forging industry. For instance, rotating scalping technologies can replace the use of the extrusion process by removing metal with a high dimensioned lathe used until the desired diameter is reached. This technology is expensive and not productive for it creates important losses of metal and time.

2.1.3. Step 3: Forging process

Due to the good formability of aluminum alloys and the use of efficient presses, it is possible to produce high-precision forged parts with excellent properties which almost conform to end-use requirements. In general, these parts provide the following advantages: 1) high strength and low weight, 2) good corrosion resistance (for most aluminum alloys) and 3) the fibre (grains) structure can be arranged to correspond to the main loading direction leading to high strength and fatigue properties. Only a minimum of additional operations like deburring, final heat treatments and parts finishing are still needed. More precisely, many heat-treatable and non heat-treatable aluminum alloys are especially suitable for this forming operation. The AlMgSi alloys (6XXX series) are really appropriate for forging applications with excellent formability aptitudes, good corrosion properties, good mechanical properties and heat treatable possibilities. *Figure 2.8* explains the major categories of aluminum alloys associated with the forging process.
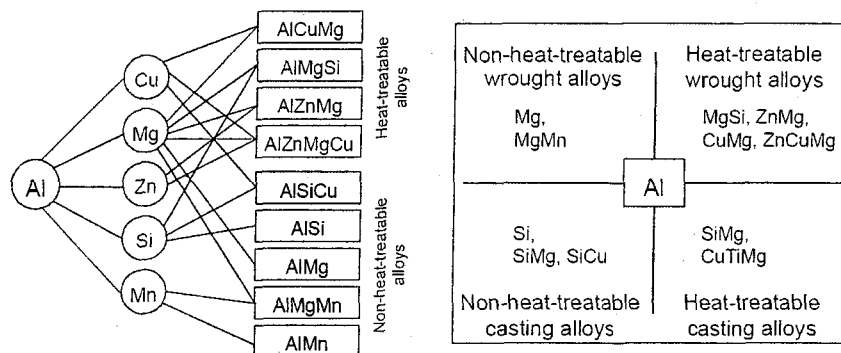
Figure 2.8: Aluminum alloys for forging applications [11]

Forging is a manufacturing process where the metal is pressed, pounded or squeezed under a great pressure into high strength parts known as « dies ». The process is normally performed hot by preheating the metal to a desired temperature prior to the final transformation. After this preparation, the metal is pressed into the bottom die where the top die is closed on itself to produce a final shape. In general, this process can create parts that are stronger than those manufactured by any other metalworking process. This process is used to produce a defined work piece geometry having good dimensions and volume accuracy.

2.1.4. Step 4: Heat treatment processes

After cooling down from a temperature of nearly 400°C, the forging is in a soft annealed state. For the non-heat-treatable alloys, this corresponds to the final condition required for the application. Heat-treatable alloys, on the other hand, can be heat treated, i.e. solution treated, quenched and aged, in order to deliver the most suitable service properties.

Solutionizing and aging heat treatments after the final forging process may have important impacts on mechanical and microstructural properties by producing a maximum of round β-Mg_2Si precipitated hardening particles. Grazyna Mrowka-Nowotnik and Jan Sieniawski from the Rzeszow University of Technology in Poland studied the influence of the cooling conditions after homogenization and aging of the AA6082 aluminum alloys [15]. The alloys were heat treated [-T4] with a wide range of solution heat treatment temperatures from 510 to 580°C. During the homogenization treatment at 570°C and air cooled, microstructural transformations of the β-AlFeSi phase and in the more spheroidal α-Al(FeMn)Si phase occurred in the AA6082 alloys (Figures 2.9a and 2.9b).

a) AlFeSi and α-AlFeMnSi intermetallic phases distributed at cell boundaries, connected sometimes with coarse Mg$_2$Si	b) Microstructural transformations of the θ-AlFeSi phase and in the more spheroidal α-Al(FeMn)Si phase after the thermal treatement
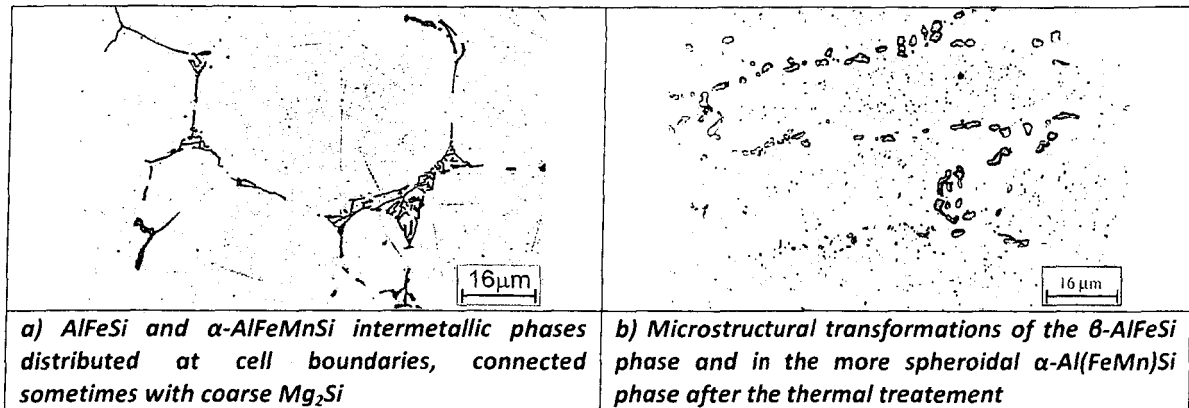
Figure 2.9: Microstructures of AA6082 alloy before and after the homogenization treatment at 570°C/6 h and air cooled [15]

During the hot extrusion of ingots, particles of the intermetallic phase position themselves parallel to the direction of the plastic deformation and therefore allow formation of the band structure *(Figure 2.11)*. After the deformation process, a -T61 heat treatment temper is commonly used to produce a supersaturated solid solution of elements. This optional step involves the formation of finely dispersed precipitates and small grain structures with high mechanical properties *(Figure 2.10)*.

a) Microstructure of AA6082 after hot extrusion at 500°C [15]	b) Microstructure of AA6082 extruded, cold rolled and T6 heat treated plate [10]
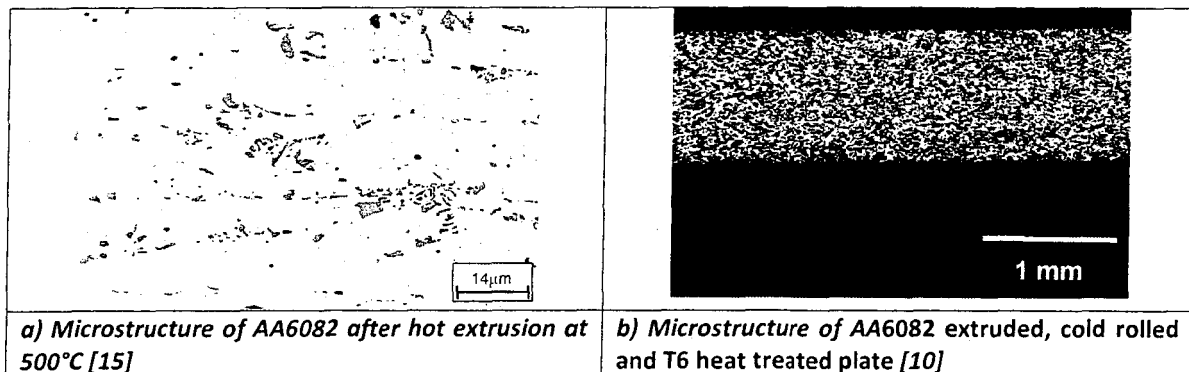
Figure 2.10: Hot extrusion and T6 heat treatment microstructures for the AA6082 alloy

2.2. Corrosion behaviour of aluminum and its alloys

The following paragraphs explain the electrochemical behaviour and passivity of aluminum and its alloys as well as the corrosion mechanisms and types usually found on industrial parts and experimental tests to evaluate their corrosion susceptibility. These theoretical explanations are the base to a good understanding of the prescribed experimental and subsequent corrosion results [16, 19].

Electrochemical reactions of corrosion for aluminum alloys in aqueous substances have been considered since many years. In the corrosion of aluminum substrates in an aggressive solution, the oxidation reaction is called «anodic reaction»:

$$\textit{Aluminum anodic reaction: } Al_{(s)} \rightarrow Al^{3+}_{(aq)} + 3e^- \qquad \textit{Equation (1)}$$
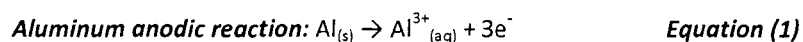
Solid aluminum loses three electrons to become a dissolved aqueous ion (Al^{3+}) during the corrosion phenomenon. This occurrence is in equilibrium with a simultaneous reaction to collect electrons released by the first anodic reaction called «cathodic reaction». Three thermodynamically reactions are possible in specific corrosive media.

Firstly, very acidic solutions with a high content of hydrogen ions (H^+) can reduce the ions into molecular hydrogen to produce gas (ex: nitric, chlorhydric, sulphuric solutions).

$$\textit{Hydrogen reduction reaction: } 3H^+_{(aq)} + 3e^- \rightarrow 3/2\ H_{2(g)} \qquad \textit{Equation (2)}$$
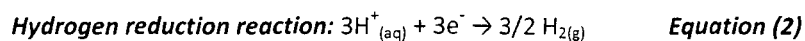
Secondly, neutral or alkaline solutions (ex: salted water, atmospheric humidity), produce hydroxide ions resulting from the oxygen made by the dissociation of water as shown in equation (3).

Oxygen reduction reaction: $O_{2(g)} + 2H_2O_{(l)} + 4e^- \rightarrow 4OH^-_{(aq)}$ *Equation (3)*
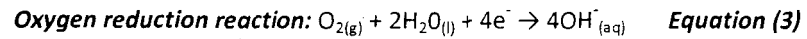
Finally, a third reaction is possible but only in weak acid media, where hydrogen and oxygen ions combine together to form water.

Water formation reaction: $O_2 + 4H^+ + 4e^- \rightarrow 2H_2O$ *Equation (4)*
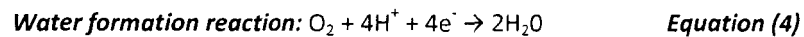
Globally, the aluminum corrosion phenomenon in aqueous media is the sum of two electrochemical reactions of oxidation and reduction. The next reaction presents the general equation for this important degradation phenomenon.

Global aluminum corrosion reaction: $Al_{(s)} + 3H_2O_{(l)} \rightarrow Al(OH)_{3(s)} + 3/2\ H_{2(g)}$ *Equation (5)*
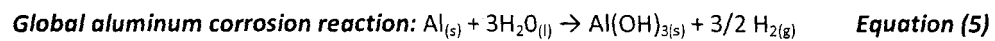
This final reaction modifies the thermodynamic state of aluminum metal in white oxidized products called «alumina» *(Figure 2.11)*. Aluminum corrosion is the formation of white and black layers that are insoluble in water and precipitate in a flake form on corrosion sites. At same time, the cathodic reaction releases hydrogen gas, water or hydroxide ions, depending of the pH solution.

White corrosion deposits of alumina
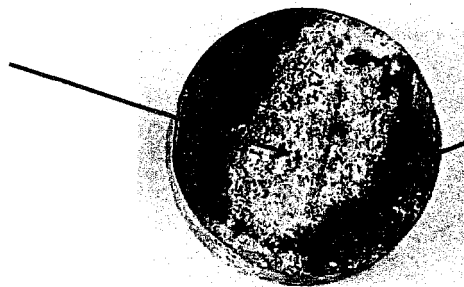
Black smut corrosion deposits of aluminum-magnesium oxides

Figure 2.11: Corrosion products identified as «aluminum oxides» (Al_2O_3) and «smut» on aluminum surfaces (Courtesy of Chicoutimi College)

2.2.1. Electrochemical theory and corrosion potentials

A metal with a high electro-negativity tends to be oxidized or corroded quickly in aggressive solutions. This tendency is stronger if the electro-negative potential is more negative. For instance, the magnesium element is a susceptible oxidation metal where a high humidity environment is dangerous and causes corrosion due to its high electro-negative potential (-2,380 V) [16].

The standard potential of aluminum is also relatively high with -1,660 V. It is especially caused by a high negative Gibbs free energy with -440 Kcal/mol. Aluminum is unstable with a humidity trace or water, it produces a natural oxide film that modifies its corrosion behaviour. In fact, this natural oxide layer on the surface of the aluminum parts normally protects it against an aggressive environment. The prediction of the corrosion phenomenon by the thermodynamic science, especially for passive metals such as aluminum, is different from the reality where oxide layers protect it against an aggressive environment. Thermodynamical data of standard potentials can indicate which reactions are possible in a corrosive media. The kinetic aspect is not covered by this electrochemical data because the reaction speed from really slow (ex: 10 years) to really quick (ex: 10 sec) can be erroneous for specific reasons. Special layers or metal passivities are good examples where the kinetic aspect of reaction can change the metal corrosion behaviour. Moreover, this theoretical potential needs to be measured in a specific 1 mol/l sulphuric acid solution with a platinum electrode. Consequently, it is difficult to adapt the standard potential to real industrial cases. The relative position of metals in the standard potential scale allows us to predict which will be the more anodic *(Table 2.1)*. In this case, the metal with the higher electro-negativity (more negative) will be dissolved by the corrosive solution. Also, galvanic corrosion can occur when an aluminum alloy is placed in an electrical contact with other metals having more important corrosion potential intervals than aluminum.

Table 2.1: Electrochemical standard potentials list of different pure metals [16]

Electrochemical Reaction	Standard Potential (V)
$Au \leftrightarrow Au^{3+} + 3e^-$	1,42
$Cu \leftrightarrow Cu^{2+} + 2e^-$	0,34
$H_2 \leftrightarrow 2H^+ + 2e^-$	0
$Fe \leftrightarrow Fe^{2+} + 2e^-$	-0,44
$Zn \leftrightarrow Zn^{2+} + 2e^-$	-0,76
$Ti \leftrightarrow Ti^{2+} + 2e^-$	-1,63
$Al \leftrightarrow Al^{3+} + 3e^-$	**-1,66**
$Mg \leftrightarrow Mg^{2+} + 2e^-$	-2,38

The dissolution potential normally referred to as *«Corrosion potential - E_{corr}»* is the barrier necessary to produce the corrosion phenomenon in a specific medium by taking into account the metal passivity. This potential can be measured alone by the ASTM G69 Standard or by further detailed potentiostatic tests. Normally, sodium chloride (NaCl) and hydrogen peroxide (H_2O_2) are added together to obtain stable and reproducible potentials. During this experimental test, two simultaneous reactions (oxidation of metal and reduction of ions such as H^+) are produced to evaluate the electrical potential. Every parameter that modifies the aluminum surface properties can change this dissolution potential. The electrochemical test can also be performed in other corrosive solutions (water, saline solution, acid solution, etc.) and become more flexible than the standard potential test. The following array *(Table 2.2)* presents dissolution potentials of different materials in a 3.5% NaCl solution.

Table 2.2: Dissolution potential for different metal or alloys in salted water [16]

Pure or alloyed metal	Potential (V)
Stainless Steels	-0.10
Titanium	-0.15
Carbon steels	-0.61
Aluminum 1050 alloy	**-0.75**
Magnesium	-1.60

For example, the alloying content in aluminum alloys can modify the dissolution potential of the metal. This electrochemical effect can be in a positive or a negative mode on the potential scale. In major part, this dissolution potential is determined by the principal solid solution at the metal surface as shown in the examples in **Table 2.3**.

Table 2.3: Dissolution potential of different phases or pure metals in salted water [16]

Pure metal or intermetallic phase	Dissolution potential (mV)	Pure metal or intermetallic phase	Dissolution potential (mV)
Silicon	-170	Al_2CuMg	-910
Al_2Cu	-440 and -640	$MgZn_2$	-960
Al_3Fe	-470	Mg_2Si	-1190

2.2.2. Passivity phenomenon

Aluminum is a natural passive metal that creates a protective oxide layer on its surface. It is not necessary to manually passivate it unlike for steel. In the majority of media, the dissolution potential of aluminum is approximately around -0.5V with a hydrogen electrode. Aluminum metal is normally stable in an oxidizing media, similar to water, air or an alkaline solution. This protecting behaviour occurs by a natural oxide layer formation that is continuous, uniform and identified as alumina «Al_2O_3». This colourless oxide film consists of two important layers, namely, Boehmite and laydown barrier with an approximately 100 nm total thickness.
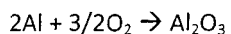
$$2Al + 3/2O_2 \rightarrow Al_2O_3 \qquad \textit{Equation (6)}$$

1) The first layer is called «**Boehmite (AlO(OH)) or Bayerite hydrate (Al(OH)$_3$)**» and its constitution is made from porous and hydrated alumina. The final oxide film thickness reached depends on physicochemical conditions (humidity, temperature, pressure, etc.)

2) The second layer named « **Lay down barrier** » is an amorphous and compact aluminum oxide. This special film has good dielectrical properties. It acts as a protective barrier against corrosion by blocking electrical ion exchanges. This layer is formed as soon as the metal or the liquid comes into contact with the air or the oxidizing medium.

Alumina can exist in different allotropic forms. Oxide formation conditions have important effects on the final layers composition and thickness. Increasing temperature, pressure, velocities or moisture parameters during a corrosion phenomenon can accelerate and increase layers formation. The density difference between aluminum and aluminum oxide produces a layer with compressive strengths. This reason explains why the oxide layer has good properties during metalworking processes (ex: rolling, forging , stamping...).

For example, the concentration of alloying elements can positively or negatively influence the corrosion susceptibility by modifying the oxide film properties. Some elements can reinforce the corrosion resistance to produce an oxide mixture at the surface since together they have a coherent structure. Magnesium addition has a positive effect on the corrosion properties of 5XXX and 6XXX aluminum series. On the other hand, copper has a bad influence causing many corrosion problems with 2XXX and 7XXX aluminum series *[16,19,27,40]*. In a major part, alumina dissolution in the protective layer depends on the pH magnitude in the corrosive solution. There is a predominant and accelerated dissolution in strong acid or high alkaline solutions. Normally, this oxide film is not stable under pH parameter equal to 4 and above 9. This chemical phenomenon is restrained for specific materials called «amphoteric»[1]. However, the pH parameter is not the only concern for the natural oxide film stability in corrosive solutions. Conductivity, dissolved oxygen percentage and aggressive ions species can modify the corrosion susceptibility.

---

[1] In chemistry, an **amphoteric** substance is one that can react as either an acid or base. The word is derived from the Greek prefix ampho- (αμφί-) meaning "both". Many metals (such as zinc, tin, lead, aluminum, and beryllium) and most metalloids have amphoteric oxides or hydroxides. (International Union of Pure and Applied Chemistry. "amphoteric". *Compendium of Chemical Terminology* Internet edition).

Acid or alkaline base characteristics may have effects during the corrosion mechanisms of aluminum. The corrosion rate in a 0.1g/L sodium hydroxide solution is 25 times higher than in an ammonia solution at 500g/L (NH_3) with a similar 12.5 pH. The same phenomenon happens in acid environments. Chlorhydric acid (HCl) or nitric acid (HNO_3) are more destructive than acetic acid ($C_2H_4O_2$) at the same pH level. The following figure presents corrosion rate fluctuations for a specific aluminum alloy in different acid and base solutions *(Figure 2.12)*.
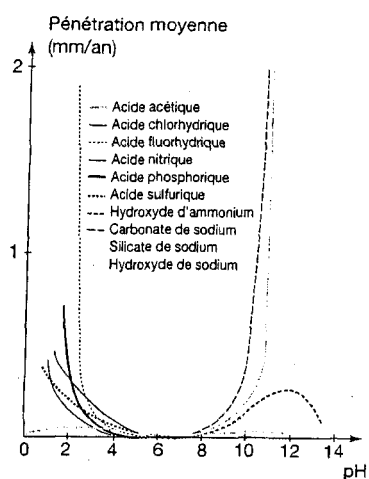
Figure 2.12: pH influence on corrosion rates for the 1100-H14 aluminum alloy [16]

2.2.3. Corrosion forms

Aluminum alloys exhibit several corrosion mechanisms during this unintended process. They are identified as localized pitting corrosion, intergranular corrosion, stress corrosion cracking, and corrosion-fatigue. The first mechanism mentioned is the worst and insidious type as it produces holes that adulterate the surface and the mechanical properties.

1) Localized pitting: This localized corrosion form will produce important cavities at the metal surface and the corrosion phenomenon depends directly on which media and service conditions are used *[29, 30]*. Aluminum alloys are very affected by the pitting corrosion mechanism especially in acid environments with chloride species. This chemical product is always a special attraction as it leaves a white layer deposition on the grey metal surface. As all passive metals, the oxide layer breaks (initiation) and the corrosive solution can continue dissolving aluminum atoms (propagation). Density of the pits depends on the aluminum alloys and can be evaluated between 10^4 pits/cm^2 and 10^{10} pits/cm^2. Among a high number of pits present on the surface, only some of them will grow and continue to propagate through the metal conducted by two electrochemical reactions:

Oxidation:	$2Al \rightarrow 2Al^{3+} + 3e^-$		*Equation (7)*
Reduction:	Neutral or base media	$\frac{3}{2} O_2 + 3H_2O + 6e^- \rightarrow 6OH^-$	*Equation (8)*
	Acid media	$6H^+ + 6e^- \rightarrow 3H_2$	*Equation (9)*
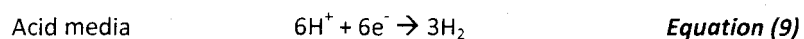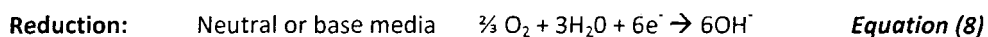
If the anodic reaction is stable and localized, pitting corrosion will produce deep holes (pits) in the aluminum metal *(Figure 2.13)*. After this first step, the hydroxide ion formation (anodic reaction) or H^+ consumption (cathodic reaction) will cause a local excess of OH^- ions and therefore a pH increase (alkalinization).

The global reaction for the aluminum pitting mechanism is stated in the following equation:

Global pitting reaction:	$2Al + 3H_2O + 3/2O_2 \rightarrow 2Al(OH)_3$	*Equation (10)*

a) Schematic diagram of pitting corrosion for aluminum alloys by the localized acidification way [16]	b) Cross section of a pitting attack on AA6082 aluminum alloy after exposure to a marine atmosphere for six months. The dark spots are intermetallic particles [17]
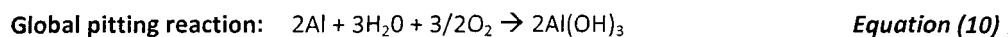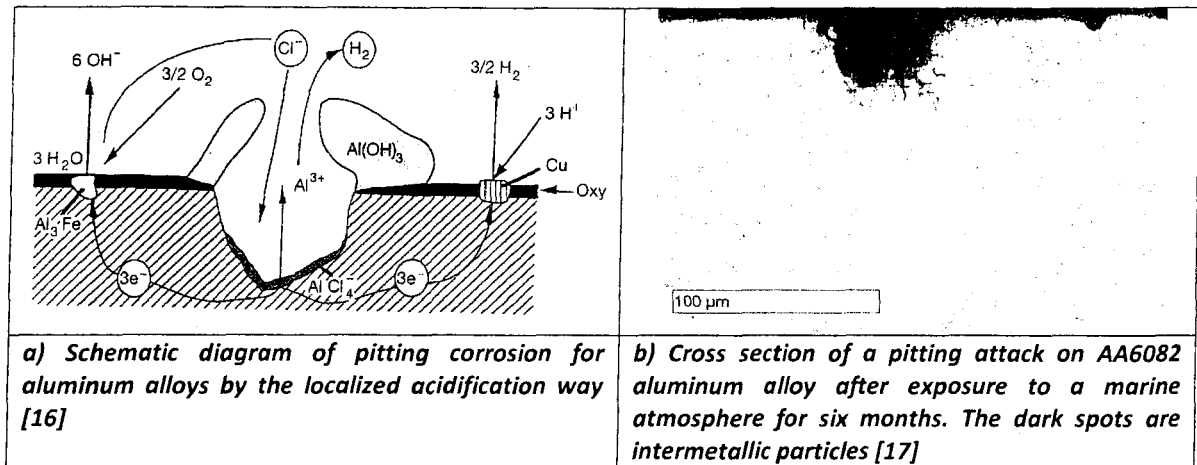
Figure 2.13: Pitting examples on aluminum alloys in a chloride media

2) Intergranular corrosion (IGC) is the selective dissolution of the grain boundary zone, while the bulk grain is not attacked. IGC is also caused by microgalvanic cell action at the grain boundaries. The susceptibility to IGC is known to depend on the alloy composition and thermomechanical processing. Grain boundaries are sites for precipitation and segregation, which makes them physically and chemically different from the matrix. Precipitation of noble particles at the grain boundaries depletes the adjacent zone of these elements, and the depleted zone becomes electrochemically active. The opposite outcome is also possible; precipitation of active particles at the grain boundaries would make the adjacent zone noble. **Figure 2.14** shows the first case where noble particles induce corrosion at the grain boundaries for AlMgCu alloys. These noble intermetallic particles (Al_3Fe, Al_2Cu), coupled with the solid solution (aluminum matrix), will produce a severe microgalvanic coupling *[16, 19, 26, 40]*.
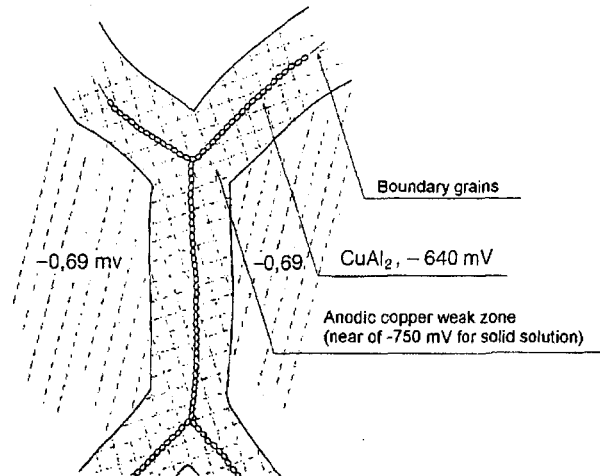
Figure 2.14: Intergranular corrosion (IGC) with Cu particles in 2XXX series [16]

Normally, three conditions are required to develop intergranular corrosion susceptibility in aluminum parts:

- A corrosive media;

- A potential difference of 100 mV between intermetallic particles and the solid solution;

- A continuous precipitation of intermetallics for the propagation of intergranular corrosion.

In general, IGC susceptibility in aluminum alloys strongly depends on microstructural properties and heat treatment tempers. Solutionizing heat treatments (T3 or T4 types) are less sensible than aging processes (T6) due to the possibility of precipitation of intermetallics near the grain boundaries. In this case, many actions can be taken to avoid precipitation of intermetallic particles by redistributing them uniformly into the aluminum matrix with a double aging treatment (T73 type) or increasing the quench rate - aging time to form efficient precipitates *[16]*.

3) The stress corrosion cracking (SCC) mechanism is defined from a synergy between a sufficient stress applied on aluminum parts in a corrosive environment inducing unexpected but normally ductile sudden failure. For a given alloy, SCC is often one which is otherwise only mildly corrosive to the metal. Hence, metal parts with severe SCC can appear bright and shiny, while being filled with microscopic cracks *(Figure 2.15)*. Only a very small concentration of certain highly active chemicals in the environment is needed to produce catastrophic cracking. Well-known specific environments for aluminum alloys include water vapor, aqueous solutions, organic liquids and liquid metals *[16, 19, 40]*.
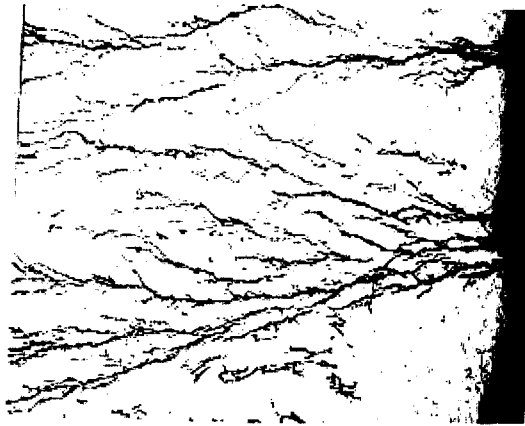
Figure 2.15: Stress corrosion cracking morphology on 2XXX aluminum profiles [18]

The stress can be the result of crevice loads due to stress concentration, or can be caused by a type of assembly or residual stresses from fabrication (e.g. cold working). The residual stress can be relieved by an annealing heat treatment. However, in laboratory tests at high stresses and in aggressive solutions, cracking has been demonstrated in 6xxx alloys with a particularly high alloy content and containing silicon in excess of the Mg_2Si ratio and/or a high percentage of copper *[19]*.

4) Corrosion-fatigue: The mechanical phenomenon alone is a major cause of fractured aluminum parts. By adding a corrosive medium, the cyclic stress produces an important synergistic effect with the first phenomenon that quickly increases the corrosion susceptibility. The CF mechanism is not limited by certain metallurgical factors or specific environments unlike other types such as SCC. In contrast, there is a relationship that links corrosion-fatigue, stress corrosion cracking and the hydrogen embrittlement phenomena. In the center of the cross-hatched circles *(Figure 2.16)*, all three corrosion mechanisms interact together by synergistic degradation. This is representative of many situations, especially for ductile alloys in an aqueous environment *[20, 40]*.
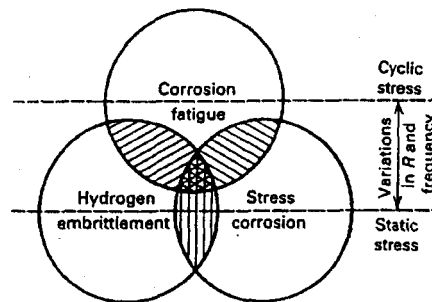
Figure 2.16: Interrelationship among corrosion-fatigue, hydrogen embrittlement and stress corrosion cracking with a minimum to maximum stress applied [20, 40]

The CF mechanism is defined as the phenomenon of cracking in material under the combined action of fatigue loads surrounded by a corrosive environment (aqueous or gaseous). This phenomenon is identified as happening in numerous engineering alloys over a wide range of environments and has been renown as an important cause of failure for materials. The description and comprehension of corrosion-fatigue kinetics and mechanisms are necessary to service the life prediction and progress of CF resistant alloys. The FCGR (Fatigue Crack Growth Rate) and the increment of crack size per load cycle, are important for risk assessment and for predicting the remaining life. This is often described by a relationship with the K stress intensity factor which includes stress magnitudes, sizes and shapes of the cracks *[21,26,35,41,43]*.

Both fatigue life and fatigue limit can be clearly decreased in the presence of a corrosive environment, and, in many cases, the endurance limit is no longer observed. In addition, corrosive environments can accelerate the «FCGR». In an air medium, the relative moisture parameter has a small effect on the corrosion-fatigue resistance for aluminum alloys. At very low values of humidity (< 5% RH), the fatigue life increases modestly. Laboratory corrosion-fatigue essays indicate that the presence of water during the cycling process markedly lowered the fatigue life. The endurance strengths obtained in demineralized or brine solutions show little differences. For active-passive material, the loading frequency is one of the critical factors that influence the CF phenomenon. Cathodic protection will attenuate the corrosion-fatigue type but amplify the HE (SCC) problem.

Aluminum alloys and several steels alloys have a relatively low corrosion-fatigue resistance compared to fatigue properties in an air environment. The fatigue endurance of aluminum alloys is decreased by specific corrosive media like seawater or saline solutions. This fact is especially true when low stresses, long duration time or low frequencies are applied during the fatigue tests.

Corrosion-fatigue resistance is normally better for the 5xxx and 6xxx aluminum alloys series compared to the 2xxx and 7xxx more susceptible alloys. Corrosion-fatigue strengths are not greatly affected by variations in heat treatments (2xxx, 6xxx and 7xxx series) *[19]*.

The stress-life method is typically used for long life situations (millions of cycles) where the stresses are elastic. This method is often referred to as infinite life design. It is based on the fatigue limit or endurance limit of the material. Material properties from polished specimens are modified for surface conditions and loading conditions being analyzed. In high-cycle fatigue situations, material performance is commonly characterized by a *S-N curve*, also known as a *Wöhler curve*. The curve is a graph of the magnitude of a cyclical stress (*S*) against the logarithmic scale of cycles to failure (*N*) *[26]*.

The S-N curves are derived from tests on samples of the material to be characterized (often called coupons) where a regular sinusoidal stress is applied by a testing machine which also counts the number of cycles to failure. This process is sometimes known as coupon testing. Each coupon test generates a point on the plot though, in some cases, there is a runout where the time to failure exceeds that available for the test. Analyses of fatigue data requires statistical techniques to determine specific polynomial regressions and confident intervals.

The typical stages of the fatigue damage process are described in **Figure 2.17** where the slip first occurs, followed by fine cracks that can be seen only at high magnification. These cracks continue to grow under cyclic loading and eventually become visible to the naked eye [21].
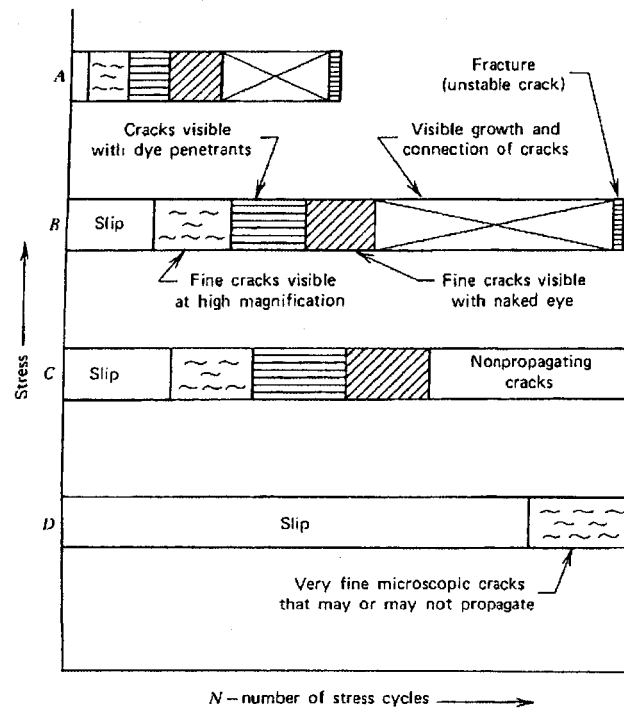
Figure 2.17: Schematic representation of the fatigue process for a S-N curve (Wöhler) [21]

In 1989, Elboudjdaini and Ghali studied the corrosion-fatigue behaviour of 6061 and 5053 aluminum alloys in a 3% NaCl environment *[20]*. *Figure 2.18* shows Wöhler curves of the Al-Mg-(Si) fatigue test results.
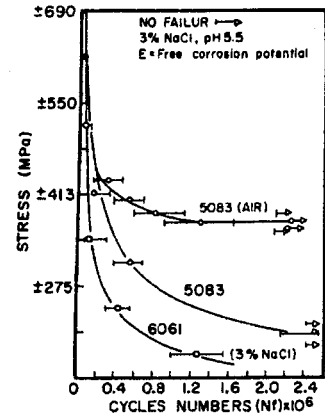
Figure 2.18: Wöhler curves of corrosion-fatigue (R=-1) for 5083-H321 and 6061-T6 in air and a 3% NaCl solution [20]

Another research paper *[1]* on fatigue strengths compares the as-cast ISOTROPAL alloy to the same extruded materials in a 5% sodium chloride media. The 6066 Al and the 6110 Al aluminum alloys in the 6xxx series were tested in corrosion-fatigue. Results show an important decrease in fatigue life assessment where stresses varied from 200 and 50 MPa *(Figure 2.19)*.
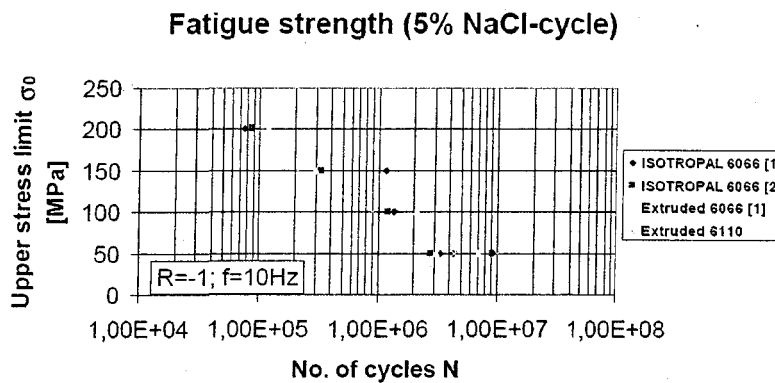
Figure 2.19: Fatigue Wöhler curves for 6066 and 6110 aluminum alloys in a 5% NaCl corrosive solution [1]

It was reported that the corrosion pitting mechanism has an important role in the evolution of fatigue damages *[22-24]*. Pitting corrosion was induced by the local dissolution of the matrix through its galvanic coupling with constituent particles in the AA2024 aluminum alloys. These pits serve as nuclei for subsequent

fatigue cracking and significantly reduce the serviceable life of a component. Corrosion-fatigue cracking

would nucleate at severe corrosion pits. The predicted fatigue lives at different stress levels from 100 to 400

MPa for an initial pit radius of 10 to 200 microns were identified *(Figures 2.20a and 2.20b)*.

a) Comparison between predicted (aij) and measured (aexp) pit sizes	b) Influence of stress amplitude and initial particle or pit size on fatigue life
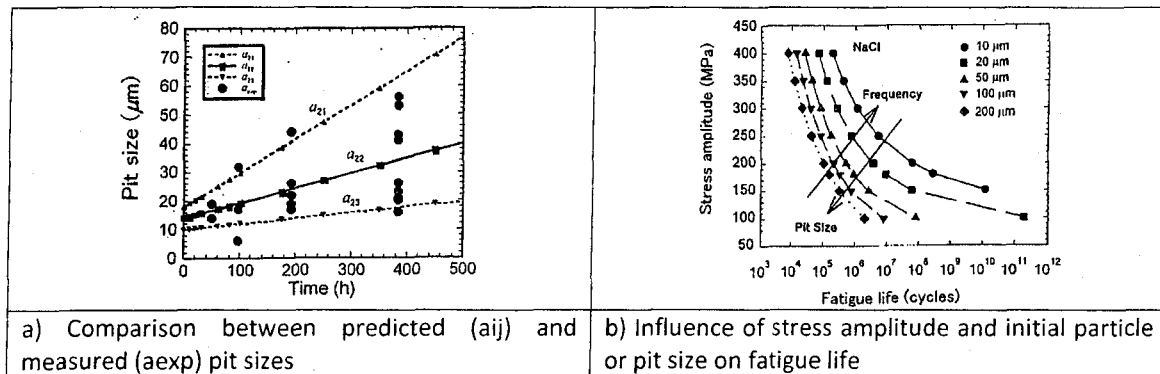
Figure 2.20: Relationship between pit sizes with corrosion-fatigue life for a 2024-T3 aluminum alloy exposed to 0.5 M NaCl [22]

Rotating bending fatigue tests were performed by Tokaji and Goshima in 2002 to determine the fatigue

behaviour of 6063 aluminum alloy in a 3% NaCl corrosion solution. The fatigue strength of 6063 alloy

decreased with increasing aggressiveness of the environment, but was nearly the same as those of AA2024

and AA7075 aluminum alloys *(Figure 2.21)*. Intergranular crack initiation was attributed to the corrosive

dissolution of grain boundary precipitates and a precipitation free zone.
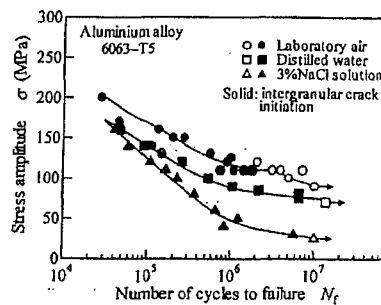
Figure 2.21: S-N diagram for AA6063 Al alloy in different corrosive environments [25]

Corrosion-fatigue depends on many relations between the material, the environment, the electrochemical conditions and the mechanical loading parameters. The cracking phenomenon for ductile alloys involves plastic deformation where this localized deformation is induced by fatigue loadings that cause a final failure below the yield stress. Many corrosion-fatigue mechanisms exist to explain the enhanced crack growth rates with low degrees of success. The fatigue crack growth rate parameter is a significant factor in characterizing this phenomenon. The generalized corrosion-fatigue cracking mechanism involves an anodic dissolution at the crack tip (i.e. electrochemical propagation theory) with a hydrogen embrittlement supplement *(Figure 2.22)*.

1 — Mass transport to crack tip
2 — Reactions in the solution
3 — Surface adsorption
4 — Surface diffusion
5 — Surface reactions
6 — Absorption
7 — Solid state diffusion
8 — Solid state reactions
9 — Actual fracture process
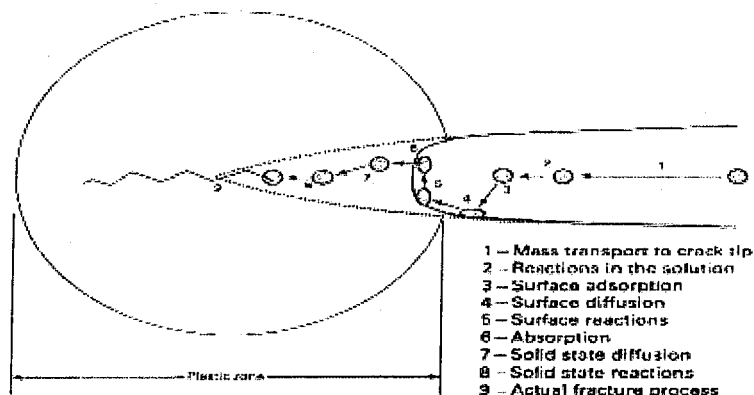
Figure 2.22: Crack tip to explain anodic dissolution of passive aluminum alloys [26]

In the anodic dissolution theory *[26]*, there are four possible mechanistic ways: slip-dissolution, brittle film-rupture, corrosion tunnelling and selective-dissolution (dealloying). During the corrosion-fatigue mechanism, the anodic dissolution depends on «how» and «when» the oxide protective film will rupture at the crack tip by this cyclic process. Moreover, the repassivation rate versus the newly exposed fresh metal enter in competition together. The FCGRs are controlled by specific parameters such as the anodic dissolution rate, the repassivation rate, the oxide film rupture rate, the mass transport rate of reactant and the flow rate of the solvated metal cations away from the surface.

The repassivation rate is critical for fatigue corrosion resistant materials *[26]* because it must be quick enough to avoid extensive dissolution, as this leads to crack tip blunting and pit formation rather than sharp and directional dissolution at the crack tip. Anodic dissolution by slip-dissolution is the most used hypothesis to explain the corrosion under fatigue loadings. A slip step forms at the crack tip and ruptures the protective surface film. Fresh surfaces react with the environment and partly dissolve until the crack-tip region is completely repassivated and the protective surface film is repaired. These processes repeat themselves when a persistent slip band (PSB) step reoccurs and ruptures the protective film and exposes more naked surfaces *(Figures 2.23a and 2.23b)*.

a) Schematic persistent slip intrusion-extrusion bands during the fatigue corrosion [27]	*b) SEM microscopy of PSB localized deformations of a tensile test with an aluminum wire of 25 μm diameter [28]*
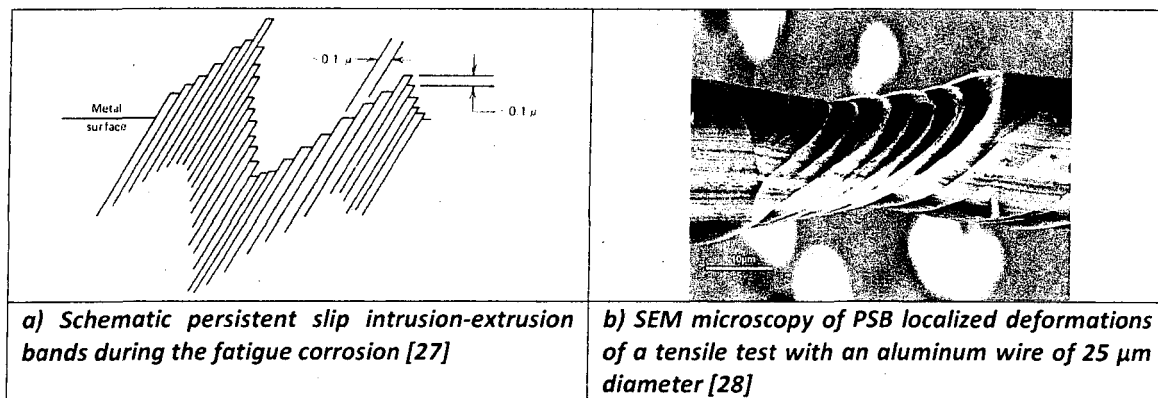
Figure 2.23: Slip bands due to cyclic external loads for Al alloys

This dissolution mechanism is often used to explain corrosion-fatigue cracking of alloys exposed in an aqueous environment. It is very difficult to explain the corrosion-fatigue in gaseous environments (water vapour, hydrogen or hydrogen sulphide) where the necessary electrochemical dissolution reaction is impossible at the crack tip.

Corrosion-fatigue appearance: The fatigue phenomenon creates intimate fretting contacts between mating crack faces by pumping the aqueous environments into the crack tips by the crack walls with a repeated blunting and resharpening of the crack tips. The reverse loads, frequencies and the cyclic waves formed can influence the dissolution rate and crack development for aluminum alloys.

Fatigue damages can be divided into the five following stages.

1. **Precrack cyclic deformation:** Repetitive mechanical damages are accumulated in some local regions; dislocations, twins, grain boundaries and constituent particles may develop, and persistent slip bands (PSB), extrusions and intrusions, as well as localized pits, may form.

2. **Crack initiation:** Cracks initiate as a result of the deepening of intrusion-extrusion bands.

3. **Crack propagation (Stage I):** Crack growth in this stage is within the planes of high stress.

4. **Crack propagation (Stage II):** Well-defined cracks propagate on the planes of high tensile stress in the normal direction to the maximum tensile test.

5. **Ductile fracture (Stage III):** When the crack reaches sufficient length so that the remaining cross-section cannot support the applied load, ductile fracture occurs.

Crack initiation stage by corrosion pits: Preferential attacks by an environment at specific surface locations may provide the most favorable sites for crack initiation when a part or structure is exposed to a corrosive medium during service. For example, intermetallic phase particles such as iron and copper in an aluminum substrate with a sodium chloride environment contribute sites for corrosion pits and subsequent fatigue crack initiations [29,30,31,32,33]. These ions produced in solution can catalyze the anodic dissolution of metal from the matrix. Local acidification due to the hydrolysis of metal ions enhances the dissolution of intermetallic phases or inclusions. Low pH conditions also help the hydrogen cathodic reaction and, consequently, increase the possibility of hydrogen embrittlement (HE) where the local ductility is decreased at the crack tip.

Crack propagation stage: *Figure 2.24a* shows a schematic fatigue crack propagating across several grains and primarily controlled by shear stresses (Stage I), and then growing in a zigzag essentially perpendicular to the crack tip by tensile stress (Stage II). *Figure 2.24b* presents a real case of the fatigue damage stages in Al-Li alloys.

| a) Schematic of Stages I (shear mode) and II (tensile mode) transcrystalline microscopic fatigue crack growth [21] | b) Surface crack profile of transcrystalline fatigue crack growth in Al-Li alloys [21] |
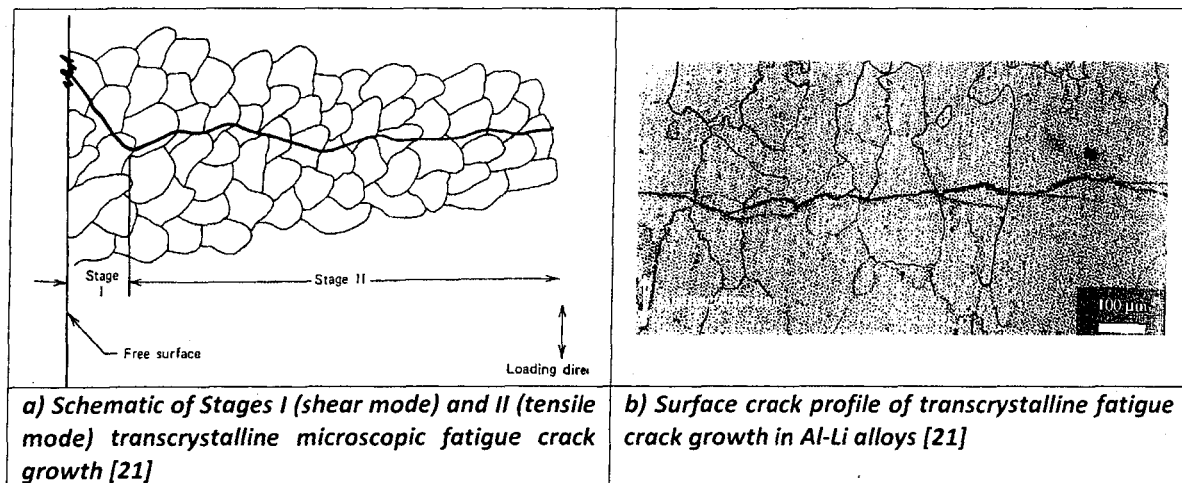
Figure 2.24: Damage stages during nucleation and growth of fatigue cracks in aluminum alloys

Final rupture stage: Failures for aluminum alloys are characteristically transgranular for fatigue corrosion and thus different from SCC failures, which are normally intergranular with several microcracks *(Figure 2.15)*.

In some cases, corrosion-fatigue cracks can exhibit a combination between these morphologies. A localized corrosion mechanism such as pitting or intergranular types provides a stress factor which adds and greatly affects the fatigue life. Although multiple cracks can be initiated during the fatigue phenomenon, fatigue failure often results from the propagation of a single and important crack. Crack interaction and coalescence propagation mechanisms are important to be understood in the corrosion-fatigue failure process *(Figure 2.25)*.

Figure 2.25: Macroscopic examination of the lateral surface CF specimen cycled at 45% of elastic limit in

3% NaCl. Cracks follow the alignment of the pits in Al 5053 (200X) [19]

LP Borrego *[34]* studied low-cycle fatigue for the AA6082-T6 aluminum alloy with cylindrical specimens under a symmetrical push-pull loading. Results of fatigue fracture surfaces reveal chaotic wavy appearances. *Figure 2.26* shows the occurrence of cleaved particles in voids and a widely dispersed microvoid formation around the second-phase particles.
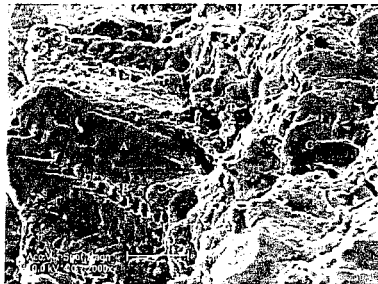
Figure 2.26: SEM image of fatigue fracture surfaces, De=2 ¼ 1%. Alloy 6082-T6 [34]

As stipulated in the same section pages 32 and 33, fatigue crack growth paths, often found in sheet or plate products, have several propagation stages (Stage II tensile mode and Stage III shear modes) before the final fracture *(Figure 2.27)*. Initially, the crack will propagate in tensile mode at the crack tip due to important endurance stresses applied at 90 degrees (Stage II). Beachmarks commonly associated with the fatigue phenomenon will appear. This is produced by a change in crack growth conditions such as an environmental change, a stress level or a pause in the stress cycling.

After this step, two possible rupture modes are encountered in fatigue brocken parts: single or double

shear propagation modes (Stage III). Microscopic cracks usually grow in the plane where maximum shear

stresses are found (slant 45° fracture).
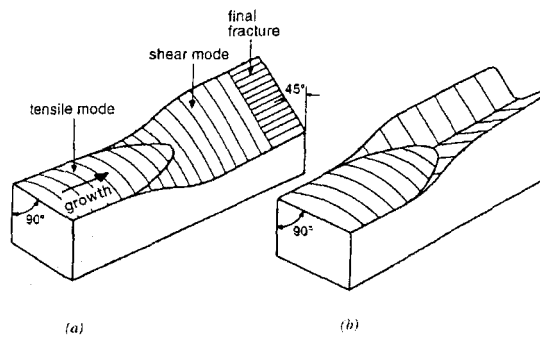
Figure 2.27: Transition of fatigue crack growth in sheet from tensile to shear modes (a) tensile with single

shear mode (b) tensile with double shear mode [21]

These stages provide a tool to help identify fatigue locations. However, at high loads and with high fatigue

crack growth rates in relatively thin components made of relatively tough material, a transition to

propagation on a slanted plane can occur *[35]*. *Figure 2.28* summarizes the macroscopic fatigue fracture

surfaces as a function of load magnitudes for reverse bending loads. The hashed regions identify the typical

fracture regions encountered, while the lighter regions with lines identify the fatigue crack regions.

(a) Low stress applied   (b) High stress applied
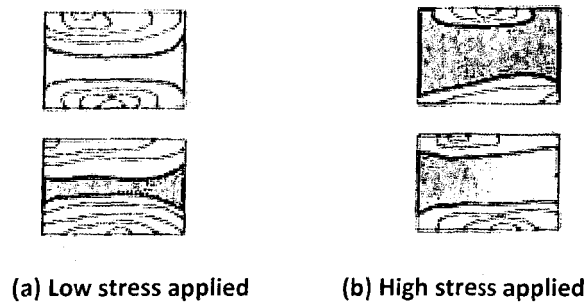
Figure 2.28: Fatigue fracture patterns during reverse flexural bending test with low (a) and high (b)

stresses applied [36]

Ratchet marks can be identified to describe features that are very useful in the identification of fatigue fractures and in locating and counting the number of fatigue origins (initiation sites). These are essentially perpendicular to the surface from which fractures originate. In flat parts, such as leaf springs, they are initially perpendicular to the surface but may curve if the bending is unidirectional. When several fatigue origins are adjacent to each other, each will start its own fatigue crack propagating as seen in *Figure 2.29*. If the origins are roughly the same, the fatigue crack growing from the one origin will start to overlap the fatigue crack from another origin. This feature creates a corner angle perpendicular to the surface of the part.

Side view of ratchet marks
caused by tension or bending

Side view of ratchet marks
where the major force was torsion
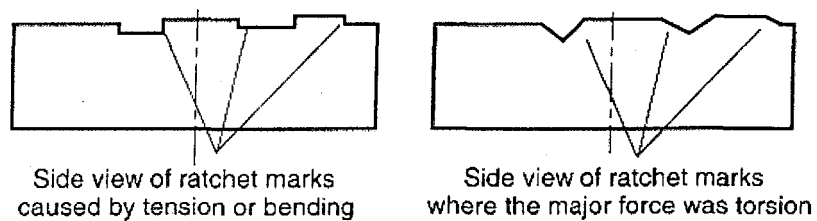
Figure 2.29: Two similar appearing sections of shaft fatigue failures with ratched marks present [37]

Material surface conditions can also influence the proportion for each stage during the corrosion-fatigue endurance. For example, surface discontinuities such as sharp notches, casting defects, non metallic inclusions and hydrogen porosities (blisters) can significantly reduce the fatigue lifetime *[37]*. Corrosive environments can influence all stages except the last one, in which ductile fracture occurs.

An electron microscopic analysis of the fracture surfaces can reveal a wide range of fatigue crack growth mechanisms. Here are three of the more common modes.

1. **The striation formation:** The most common aspect are ripples that are not the benchmarks described. They are smaller and contain thousands of microscopic deformations. Striations are formed by a plastic crack tip blunting during the loading and unloading sequences. For example, striations are usually well defined in aluminum alloys fatigued in air, but not under vaccum. Corrosion or mechanical damage can obliterate the striations *[38]*.

2. **The microvoid coalescence (MVC):** This takes place by the nucleation, growth and coalescence of microvoids during the plastic deformations.

3. **The microcleavage:** This undesirable cracking method is produce by «brittle» inclusions with lowered energy.

The next picture *(Figure 2.30)* presents an example for each microscopic propagation mode that is enumerated above in the list. An example of each fatigue propagation mode just enumerated can be seen in Figure 2.30.
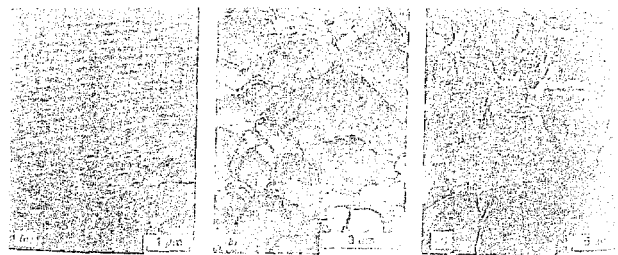
Figure 2.30: Fatigue propagation modes (a) Striations (b) Microvoid coalescence (c) Microcleavage [21]

Standard test methods for interpretations and similar results have not been fully developed for the corrosion-fatigue mechanism. In several cases, the CF and SCC phenomena are almost non dissociable and therefore produce non-conservative and non standardized data *[44]*.

2.3. Corrosion testing for aluminum alloys

Corrosion susceptibility of alloys is based on a number of factors such as service history, field in-plant corrosion tests, pilot plant and laboratory corrosion tests. Over time, laboratory tests have proven to be the most reliable and simple means to generate information for the selection of process materials. Many of these tests are routinely performed to provide information on:

- Fundamental corrosion evaluation;

- Failure analysis;

- Corrosion prevention and control;

- Acceptance of quality assurance;

- New alloy/non-metallic or product process development.

Electrochemical tests are predominantly used for aluminum alloy corrosion susceptibility to detect important potential differences between components. Electrochemical potential variations can create severe corrosion phenomena on assembled parts (ex: steel fasteners coupled with aluminum parts) or intrinsic to the material (ex: noble intermetallic phase particles in aluminum substrate). However, these electrochemical results can only be compared to the potential as a known relative reference system.

Experimental corrosion tests (immersion or atmospheric contact) are normally designed to determine mass losses during a specific duration time. For aluminum alloys, this mass loss is not sufficient enough and also not linear to evaluate the corrosion susceptibility due to the main active pitting mechanism.

2.3.1. Corrosion susceptibility evaluation by cabinet exposure tests

Cabinet testing refers to tests conducted in closed cabinets where the conditions of exposure are controlled and mostly designed to accelerate specific corrosion situations while trying to emulate as closely as possible the corrosion mechanisms at play. Cabinet tests are generally used to determine the corrosion performance of materials intended for use in natural atmospheres. In order to correlate test results with service performance, it is necessary to establish acceleration factors and to verify that the corrosion mechanisms are indeed following the same paths.

There are basically three types of cabinet tests.

1. **Controlled humidity test:** there are fifteen ASTM standards relating to different variations of creating and controlling fog and humidity in cabinets that are used for corrosion testing of a broad spectrum of products.

2. **Corrosive gas test:** in these tests, controlled amounts of corrosive gases are added to the humidity to replicate more severe environments.

3. **Salt spray testing:** the oldest and most wildly used cabinet test ASTM B117, introduces a spray in a closed chamber where some specimens are exposed at specific locations and angles *(Figure 2.31)*. The concentration of the NaCl solution ranges from 3.5 to 20%. Hot and humid air is created by bubbling compressed air through a bubble (humidifying) tower containing hot deionized water. The salt solution is typically moved from a reservoir, through a filter and to the nozzle by a gravity-fed system. When the hot, humid air and the salt solution mix at the nozzle, they atomize into a corrosive fog. This creates a 100% relative humidity condition in the exposure zone.

Closed chamber to produce
high humidity with salts

Corrosion coupons

Tank with a stirrer and a heater
to prepare the vaporized
corrosive solution
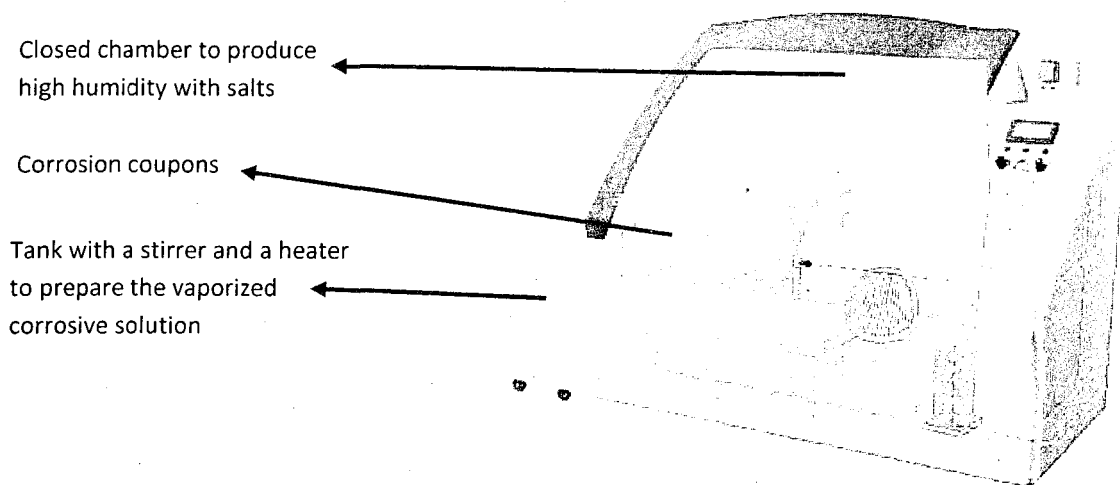
Figure 2.31: Salt spray system to simulate atmospheric corrosion (salt spray testing) on aluminum alloy coupons (Ex: Ascott Analytical Inc.)

2.3.2. Corrosion susceptibility evaluation by electrochemical tests

All laboratory corrosion tests require accelerating corrosion processes; only electrochemical tests can directly amplify the impact of corrosion processes. The main reason why this is possible is that all electrochemical tests use some fundamental model of the electrode kinetics associated with corrosion processes to quantify the corrosion rates. The amplification of the electrical signals generated during these tests has permitted very precise and sensitive measurements to be carried out. In general, electrochemical methods acquire and apply electrical potentials on samples to accelerate the corrosion phenomenon. Many electrochemical methods exist to evaluate the corrosion susceptibility of aluminum alloys but scientific works preferably use the potentiometric method *[45]*.

2.3.2.1. Potentiometric methods

Potentiometric polarization methods involve changing the potential of the working electrode and monitoring the current which is produced as a function of time or potential. Many polarization measurements exist such as «Open-Circuit-Potential», «potentiostatic polarization», «potentiostaircase», and «cyclic voltammetry». These techniques provide significant information regarding corrosion mechanisms, corrosion rates and the corrosion susceptibility.

To realize potential measurements, a potentiostat apparatus is fundamental to modern studies. This apparatus uses three electrode systems for investigations of reaction mechanisms related to redox chemistry and other electrochemical phenomena *(Figure 2.32)*. The principle of potential measurement is to identify the working electrode (WE) potential with the reference electrode potential already known. Modern potentiostats are designed to interface with a personal computer and operate through a dedicated software package. The automated software allows the user to rapidly shift between experiments and experimental conditions.
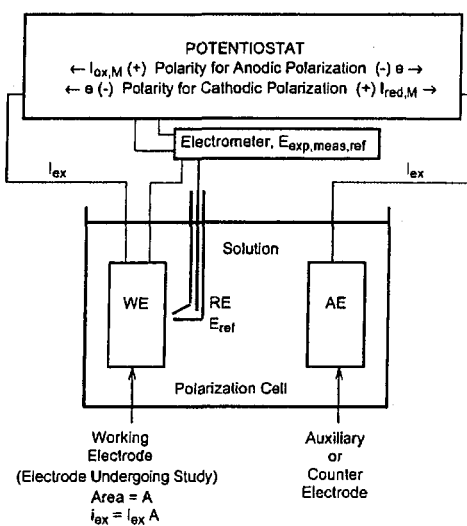
Figure 2.32: Potentiostat with three electrodes to simulate electrochemical corrosion on aluminum coupons in a corrosive solution [27]

1. **Open-circuit-potential method** (abbreviated as **OCP**, E_e or E_{corr} and referred to as the equilibrium potential) is the electrical potential between two terminals when no external loads are connected, i.e. the circuit is broken or open. Under these conditions, there is no external electrical current between the terminals, even though there may be current internally (e.g. self-discharge currents in batteries or the natural corrosion equilibrium). In many corrosion testing applications, it is advantageous to monitor the measured potential vs the electrochemical reaction time *(Figure 2.33)*. A modern potentiostat gives an easy way to acquire this information by a computer connection *[39]*.
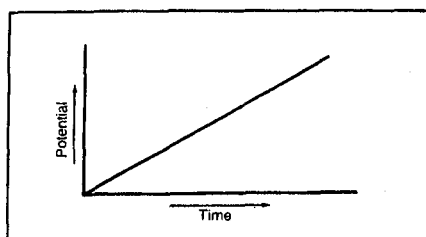
Figure 2.33: Open-Circuit-Potential (OCP) graph acquisition that demonstrates corrosion evolution mechanisms in time function [39]

2. **Potentiodynamic polarization methods** are usually performed to determine resistance to pit initiation at a given potential and to simulate galvanic situations. Precisely, potentiodynamic anodic polarization is the characterization of a metal specimen (ex: a specific aluminum alloy) by its current-potential relationship *(Figure 2.34)*. The specimen potential is scanned slowly (≈0.1mV/s) in the positive going direction and therefore acts as an anode such that it corrodes or forms an oxide coating. A complete current-potential plot of a specimen can be measured in a few hours to evaluate active-passive characteristics. Investigations such as passivation tendencies, inhibitors or oxidizers on specimens are easily performed with this technique. With this knowledge, the corrosion characteristics of different alloys can be compared on a rational basis and compatible specimen-environment combinations *[40]*.
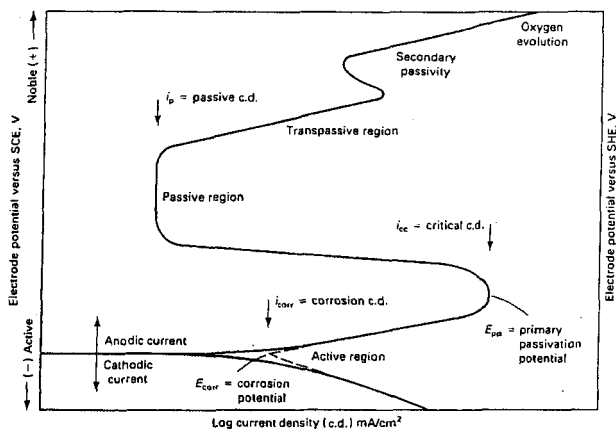
Figure 2.34: Potentiodynamic graph acquisition that demonstrates active-passive evolutions in a current applied function [40]

2.3.3. Corrosion-fatigue tests

This section is introduced to define the apparatus able to evaluate the material performance in corrosion-fatigue (CF) for aluminum alloys. A mechanical cycling stress applied on specimens surrounded by a corrosive media is ideal to appreciate the difference between cast and extruded-forged materials. This test can simulate a realistic environment where forged parts will rupture like in industrial applications. The combined test also helps to understand the synergistic effect between the mechanical and electrochemical phenomena during fatigue movements on specimens. Corrosion-fatigue standards are difficult to develop in international organizations due to the intrinsic test complexity and the many factors to control. For example, the parameterization of the corrosive environment alone is a complex variable and is difficult to be included inside a standard. The CF tests are influenced by many interactive mechanical, chemical and microstructural variables that must be factored into experimental designs *(Table 2.1)*. Only two organizations have developed standards: **ISO 11782 (1998) and ASTM F1801-04.** Another point that justifies the difficulty of simple and effective interpretations is that the CF damage is localized at the surface slip structure and near the crack tip *[45]*.

Table 2.4: Important variables to fix during corrosion-fatigue tests [40]

Metallurgical variables	Electrochemical variables	Mechanical variables
- Alloy composition - Distribution of alloying elements and impurities - Microstructure - Heat treatment - Mechanical working - Preferred orientation of grains and grain boundaries (texture) - Mechanical properties (strength, toughness...)	- Temperature - Types of environments: - Flow rate, pressure - pH, dissolved O_2 - Viscosity of the environment - Electrochemical potential - Environmental concentration - Protection: coatings, inhibitors, cathodic protection	-Maximum stress (σ_{max}) -Crack size, shape, size and geometry of components -Stress ratio ($R = P_{min} / P_{max}$) -Cyclic loading frequency -Cyclic load waveform -Load interactions in variables-amplitude loading - Amplitude - Residual stress or history

Two major categories of fatigue test can be distinguished:

1. Fatigue-corrosion tests under constant amplitude loading and testing;

2. Fatigue-corrosion tests under variable amplitude loading or realistic simulations such programmed sequence as in-service.

In the first case, the test under constant load amplitude determines the limit of endurance stress or the fatigue life to fracture. Fatigue crack growth tests can also try to measure the speed of propagation of fatigue cracks. The second case distinguishes corrosion-fatigue tests with forced loads, imposed displacements or constrained deformations. This apparatus is controlled via specific data as transferred by a computer that reproduces a precise cyclic effect on specimens. Practically, cyclic loading methods are normally categorized according to the nature of the applied forces by the apparatus. Thus, there are several force types to impress on specimens: plane bending, rotating bending, axial, torsion or combined forces. Some apparatus can even simultaneously test the types of solicitations.

A typical fatigue test specimen has three areas: the test section and two grip ends. The grip ends are designed to transfer the load from the test machine grips to the test section and may be identical, particularly for axial fatigue tests.

The transition from the grip ends to the test area is designed with large, smoothly blended radii to eliminate stress concentrations in the transition. The design and type of the specimen depends on the fatigue-testing machine and the objective of the fatigue study. The test section in the specimen is reduced in cross section to prevent failure in the grip ends and should be proportioned to use the middle to upper ranges of the load capacity of the fatigue machine.

Many accessories are important to be considered during corrosion-fatigue tests. They include a fluid circulation pump, a gas diffuser system, a thermostated solution, a sampling bottle by-pass, and pH-%O$_2$-conductivity meters [41, 43]. For instance, oxygen or nitrogen gases can be injected into the corrosive solution respectively to enrich or deaerate the oxygen content. The oxygen content can change the cathode reactions during the corrosion phenomenon and modifies the corrosion susceptibility of different aluminum alloys. Therefore, the corrosion chamber must be ready to accept pipes to distribute gas into the solution *(Figure 2.35).*
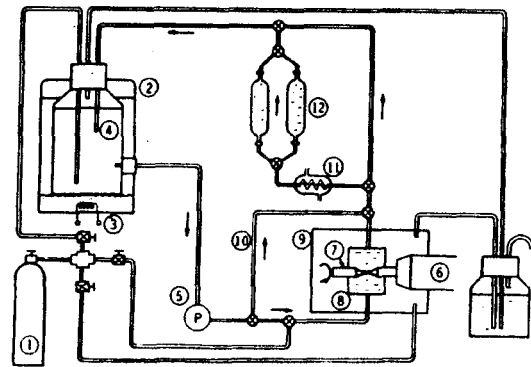
① Nitrogen gas supply   ⑦ Specimen
② Thermostat   ⑧ Corrosion chamber
③ Heater   ⑨ Cover for N$_2$ gas seal
④ Closed reservoir   ⑩ By pass
⑤ Magnet pump   ⑪ Cooler
⑥ Fatigue testing machine   ⑫ Sampling bottle

Figure 2.35: Example of a corrosion-fatigue set-up with fluid-gas circulation, deoxygenating and thermostated possibilities [41].

3

EXPERIMENTAL

The material preparation began with the production of AA6082 aluminum billets by a direct chill (DC) casting technique. All cast billets were subject to a homogenizing treatment. Half of these aluminum cast billets were hot-extruded. Both as-cast and extruded feedstock materials were then hot-forged with an optional -T6 heat treatment. Three complementary experiments were performed to identify the corrosion susceptibility: 1) electrochemical measurements, 2) salt spray exposures and 3) corrosion-fatigue tests. *Figure 3.1* presents material preparation ways to be used for the corrosion tests.

PREPARATION OF ALUMINUM FORGING MATERIALS

| CASTING of AA6082 aluminium billets by a DC casting technique | → | HOMOGENIZING treatment of AA6082 aluminium as- cast billets | → | 1) As-cast Feedstock |
| | | Hot EXTRUSION of AA6082 aluminium cast billets | → | 2) Extruded Feedstock |
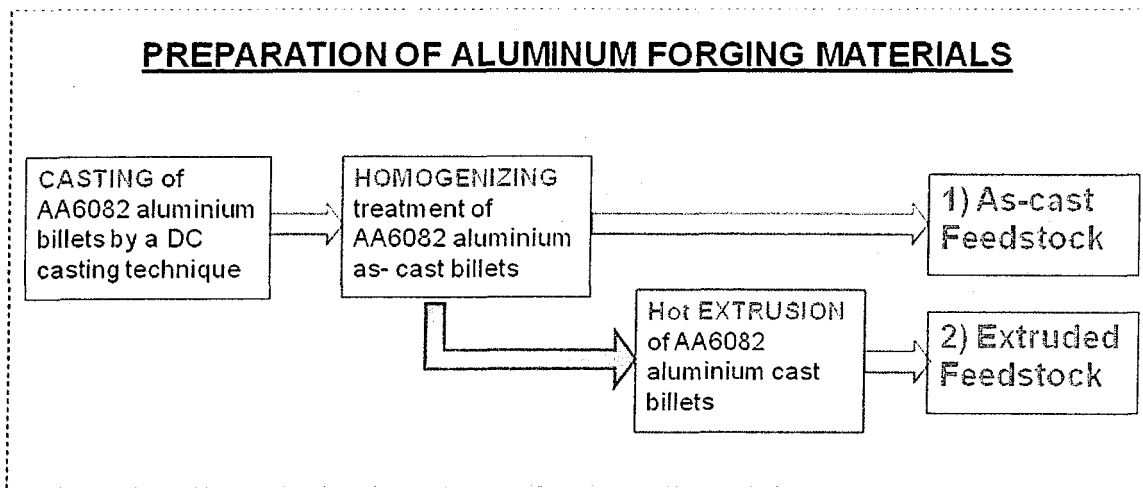
Figure 3.1: Experimental flow of materials preparation as forging feedstock

3.1. Materials preparation

3.1.1. AA6082 aluminum cast billets

The 76 mm diameter billets were cast using a gas-assisted direct chill (DC) casting technology. The chemical composition of the DC cast billets as a typical AA6082 alloy is given in *Table 3.1*.

Table 3.1 Nominal composition for AA6082 aluminum cast billets (wt.%)

% Elements	Si	Fe	Cu	Mn	Mg	Cr	Ti
Cast billets	0.98	0.13	0.08	0.48	0.77	0.13	0.01

3.1.2. Homogenizing and extrusion of cast aluminum billets

All billets underwent a homogenizing treatment at 540°C during four hours. After homogenization, a part of billets was directly used as an as-cast feedstock for forging. Parameters of the homogenization treatment are:

- 200°C per hour until 490°C;

- 50°C per hour until 540°C;

- Maintaining at 540°C the homogenization during four hours;

- Decreasing 100°C per hour during the cooling.

Half the billets were heated to 520°C by an induction system and extruded in a 25.4 mm (1 inch) round bar product. The extrusion speed was fixed at 45 m/min to produce a good surface quality. This material was employed as an extruded feedstock for the next forging process *(Figure 3.2)*.

| a) AA6082 aluminum as-cast billet | b) AA6082 aluminum bar after the extrusion |
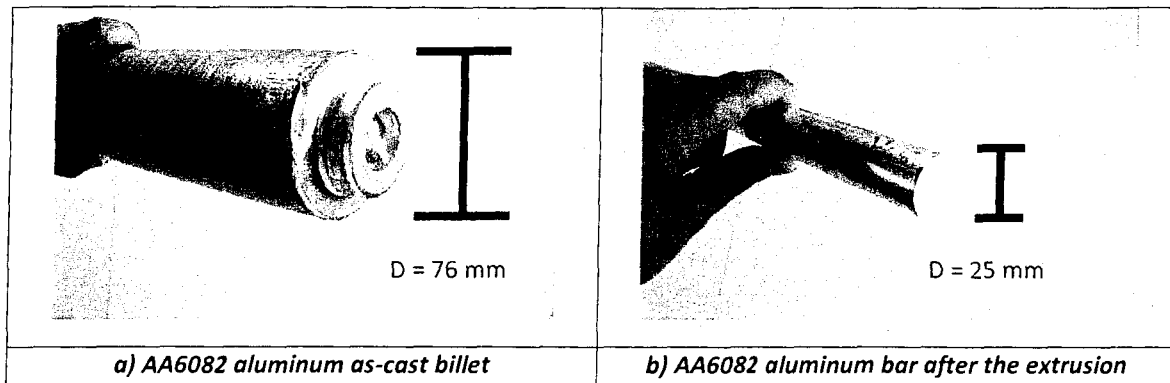
Figure 3.2: Feedstock materials for further thermomechanical treatments

3.1.3. Forging of feedstock materials (cast and extruded)

The apparatus used to forge corrosion coupons was a machine called "crank press". The maximum capacity of this machine is approximately 500 tons. The mechanical press type works by using cams, cranks and/or toggles to produce a preset stroke (a predetermined force at a certain location in the stroke, *Figure 3.3a*). Due to the nature of this type of system, different forces are available at different stroke positions for the forging press. Metal forming parameters were defined in order to represent industrial conditions that happen during the forge process. Thermal and deformation parameters during the forge process are listed below:

1. Preheating temperature of specimens: $\approx 500°C$;

2. Forging die temperature : $\approx 230°C$;

3. Specimen temperature after forging: $\approx 350°C$;

4. Graphite lubricant in water colloidal suspension spayed with 0.2 w/v% of solid content;

5. Total strain during hot forging $\varepsilon = 1$;

6. Strain rate = $\approx 10 \, s^{-1}$ for a forging crank press;

7. Aspect ratio (Length / Diameter) of specimens: 1.5.

Plane strain orientation was used during the forging sequence to produce flat and elongated samples

(5" x 3"). This geometry was also used to machine the corrosion coupons *(Figure 3.3b)*.

| *a) AJAX © 500 tons crank press* | *b) Feedstock materials forged by the crank press* |
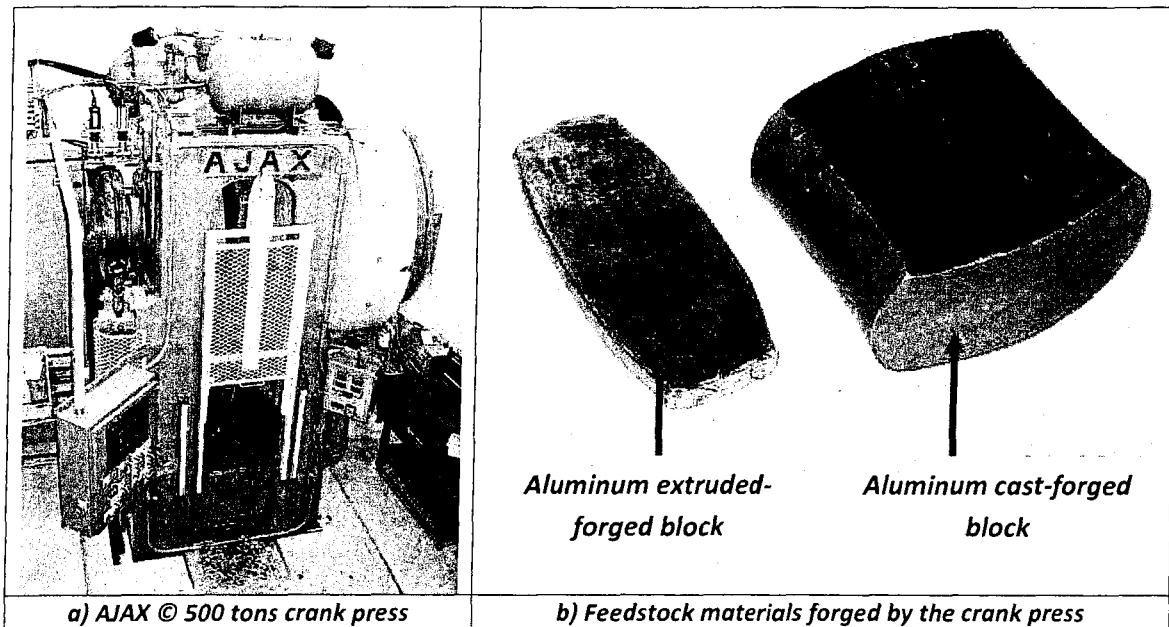
Figure 3.3: Mechanical forging press used to prepare corrosion coupons

3.1.4. T6 Heat treatment on forged products

The T6 heat treatment was done on forged parts to improve the mechanical properties and to respect the industrial method. The T6 parameters are:

- Solutionizing temperature at 550°C during one hour;

- Water quenching within five seconds;

- Artificial aging temperature at 170°C during eight hours.

3.2. Corrosion testing on forged materials

Due to the presence of several conditions of feedstocks, it was necessary to set relative identification numbers for further experiments. The following list contains the metallurgical classification for microstructural characterizations and corrosion tests.

1. Condition as-cast;

2. Condition cast homogenized;

3. Condition cast homogenized + hot forged;

4. Condition cast homogenized + hot forged + T6;

5. Condition cast homogenized + extruded + hot forged;

6. Condition cast homogenized + extruded + hot forged + T6.

Three types of corrosion tests were chosen to evaluate the corrosion susceptibility of the forged materials. The list of corrosion tests performed in order to have a good comparison between the feedstock materials follows *Figure 3.4.*
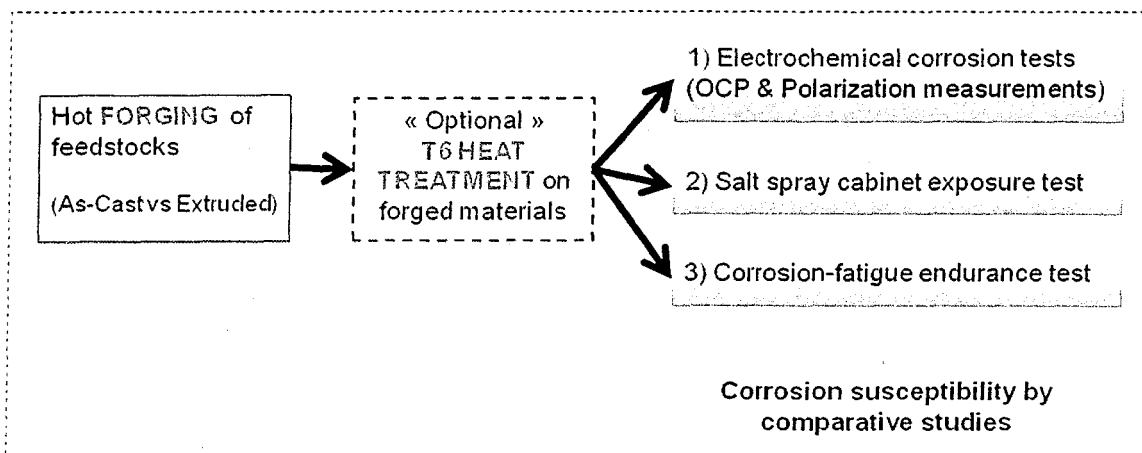
Figure 3.4: Experimental view of forging and corrosion testing samples preparation

Electrochemical and salt spray tests are the most commonly and wide-spread corrosion tests used in the world. These tests have a long history, with a lot of test data available relating to the expected corrosion resistance for a wide variety of materials and surface coatings. The corrosion-fatigue test combines simultaneous corrosion and mechanical stresses to evaluate the synergistic effect on forged materials. *Note: all the forged materials kept the original surface from feedstock. No machining was allowed on the original surface*.

3.2.1. Electrochemical corrosion tests: OCP and anodic polarization curves

Two electrochemical methods (**O**pen **C**ircuit **P**otential and anodic polarization tests) were used to study the corrosion susceptibility of different metallurgical conditions, especially between as-cast and extruded feedstocks. The followed procedure for electrochemical tests was developed by the ASTM organization and referred to as *"G5-94 Standard Reference Test Method for Making Potentiostatic and Potentiodynamic Anodic Polarization Measurements"*. The ASTM test method covers the experimental techniques and instrumentation.

The open circuit potential (OCP) was monitored during 24 hours in a 3.5 w/v% sodium chloride solution especially deaerated with a minimum flowrate of nitrogen bubbling at 2.5 L/h. Agitation was only performed by the natural convection of bubbling gas. This step was necessary to stabilize the corrosion phenomenon at the equilibrium before the next anodic polarization test. Five tests were repeated for each metallurgical condition. A flat corrosion cell with a calomel reference and with platinum-niobium counter electrodes were used to determine the electrochemical potentials. The circular surface area tested during the corrosion test was approximately 12.9 cm^2 (2 square inches). The corrosion potential at equilibrium (E_{corr}) was precisely determined with the OCP test. *Figure 3.5* shows the electrochemical setup to obtain the corrosion potential data.
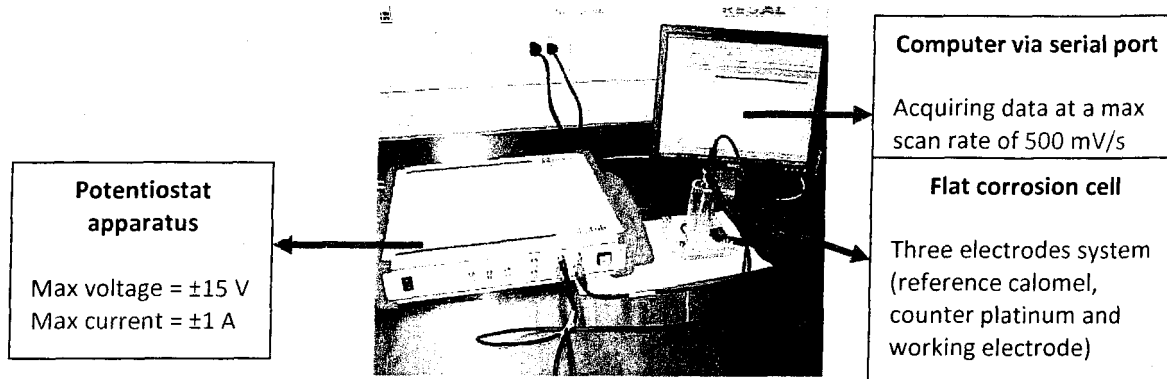
Figure 3.5: Electrochemical system made from Radiometer© that identify the corrosion susceptibility of forged materials by potential and current measurements

No glass luggin capillary was used to act as a salt bridge between the saturated calomel reference electrode and the corrosion coupon. When added, the bridge tube in the cell setup has produced important IR drops (ohmic potential drop) that induced an important decrease in magnitude of current during corrosion testing. Specific cares was taken to minimize the effect of luggin capillary elimination as a large scale convective mixing in the cell solution. Particularly, the use of a fritted porous plug reference electrode with a minimal distance adjustment between electrodes can be helpful. Also, a low scan rate during the polarization test allows a good sensitivity operation of potentiostats.

After 24 hours of acquisition, anodic polarization was applied on specimens to evaluate the susceptibility of the critical pitting corrosion potential (E_{pit}). This test can also determine critical electrochemical values such as corrosion current (I_{CORR}), pitting corrosion current (i_c), passivation current (i_p), passivation voltage (E_{pass}), transpassive voltage and repassivation voltage (E_R). The shutdown criteria was the maximum output current possible to deliver using the potentiostat with 1 Ampere. In this case, the maximum current density applied on the samples was approximately 100 mA/cm^2. A scan rate of 2 mV/s was used to sweep the anodic polarization curve.

3.2.2. Salt spray corrosion exposure tests

The salt spray test is a standard method used to verify the corrosion resistance of samples. This test is an accelerated corrosion test that produces a corrosive attack on the samples in order to predict its suitability in use as an industrial part *(Figure 3.6a)*. The appearance of corrosion products (oxides) is evaluated after a period of time *(Figure 3.6b)*. The most important ASTM standard is the *"ASTM B117-03 Standard Practice for Operating Salt Spray (Fog) Apparatus"*.

This practice covers the apparatus, procedure, and conditions required to create and maintain the salt spray (fog) test environment. The solution must be prepared with high grade sodium chloride with pure water conforming to Type IV water in the ASTM D-1193 standard. Some modifications in the ASTM B117 standard were made to compare the results with other corrosion tests; the temperature was adjusted 21 ± 1°C (normally 30°C) and the salt concentration percentage was changed to 3.5 w/v% (normally 5% w/v).

| *a) Setup to produce atmospheric corrosion by mixing water - salts* | *b) AA6082 as-cast coupon* |
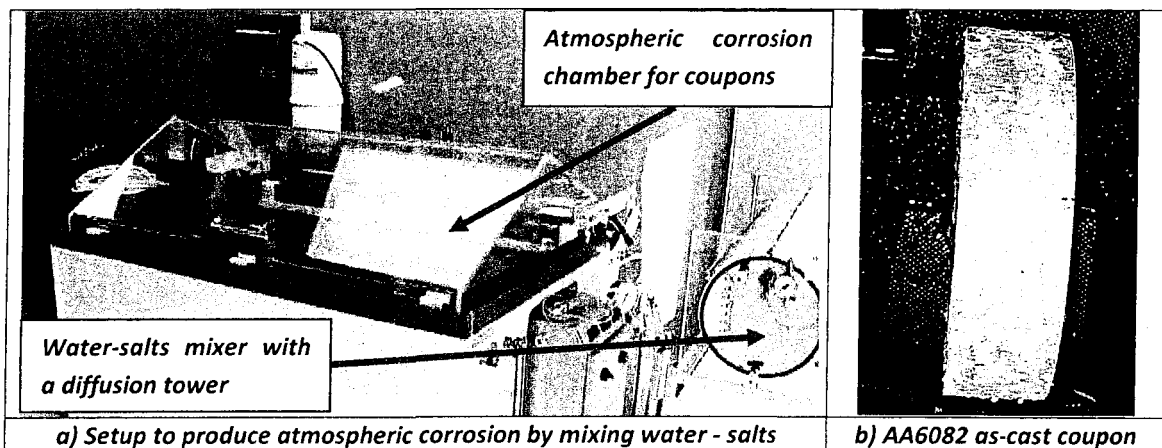
Figure 3.6: Singleton © salt fog spray apparatus and specimen example with corrosion products after 168 hours of exposure time

Two complete sets of forged parts were tested for each metallurgical condition in the salt spray apparatus. After two and four weeks of exposure times, the corroded specimens were removed from the salt spray cabinet in order to compare and identify which were the most susceptible to pitting and other corrosion types *(Figure 3.6b)*. A mechanical brushing and a chemical etching in H_3PO_4 solution were applied on corroded specimens to eliminate the alumina deposits in the pits. This step was in conformity with the ASTM standard *«G1-03 Standard Practice for Preparing, Cleaning, and Evaluating Corrosion Test Specimens» (Table 3.2). The* Clemex[©] image analysis software was used to precisely determine important corrosion information.

Table 3.2: ASTM G1-03 chemical cleaning procedure to remove oxide products after corrosion testing

Designation	Material	Solution	Time	Temperature	Remarks
C.1.1	Aluminum and Aluminum Alloys	50 mL phosphoric acid (H_3PO_4, sp gr 1.69) 20 g chromium trioxide (CrO_3) Reagent water to make 1000 mL	5 to 10 min	90°C to Boiling	If corrosion product films remain, rinse, then follow with nitric acid procedure (C.1.2).

3.2.3. Corrosion-fatigue tests

Aluminum forged parts are often solicited with high mechanical stresses in constrained environments (ex: suspension arms, motor parts, locomotive drive train, bike fasteners, etc.). For this reason, a mechanical cycling stress applied in a corrosive environment can estimate the synergistic effect between the corrosion degradation and fatigue deformation that happen on these parts. The corrosion-fatigue experiment is ideal to simulate real conditions where forged parts are used. This apparatus will help identify which mechanical and electrochemical mechanisms are prominent during specimen ruptures (see **Figure 3.7**). Based on a flat geometry of forged specimens as mentioned in the above section, the pure flexural movement was the most suitable to evaluate these fatigue specimens with «forged skin». In order to answer the main thesis objective, the flat geometry avoids the need to machine the skin on forged blocks.

Lever arm and specimen holder are made in a 304 stainless steel alloy to resist at 3.5% w/v NaCl solution and to test flat specimen geometries.
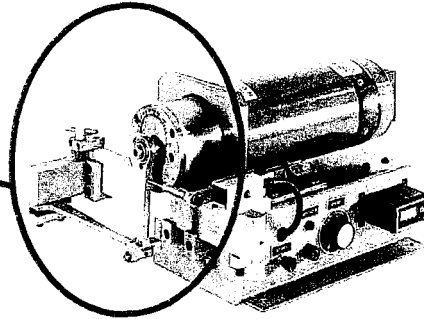
Figure 3.7: A typical bending fatigue machine sold by many companies (Ex: Fatigue Dynamic inc ©.)

Flexural fatigue test specimens must have small and precise dimensions to extract them from flat forged parts. Overall tolerance on the fatigue specimen drawing was within 0.0127 cm and tighter in the rupture zone with 0.00254 cm *(Figure 3.8)*. In particular, the extruded feedstock material has only a 2.54 cm diameter before the forging step that can cause a problem during machining. The dimensions for the flexural fatigue specimens are seen in Figure 3.8b. Also, the original surface of the extruded and cast materials was kept on only one side to evaluate the surface reactivity (with and without the original skin) with corrosive environments.

a) Fatigue specimens extracted from the machined block of the cast-forged material	b) Fatigue specimen drawing with specific dimensions (inches)
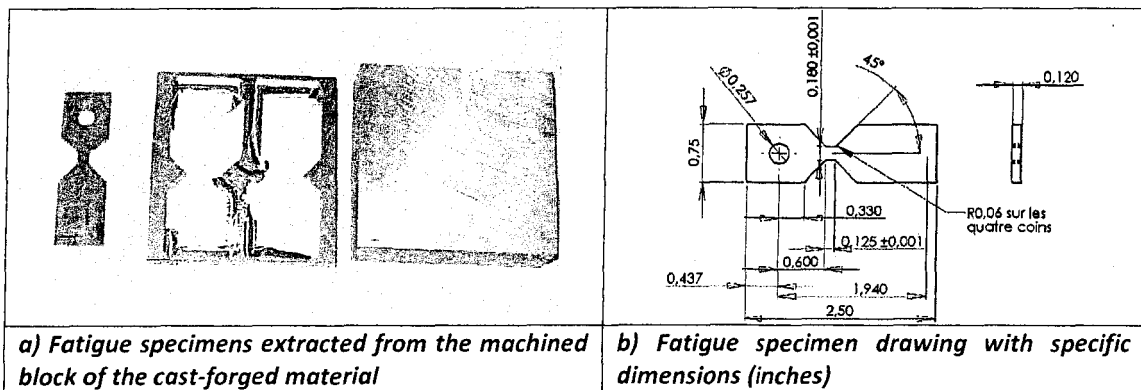
Figure 3.8: Fatigue specimen extraction from machining and its dimensional tolerances

Specimens can undergo a maximum vertical displacement of 5.08 cm. A vertical adjustment between 0.254 cm and 0.508 cm represents a fatigue stress interval of 70 to 150 MPa. The incorporation of specimens into the apparatus is possible and they are simultaneously bent during the fatigue cycling. A low fatigue frequency was tried in order to make the intimate contact duration between the corrosive solution and fatigue specimens as long as possible. Finally, the use of 4 specimens at the same time during the experiment increases the reproducibility of results. A gas flowing system is important to be considered during the corrosion-fatigue experiment. This parameter can accelerate or decrease the corrosion susceptibility of the fatigue specimens tested. A nitrogen gas was respectively introduced into the corrosive solution to deaerate the oxygen content. As mentioned in the literature review, the oxygen content modifies cathodic reactions during the corrosion phenomenon.

The immersion tank must be ready to accept gas pipes to dispense the gas flow into the corrosive solution *(Figure 3.9)*. High gas flowrates during the experiment can have negative effects (erosion, bubbles, turbulence, etc.) on corrosion results, reproducibility and predominant corrosion mechanisms. However, a low fluid velocity can increase stuck bubbles on the surfaces and create cavitation effects or differential oxygen concentrations. To avoid these problems, a minimum flowrate of 2.5 L/h was maintained.
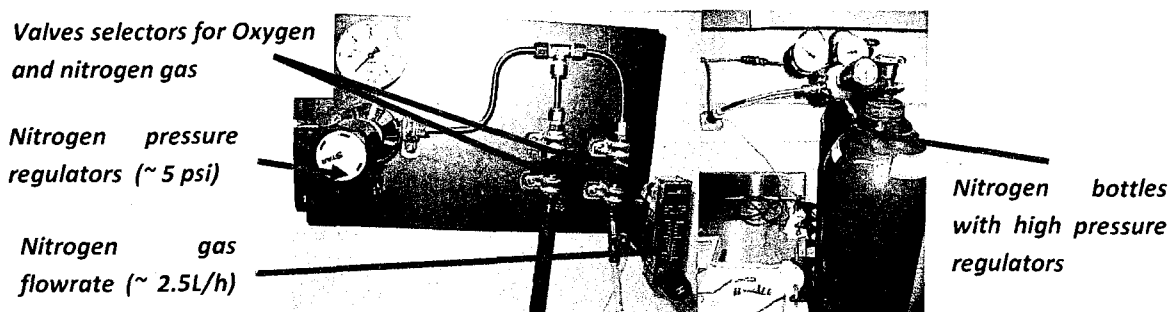
Figure 3.9: Nitrogen gas distribution system at the CURAL lab for the corrosion-fatigue apparatus

If more than one specimen is tested during the same fatigue experiment, a shutdown and a scanner controller are required for each sample. These four counters *(Figure 3.10)* are necessary to estimate the number of cycles done for each specimen. To realize this, a relative rupture criterion of 60% of the initial stress applied was used to acquire the total cycling number of each specimen.

Electrical motor 120 V

Samples and holder

Solution tank for corrosion solution immersion

System shutdown controller for specimens

Scanner controller to count number of cycles
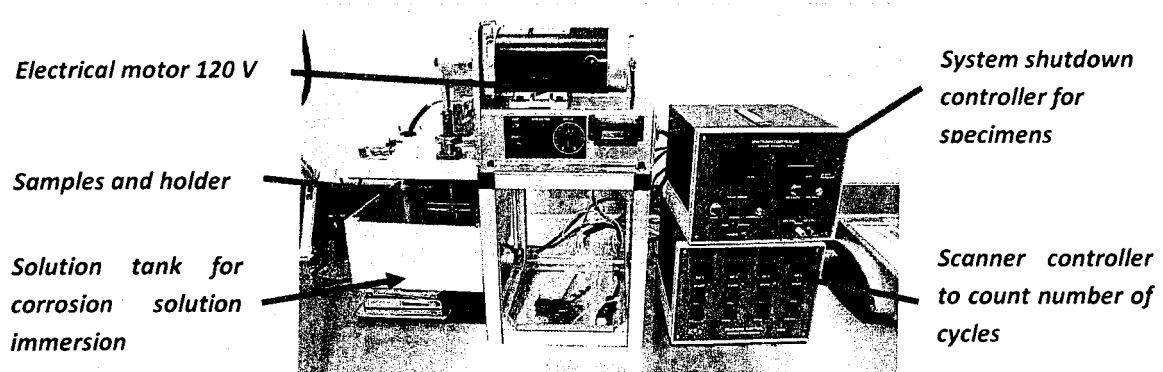
Figure 3.10: 4 samples flexural bending fatigue apparatus made by Fatigue Dynamic inc© with a corrosion immersion cell

3.2.4. Design of corrosion-fatigue experiments (*DOE*)

A design of experiments was elaborated in order to evaluate the most important variables. The following list shows the experimental parameters to compare the feedstock materials.

Variable parameters during the corrosion-fatigue tests:

- Magnitudes of fatigue stress applied on specimens (70, 90, 110 and 140 MPa);

- Types of fatigue environment (NaCl 3.5%w/v and air);

- Feedstock materials (as-cast and extruded materials).

Fixed parameters during the corrosion-fatigue tests:

- Solution temperature   →   21°C;

- N_2 bubbling flowrate   →   2.5 Liters per hour;

- Specimen rugosity   →   Low ($R_a \leq 1$ μm);

- Cycling frequency   →   4Hz.

To create Wöhler curves with four induced stresses, a minimum of 20 specimens (four for each condition) was tested to increase the reproducibility of the results.

3.3. Materials characterization

3.3.1. Microstructural evolution: Optical and SEM microscopies

1) Feedstock materials analysis: It is anticipated to evaluate properties and corrosion susceptibility of two different forged materials, namely the as-cast and the as-extruded materials. The microstructural analysis was done on these feedstock materials to understand the microstructural evolution during the forging process and the T6 heat treatment. Many aspects were evaluated during the microstructural investigation. For instance, macro and microstructural patterns, defects presence, grain sizes, precipitated phases and superficial layers are some matters that were analyzed. Modified Poulton's and Tucker's etchants were used to realize macroscopical examination of orientations, boundaries and quantities of α-Al grains **(Table 3.3)**. A JEOL JSM 6480LV SEM microscope equipped with an EDX energy system 250 from OXFORD INCA unit was used to define the special surface layers present in extruded and cast materials.

Table 3.3: Chemical etchants used for macroscopic examinations of AA6082 aluminum specimens [42]

Tucker's reagent	Modified Poulton's reagent
- 45 ml HCl (37 v/v% conc)	- 30 mL HCl (37 v/v% conc)
- 15 ml HNO$_3$ (70 v/v% conc)	- 40 mL HNO$_3$ (70 v/v% conc)
- 15 ml HF (48 v/v% conc)	- 2.5 mL HF (48 v/v% conc)
- 25 ml H$_2$O	- 12 g CrO$_3$
	- 42.5 mL H$_2$O

Optical metallography was performed on AA6082 feedstock materials and the following observations were noted:

- Grain patterns such as columnar, deformed or equiaxed grains;

- Special surface layers (segregated layers and peripheral grain layers);

- Bulk and surface anomalies for each metal forming processes during the material preparation (ex: blisters, tears, oxides, void, etc.);

- Presence of secondary phases (ex: Mg$_2$Si, Al-Fe-Mn-Si compounds, Eutectic silicon, etc.).

2) Forged materials analysis: After the first microstructural analysis was completed to determine the characteristics of cast and extruded materials, a second examination was accomplished on the final forged products. In addition, this microstructural analysis was the starting point in order to understand «how» corrosion and fracture mechanisms initiated and propagated into the microstructure of the materials.

3) Corroded specimen analyses : Optical and SEM microscopies were used in conjunction after corrosion testing to link the corrosion results (electrochemical curves, salt spray pits, corrosion-fatigue fractured surface) with the microstructural damages. For the corrosion pits, macrophotographs were acquired and processed with a quantitative image analysis software (CLEMEX©). For example, the relative percentages of pits, number of pits, aspect ratio, corroded areas, length and width of corrosion pits were measured. Metallographically cut profiles of corroded surfaces allowed the evaluation of the pitting depth. The optical image **(Figure 3.11)** shows colored pits at the surface of the corroded parts. Several parameters and calculations were carried out starting from these images. A minimum of 30 fields for each metallurgical condition were analyzed to obtain representative and reproducible results. Microphotographs obtained by the SEM microscope evaluated the non-visible pits, the specific geometry of corrosion propagation, the local pit densities and the initiation points.
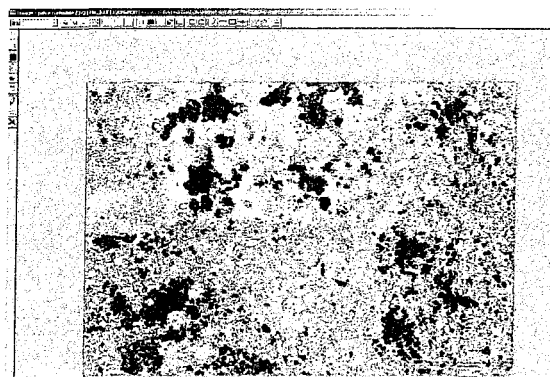
Figure 3.11: Quantitative image analyses with corrosion pits recognition in blue by the Clemex© routine

4

RESULTS AND DISCUSSION

4.1. Characterization of feedstock

4.1.1. Microstructural analysis of feedstock materials

As-Cast material: In general, as-cast feedstock has an equiaxed grain structure, which is a typical macrostructure, produced in the vertical DC cast billets *(Figure 4.1)*. However, the surface and the core areas of cast billets have distinctive microstructural features due to an uneven solidification process. A modified Poulton etching on samples revealed a uniform cast structure in the inner central zone of the AA6082 cast billet.
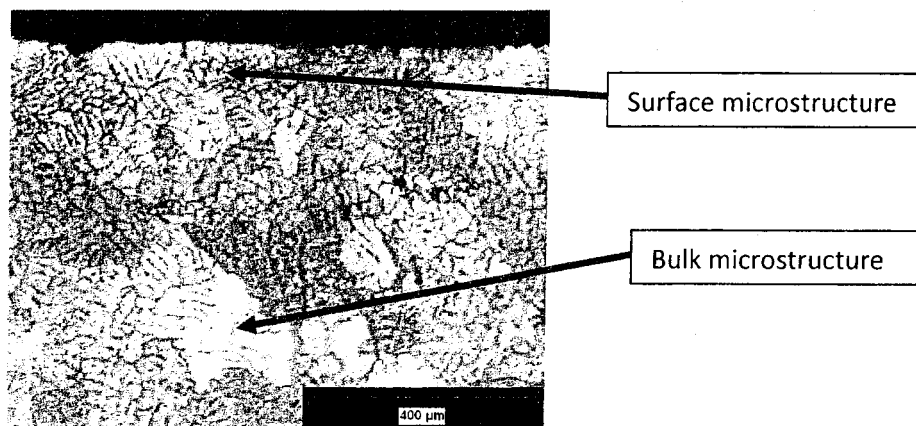
Figure 4.1: Optical macrograph of AA6082 as-cast aluminum material with a uniform grain structure (Modified Poulton etchant, 50X)

Direct chill casting techniques usually induce non-equilibrium freezing within the ingot. Non-uniform solidification introduces a segregation layer in the casting surface. **Figure 4.2a** shows an inverse segregated layer at the surface of the as-cast feedstock. The presence of many intermetallic compounds was detected as seen in **Figure 4.2b**. The enriched layer thickness was measured with an average of 129 µm.

a) Presence of inverse segregated layer on the as-cast material (Tucker etchant at 100X magnification)	*b) Presence of intermetallics compounds in the enriched surface layer (no etching, 500X magnification)*
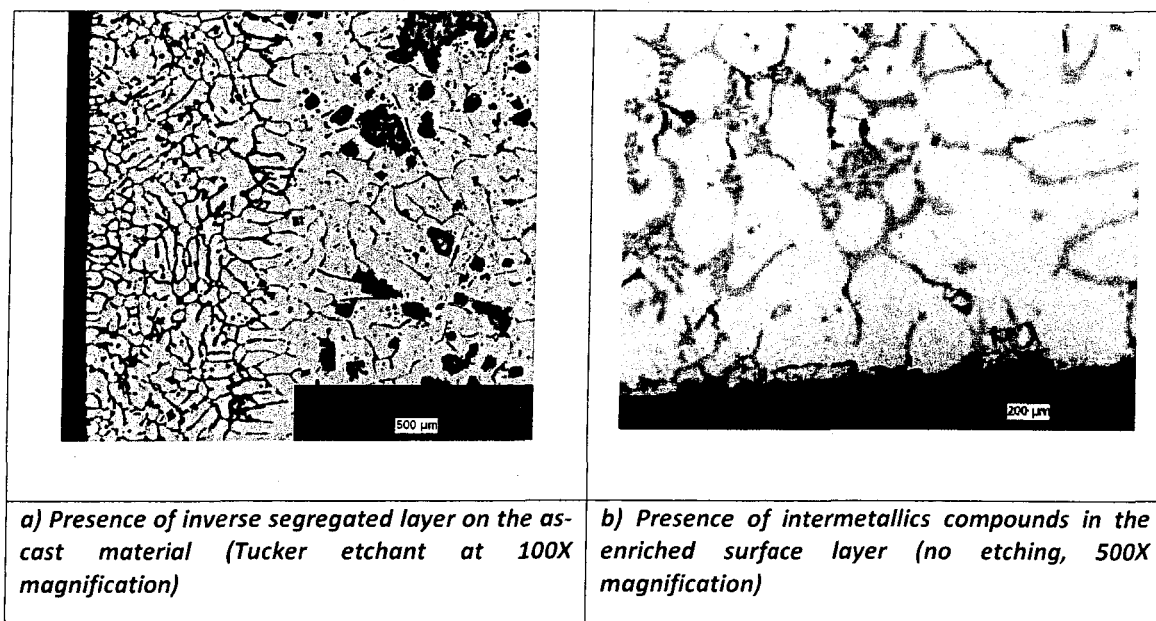
Figure 4.2: Optical micrographs of AA6082 as-cast aluminum revealing the segregated layer presence with rich intermetallic compounds.

As-extruded material: The extruded material has a fibrous and non-recrystallized grain structure except at the surface. **Figure 4.3a** displays a highly fibrous structure in the inner central location of the extruded bar.

| a) **Metallographic longitudinal profile with elongated and deformed grains (50X magnification)** | b) **Metallographic transversal profile with two different microstructures: bulk and surface zones (50X magnification)** |
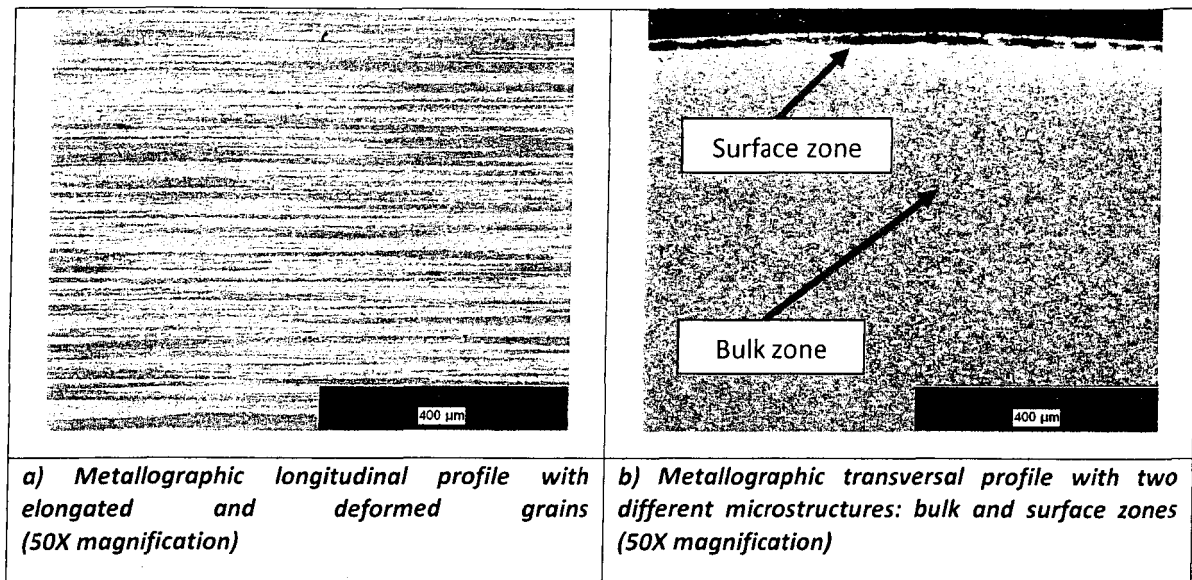
Figure 4.3: As-extruded AA6082 feedstock revealing an elongated structure with different microstructural zones (Modified Poulton etchant, 50X magnification.)

Two different microstructural zones have been detected in the extruded material *(Figure 4.3b)*. They are referred to as specific deformation zones during the extrusion process. The significant thickness of the surface layer and the related through-thickness inhomogeneity in grain structure and crystallographic texture seem to constitute the particular features of the extruded profiles.

The extruded material displays a fiber-like and non-recrystallised grain structure. The thin layer at the surface is often called the *«Peripheral coarse grain layer (PGL)» (Figure 4.4a)*. The peripheral grain layer at the surface is produced by high mechanical deformation ratios and significant temperatures that will produce enough energy to redefine the shell zone by a recrystallization process *(Figure 4.4b)*. Quantitative thickness measurements on transversal profiles give a thickness mean equal to 108.15 μm related to the peripheral coarse grain layer *(Figure 4.5)*.

| a) As-extruded feedstock with the «Peripheral Coarse Grain Layer» (50X magnification) | b) Peripheral grain layer (PGL) with recrystallized grains (200X magnification) |
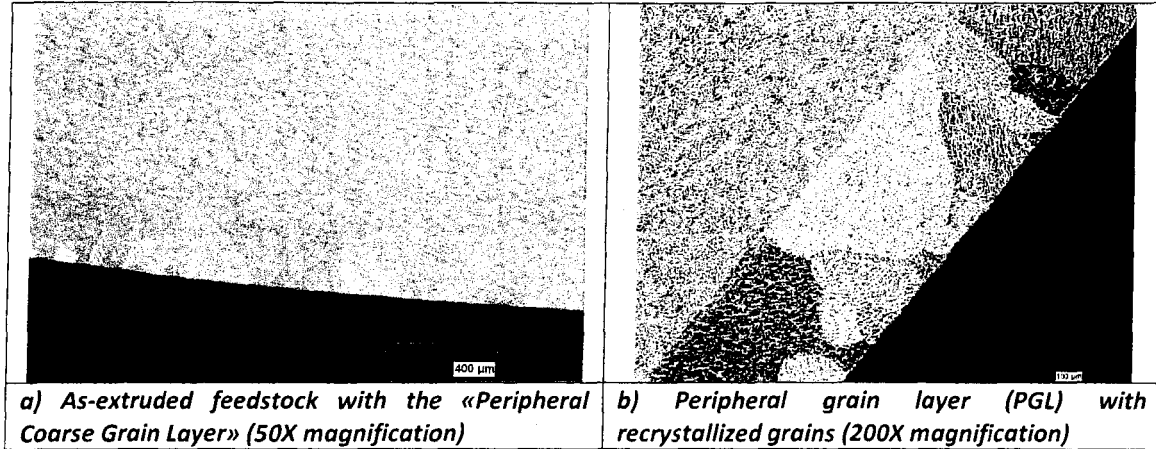
Figure 4.4: Transversal micrographs of AA6082 aluminum extruded material exhibiting the presence of a recrystallized grain structure at the surface (Modified Poulton etchant)
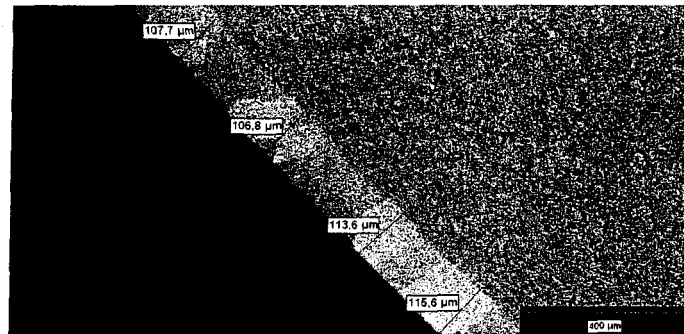
Figure 4.5: Peripheral grain layer thickness measurements on extruded AA6082 aluminum profiles (Modified Poulton etchant, 50X magnification)

Fine, round and black Mg_2Si constituents are found everywhere in the extruded microstructure but a number of bigger Mg_2Si constituents were found around the thinnest zone at the surface. Micrographs revealed that the Peripheral coarse grain layer (PGL) contains larger Mg_2Si precipitates *(Figure 4.6)*. Coarse Mg_2Si particles in the PGL zone can cause low hardness, increase pick-up on the extruded surface, and influence the corrosion phenomenon.
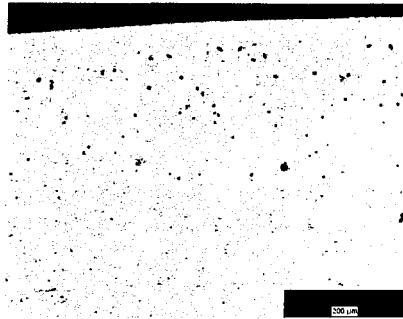
Figure 4.6: Micrograph of AA6082 extruded bar showing round and larger Mg₂Si particles near to the PGL

zone (No etching, 100X magnification)

A further SEM examination shows the transition between the inner core microstructure and the peripheral grain layer at the surface *(Figure 4.7)*.
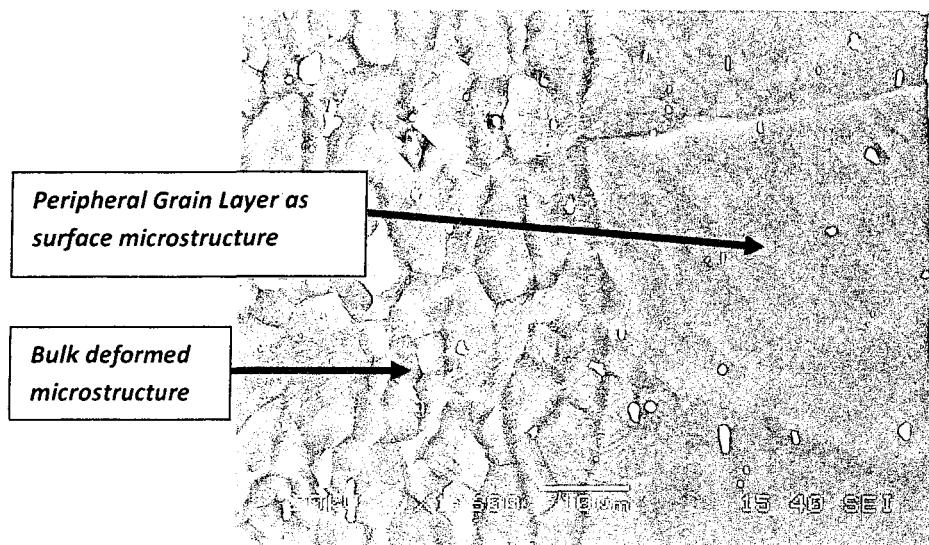
Figure 4.7 SEM micrograph of an as-extruded AA6082 aluminum alloy profile exhibiting the transition

between the internal core microstructure and the Peripheral Grain Layer (PGL) (Modified Poulton etchant,

1600X magnification, 20 KeV, SEI source)

4.1.2. Chemical EDX analysis of secondary phases in feedstock materials

As-Cast material

First, a local analysis of the white phase revealed a composition containing aluminum, silicon, iron and manganese elements. These data are similar to the α-Al_8Fe_2Si phase which has an irregular shape *(Figure 4.8)*.

White and irregular Al-Si-Fe-Mn phase	
a) Local analysis of the white irregular phase	*a) Elements found in the white irregular phase*
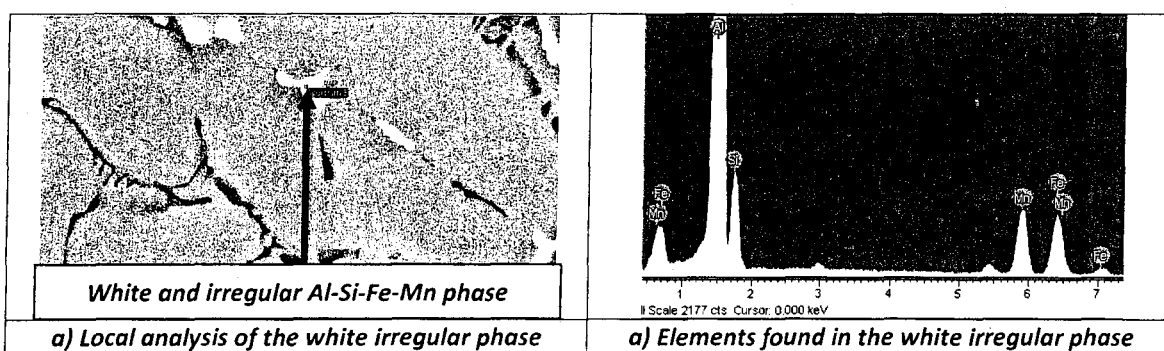
Figure 4.8: SEM micrograph and EDX spectrum analyses of the white irregular phase

Secondly, an EDX analysis of the dark phase shows mainly aluminum, magnesium, and silicon constituents. These data suggest the stoichiometry of the Mg_2Si phase. This phase has a needle form with a black color that corresponds to the micrographs obtained *(Figure 4.9)*.

Black and acicular Mg-Si phase	
a) Local analysis of the black needle phase	*a) Elements found in the black needle phase*
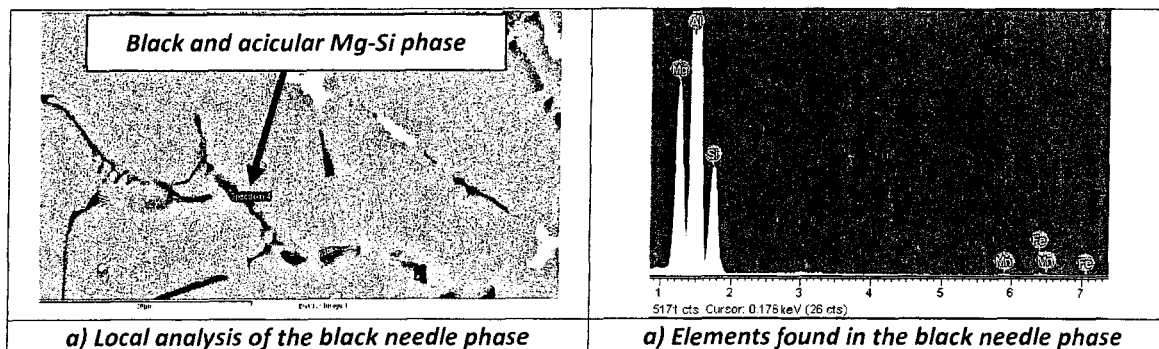
Figure 4.9: SEM micrograph and EDX spectrum analyses of the black needle phase

Thirdly, an analysis conducted on the elongated white phase revealed aluminum, silicon and some iron and manganese elements *(Figure 4.10)*. These results have a chemical similarity with the stoichiometry of the β-Al₅FeSi phase. The β-AlFeSi phase normally has a harmful effect on the hot working characteristics. The α-phase with an irregular round shape is less damaging than the beta elongated phase for the plastic deformation of aluminum alloys.

a) Local analysis of the white needle phase	a) Elements found in the white needle phase
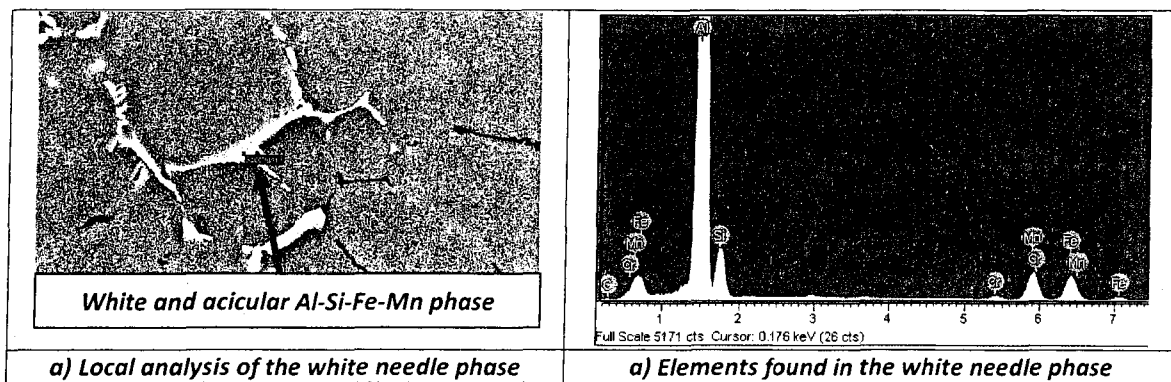
Figure 4.10: SEM micrograph and EDX spectrum analyses of the white needle phase

In addition, the presence of eutectic silicon was found. The chemical mapping reveals the presence of this element at the grain boundaries in as-cast alloys *(Figure 4.11)*.

a) Global %Si analysis in the microstructure	a) Silicon mapping in the microstructure
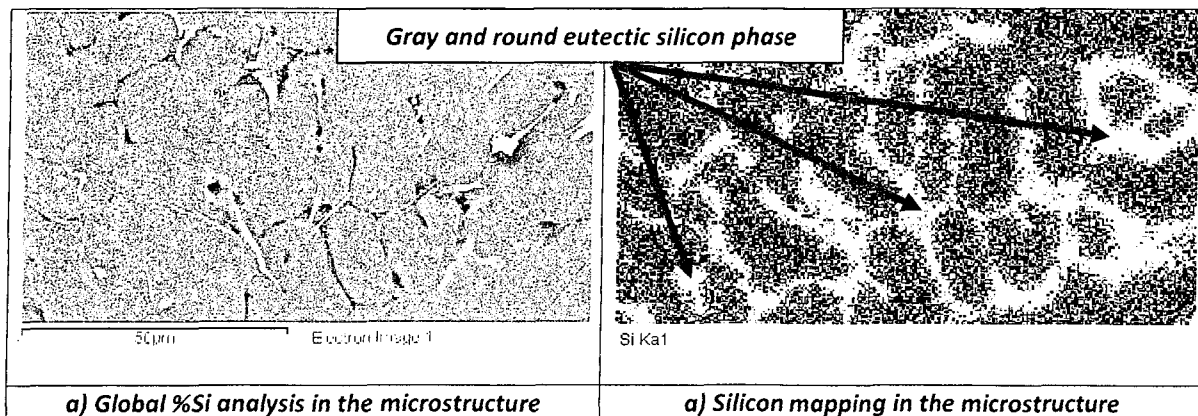
Figure 4.11: SEM micrograph and chemical mapping on the Si elements

4.2. Characterization of forged products

4.2.1. Microstructural analysis of forged materials

Cast-forged material: By default, cast material has an equiaxed grain structure where the forging process will flatten all grains perpendicular to the force direction *(Figure 4.12)*.
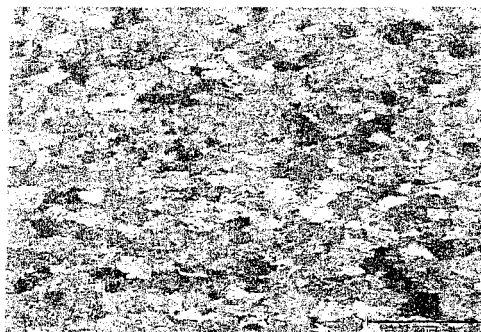
Figure 4.12 Optical polarized macrograph of a cast-homogenized AA6082 aluminum billet that was hot forged (Modified Poulton etchant, 50X magnification)

Optical micrographs show that the microstructure contains coarse Mg_2Si precipitates with an elongated shape at the grain boundaries *(Figure 4.13)*. A surface investigation exposes the presence of several coarse phases with irregular shapes. The concentration of these constituents remains even higher on the surface when compared to the center zone *(b))*.

a) Presence of round and black Mg₂Si constituents in the cast-forged material (200X magnification)	b) Same constituents are positioned mainly at the grain boundaries (500X magnification)
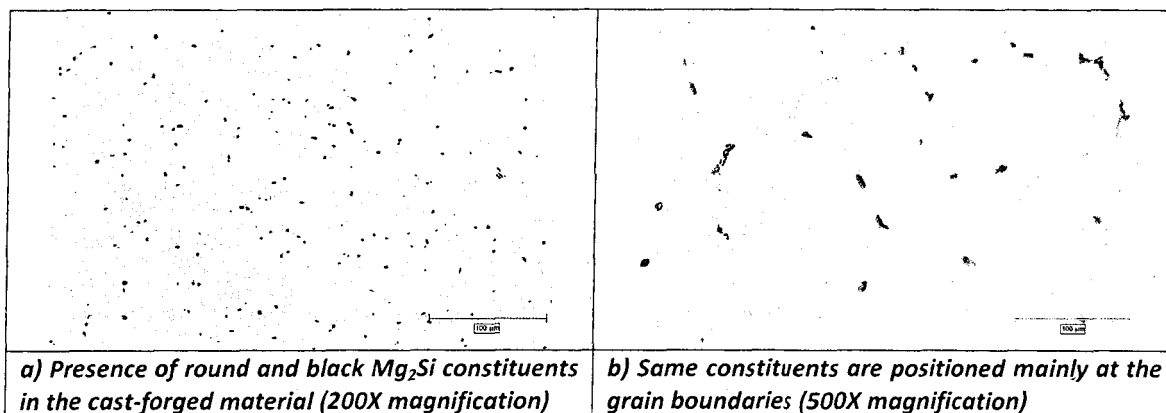
Figure 4.13: Optical micrographs of a cast-homogenized AA6082 aluminum billet that was hot forged

| a) Significant Mg₂Si concentration at surface compared to center zone (100X magnification) | b) Two phases (black and gray colors) dominate others from the surface (500X magnification) |
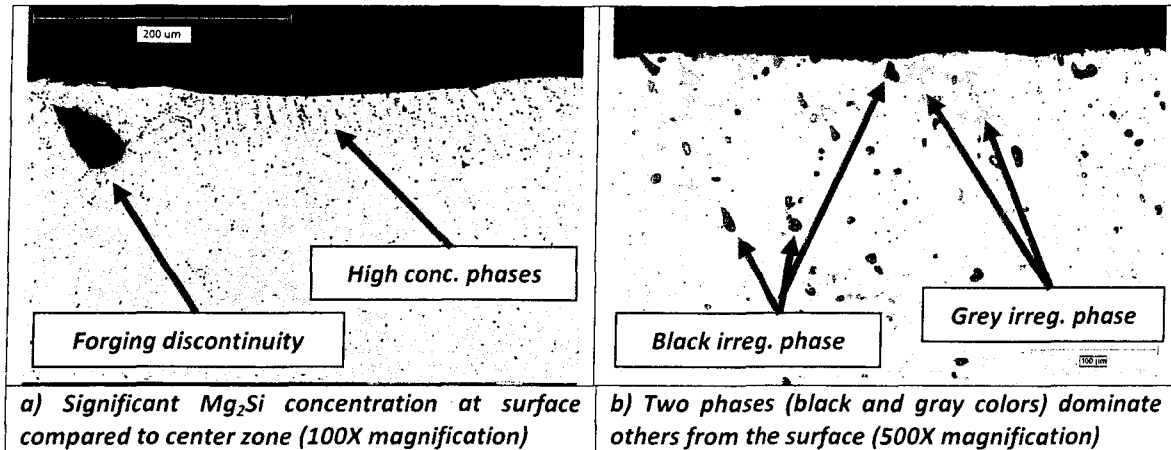
Figure 4.14: Optical surface micrographs of a cast-homogenized AA6082 aluminum billet that was hot forged

Cast-forged material with T6: Solution heat-treated and then artificially aged, the cast-forged material produced finely dispersed precipitates. The elongated grain structure produced by the forging step was changed to recrystallized and fine microstructure with the T6 heat treatment *(Figure 4.15).*
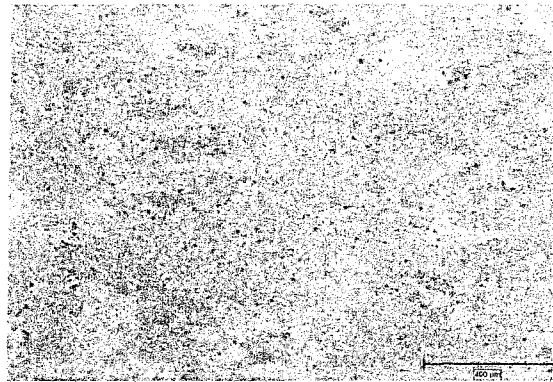
Figure 4.15: Optical polarized macrograph of a cast-homogenized AA6082 aluminum billet that was hot forged with a subsequent T6 HT (Modified Poulton etchant, 50X magnification)

In this case, it was possible to observe the disappearance of coarse Mg_2Si precipitates in the grain boundaries. Finally, precipitates with intermediate sizes were visible in the microstructure *(Figure 4.16)*.

a) Presence of some intermediate sizes of Mg_2Si precipitates in the cast-forged-T6 material (100X magnification)	b) In general, the microstructure shows some precipitates of Mg_2Si in the matrix (500X magnification)
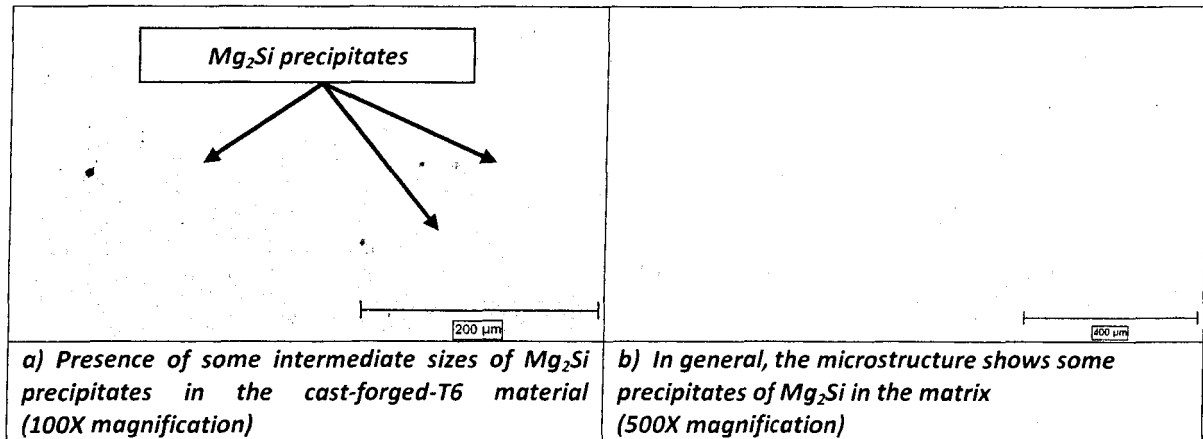
Figure 4.16 Optical micrographs of a cast-homogenized AA6082 aluminum billet that was hot forged with a subsequent –T6 HT

In both cast-forged material cases (with and without T6), significant precipitate concentrations were visible at the surface of the parts **(Figure 4.17)**. Solutionizing and aging heat treatments allowed redistributing the percentage of phase constituents between the surface and center parts.

a) Significant Mg_2Si concentration at surface compared to center zone (100X magnification)	A pale phase dominates others from the surface (500X magnification)
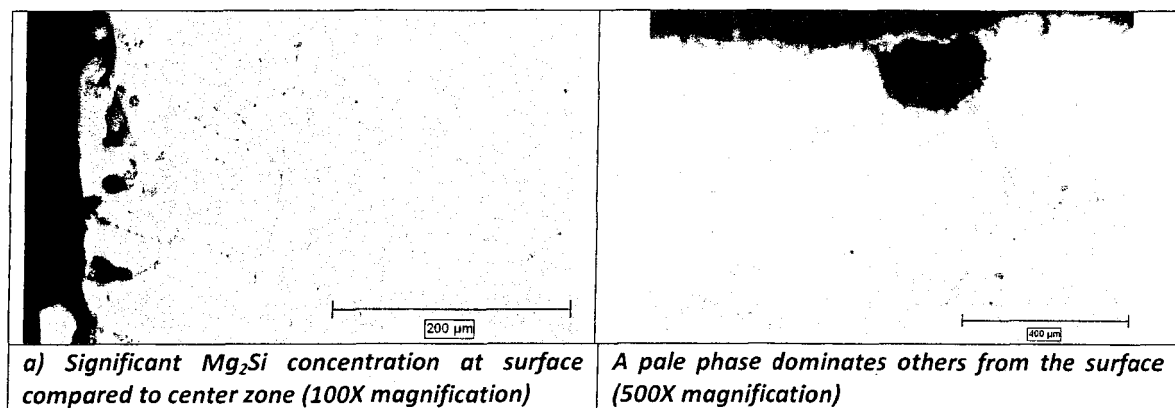
Figure 4.17: Optical surface micrographs of a cast-homogenized AA6082 aluminum billet that was hot forged with a subsequent –T6 HT

Extruded-forged material: The extrusion process has already produced a fibrous macrostructure where the subsequent forging process contributes to amplify this grain flattening tendency *(Figure 4.18)*.
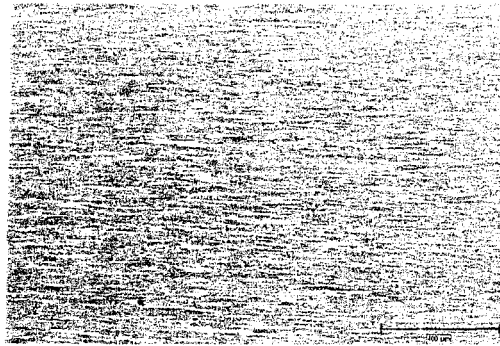
Figure 4.18 Optical polarized macrograph of a homogenized-extruded AA6082 bar that was hot forged (Modified Poulton etchant, 50X magnification)

The Mg_2Si precipitates were finely dispersed in the matrix with the presence of small nodules *(Figure 4.19)*. That is explicit to a microstructure deformed several times with the use of an anisotropic material.

| a) Presence of fine Mg_2Si precipitates in the extruded-forged material (100X magnification) | b) Fine precipitate dispersions of Mg_2Si in the matrix (500X magnification) |
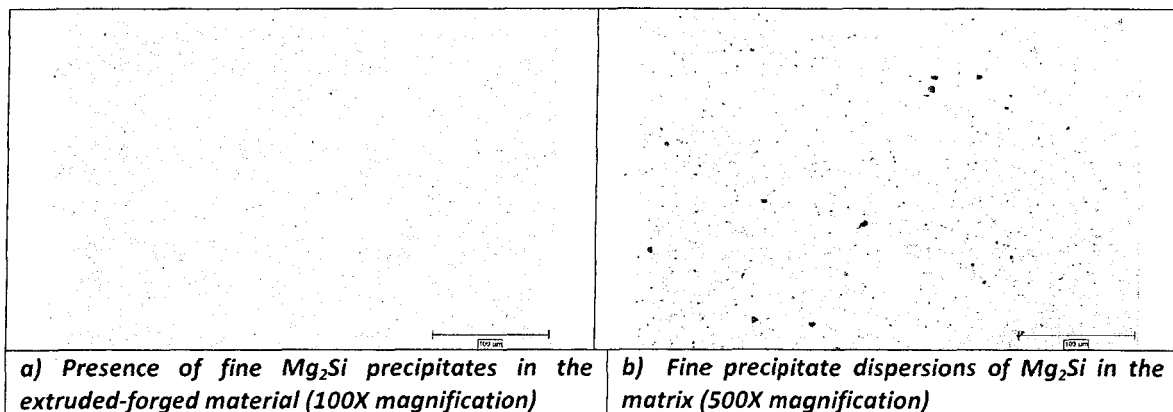
Figure 4.19: Optical micrographs of a homogenized-extruded AA6082 bar that was hot forged

As previously stipulated in the same section, Mg_2Si precipitates at the surface were all finely distributed with a high concentration **(Figure 4.20)**.

a) Presence of several extremely and fine Mg₂Si precipitates at surface for the extruded-forged material (100X magnification)	b) In general, the surface microstructure shows several fine precipitates of Mg₂Si in the matrix (500X magnification)
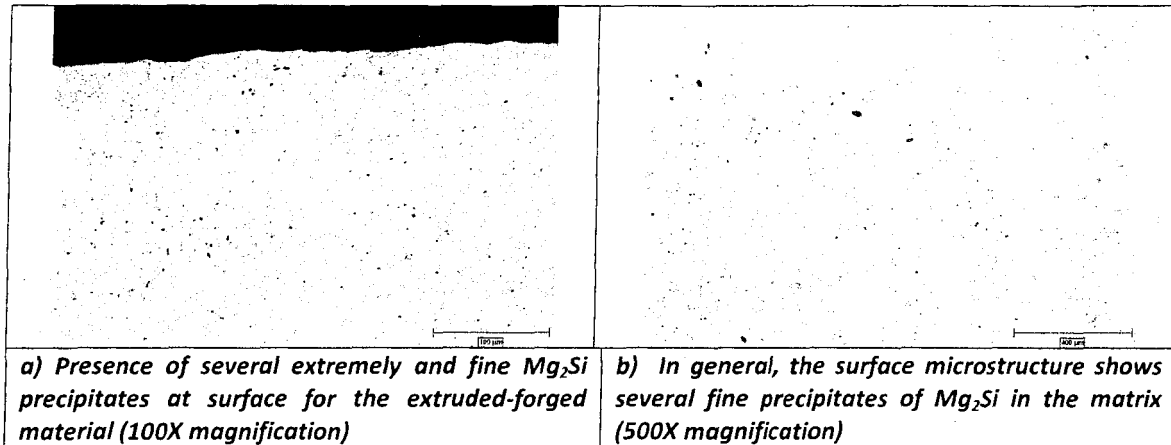
Figure 4.20: Optical surface micrographs of a homogenized-extruded AA6082 aluminum bar that was hot forged

Extruded-forged material with T6: The following heat treatment with T6 temper produced on the extruded-forged material revealed a regenerated microstructure that occurred due to enough stacked internal energy. This former static recrystallization promoted the making of new grains and permitted their growth where the microstructure evolved with large grain dimensions *(Figure 4.21)*.
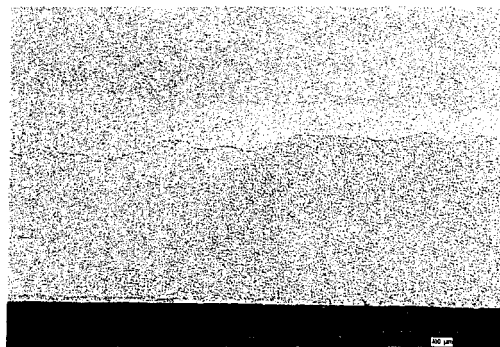
Figure 4.21: Optical polarized macrograph of a homogenized-extruded AA6082 bar that was hot forged with a subsequent –T6 HT (Modified Poulton etchant, 50X magnification)

As seen in the case of cast-forged-T6 material, the Mg_2Si precipitates were all finely distributed in the aluminum matrix with some intermediate size objects **(Figure 4.22)**.

a) Presence of intermediate size Mg₂Si precipitates in the cast-forged-T6 material (100X magnification)	*b) The microstructure shows some Mg₂Si precipitates in the matrix (500X magnification)*
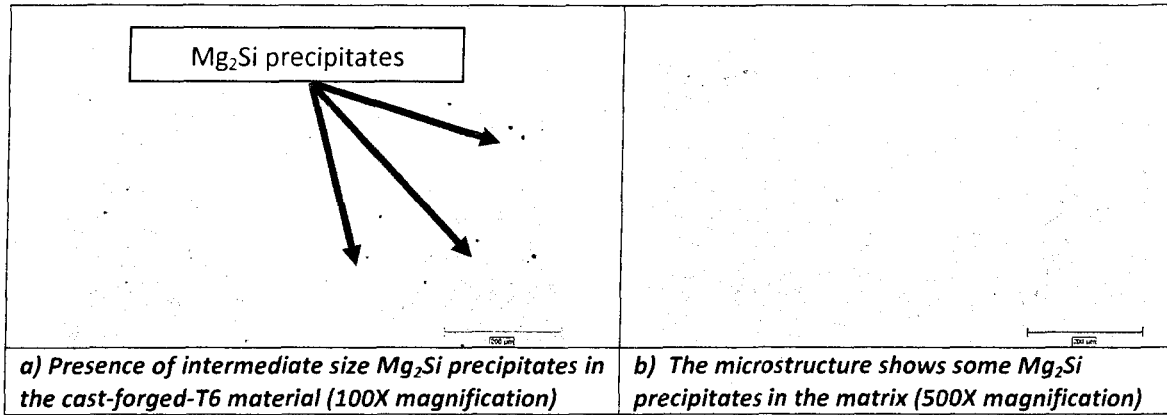
Figure 4.22: Optical micrographs of a homogenized-extruded AA6082 bar that was hot forged with a subsequent –T6 HT

4.3. Electrochemical corrosion tests

The next section details corrosion results of four metallurgical conditions in a corrosion cell using electrochemical methods. Cast-forged and extruded-forged materials with heat treatment effects were tested to determine their corrosion susceptibility.

4.3.1. Cast-forged surface without T6

The open circuit potential started between -0.76 and -0.85 V /SCE for the cast-forged material without T6. The acquisition rate for all OCP curves was fixed at 1 data per 2 seconds. Starting thirty minutes before the testing began, a system for injecting nitrogen bubbles deaerated the solution of its oxygen content with a 10 SCFH flowrate. The potential evolution decrease was involved by the corrosion phenomenon initiation where samples were submerged in a 3.5 w/v% NaCl solution at 21°C. The higher negative voltage obtained for these fives curves was located between -0.85 V and -1.1 V /SCE. After thirty minutes, all OCP curves tended to increase to obtain a stabilized zone at -0.76 V /SCE. This phenomenon is due to the passivation mechanism of aluminum alloys to form a protective aluminum oxide layer, especially in a corrosive solution. In *Figure 4.23*, each curve had its own characteristic slope of between 30 to 1000 minutes to access the passive state. A reciprocal phenomenon between corrosion and passivation can sometimes be produced by a breakdown of the passive layer, as can be seen in one of these five curves at 750 minutes.
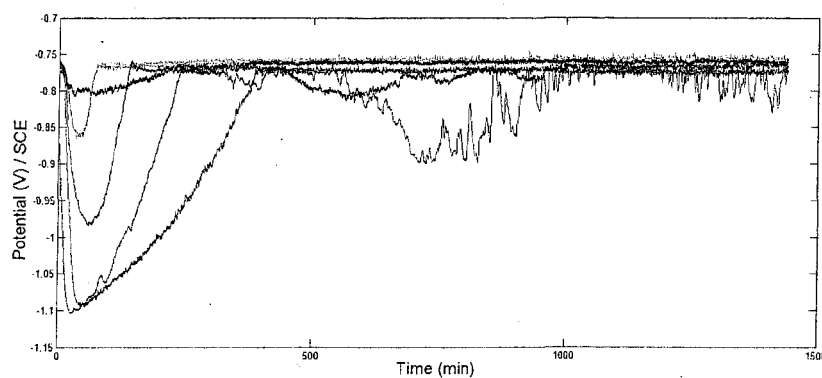
Figure 4.23: Five OCP curves of cast-forged samples in a deaerated 3.5 w/v% NaCl solution during 24 h.

After the OCP acquisitions, samples were polarized by increasing the voltage on the potentiostat machine with a scan rate of 2 mV/s until the maximum current was reached. The apparatus was able to deliver voltage increments until the maximum current output of 1 ampere. This data is equivalent to a current density of 100 mA/cm^2 on the specimen tested in a flat corrosion cell. The presence of regular instabilities in the early stage of polarization is caused by the initial potential that was always manually set below the final value of the OCP test. For example, last OCP measurements of cast-forged samples were identified at -0.76 V/ SCE *(see Figure 4.23)* and the polarization test *(see Figure 4.24)* started to -1V (set under OCP results). Consequently, the anodic polarization of the sample begins at OCP and lower potential instabilities were produced by a cathodic polarization noise.

Polarization voltage began to increase at the last OCP result acquired (near -0.76 V /SCE for the samples). The pitting corrosion potential (E_{pit}) was estimated from 5 polarization curves of each metallurgical condition. The threshold current density value was established arbitrary as j = 0,1 mA/cm^2, where the current quickly increase. It was recognized that for a given potential, pitting corrosion process proceed at given electrode, if determined value was greater than or equal to threshold current density value. For the cast-forged without T6 material condition, at j=0,1 mA/cm^2, the E_{pit} average was determined to -0.63 V /SCE *(Figure 4.24)*.

Some instability on polarization curves were visible starting at -0.65 to -0.5 V /SCE. Theses disturbances were produced during the pitting mechanism, referred to as the breakdown potential, to produce continuous pitting corrosion on samples. The passive alumina film contains or is susceptible to the formation of distribution flaws that are potential sites for pitting. For example, the Mg_2Si and AlFeSi phases that were identified at the grain boundaries of cast-forged microstructures can cause corrosion pitting and instability in these results **(see section 2.2.3, page 33 and section 4.1.2., page 68)**.

Three out of five curves produced this phenomenon of constant pitting lower than the other two. A continuous pitting phenomenon can be identified after the most active pitting zone E_{pit}. These current variations are associated with initiation and repassivation of pits sites prior to the propagation of stable pits.
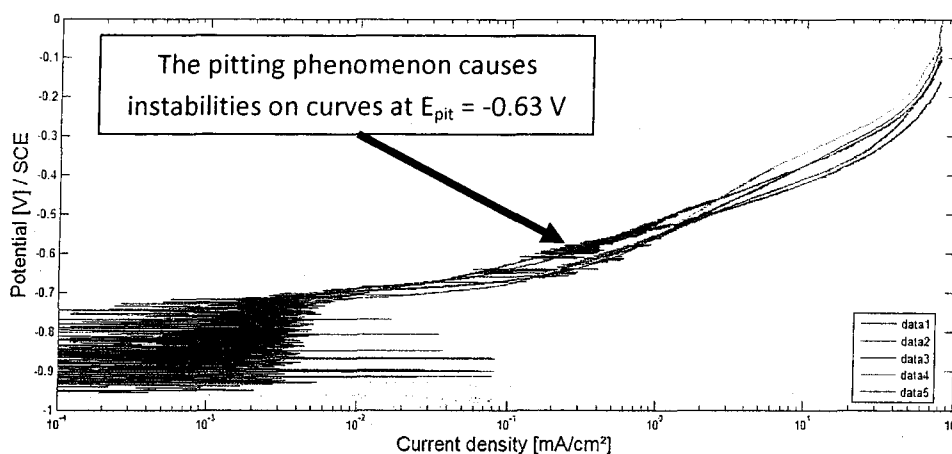
Figure 4.24: Anodic polarization curves of cast-forged samples in a dearated 3.5 w/v% NaCl solution during 24 h. at a 2mV/s scan rate. Instabilities on these curves were produced by a corrosion pitting phenomenon.

<u>Optical and SEM imaging on polarization test specimens</u>

Optical imaging revealed many pits produced at the surface during polarization tests especially for cast-forged without the T6 condition *(Figures 4.25 to 4.27)*. The scanning electron microscope allowed the form evaluation, the dimensions and the depths of the pits as well. Dimensions of the pits were approximately 500 µm by 300 µm.
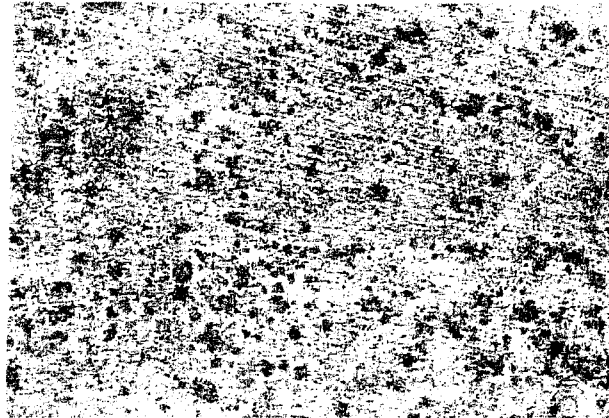
Figure 4.25: Optical macrograph of cast-forged samples after anodic polarization (8X magnification)
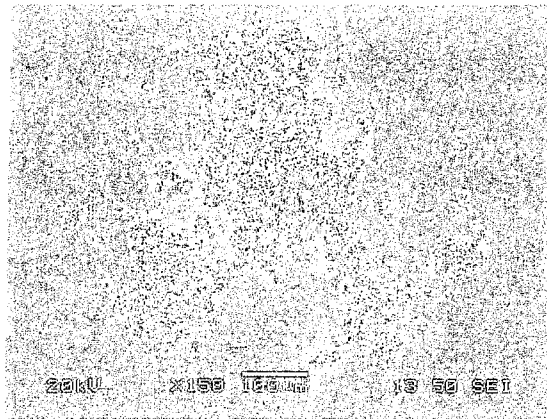
Figure 4.26: SEM micrograph of cast-forged samples after anodic polarization (150X magnification)
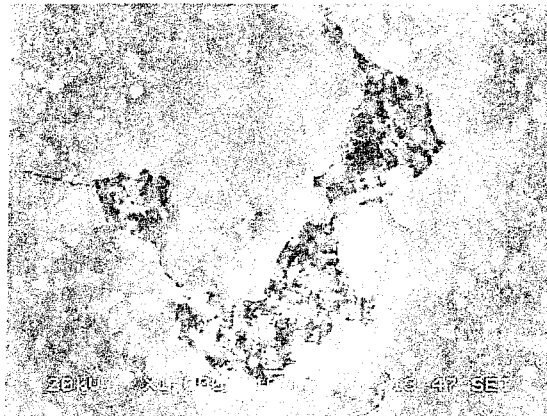
Figure 4.27: SEM micrograph of cast-forged samples after anodic polarization (1000X magnification)

4.3.2. Cast-forged surface with T6

The OCP voltage initiated from -0.85 V /SCE and decreased until a minimum of approximately -1.075 to -1.15 V /SCE was attained for every test. After a specific time for each curve, the voltage was increased to reach a maximum of -0.76 V /SCE, similar to the last condition without T6. After 900 minutes, all tests were stabilized within 0.76 V /SCE ± 0.01 V *(Figure 4.28)*. The cast-forged with the T6 material seems to have the same curve pattern than the cast-forged without the T6. Three similar points were found in theses curves:

1) The voltage drop from the initiating point corresponded to the corrosion initiation on samples during immersion. The voltage became negative and the anodic phenomenon was more active.

2) The curve orientation and the voltage increase are related to the passivation mechanism of aluminum with an aluminum oxide layer at the surface. The corrosion phenomenon was sufficient to produce a protective layer of alumina on the aluminum surface and thus make the potential nobler (more positive).

3) The stabilization of the OCP potential was due to the protective oxide layer formation and this potential was associated with the corrosion potential called « E_{corr} ».
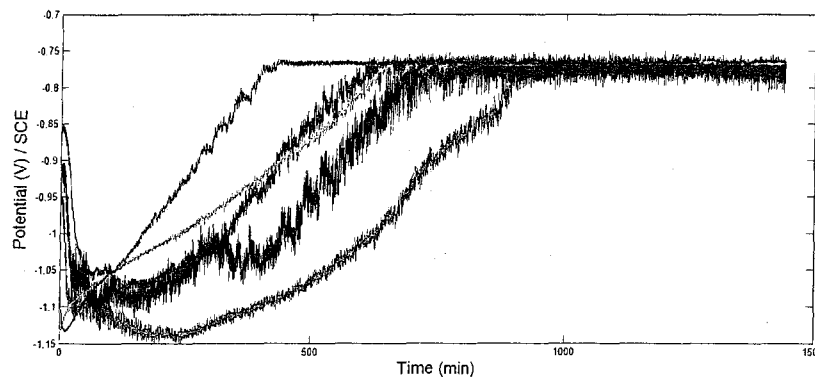
Figure 4.28: Five OCP curves of cast-forged-T6 HT samples in a deaerated 3.5 w/v% NaCl during 24 h.

An anodic polarization action with a scan rate of 2 mV/s was applied after 24 h. of OCP acquisition. The polarization voltage increased at the last E_{corr} result acquired (close to -0.76 V /SCE during the OCP test) until a maximum of 0.1 V was reached. Little instability produced by continuous pitting was visible on one out of the five curves and E_{pit} average was determined at -0.54 V /SCE for this metallurgical condition *(Figure 4.29)*. The other four curves presented no important continuous pitting phenomenon.
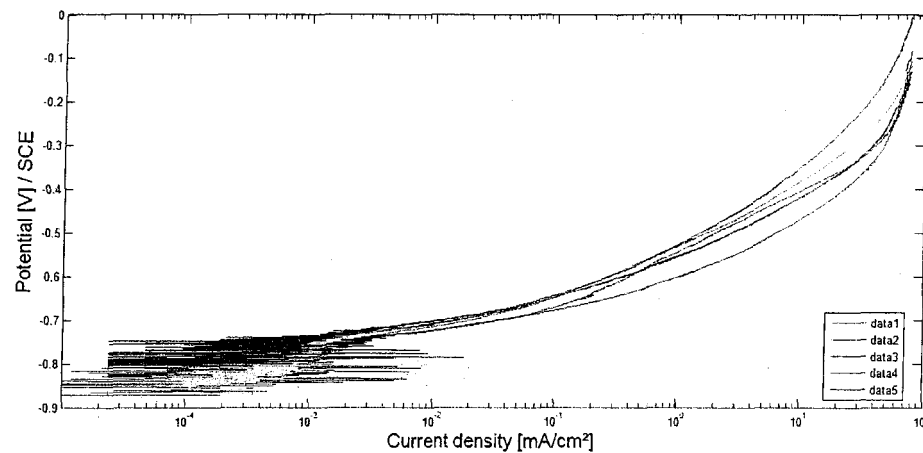
Figure 4.29: Anodic polarization curves of cast-forged -T6 HT samples in a deaerated 3.5% NaCl solution during 24 h at a 2 mV/s scan rate

<u>*Optical and SEM imaging on polarization test specimens*</u>

Anoptical macrograph permitted evaluating the corroded surface of samples and detect the presence of many small and some bigger pits. The SEM revealed pit diameters around 10 to 20 μm. The inside zones of the pits were not observable by SEM making it possible to believe that they are nevertheless deep, i.e., a minimum of a few microns. The optical microscopy analysis was not precise enough to quantify the depth of the pits *(Figures 4.30 to 4.32)*.
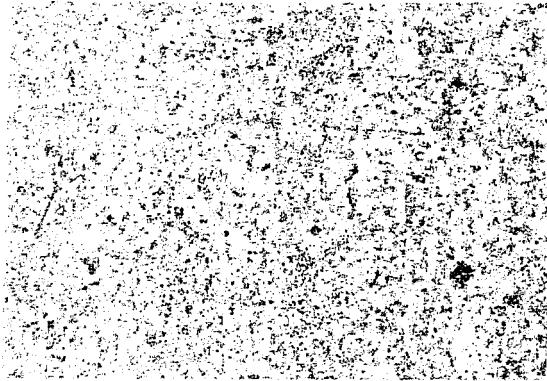
Figure 4.30: Optical macrograph of cast-forged -T6 HT samples after polarization (8X magnification)
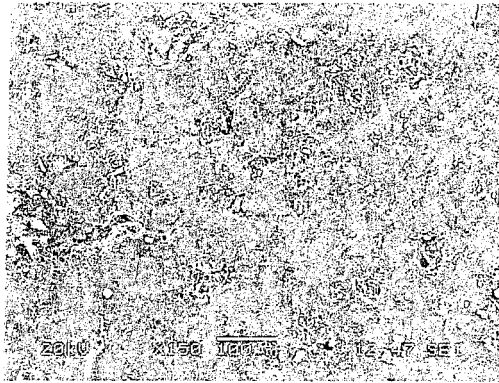
Figure 4.31: SEM micrograph of cast-forged -T6 HT samples after polarization (150X magnification)
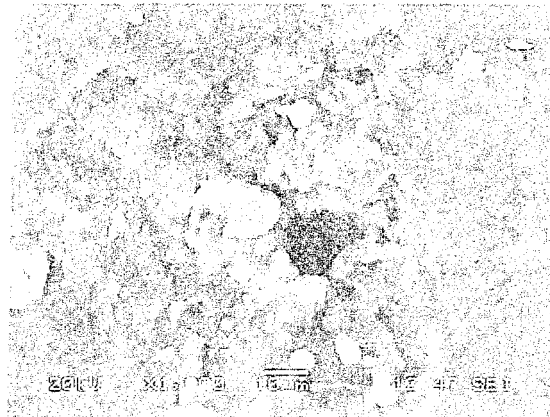
Figure 4.32: SEM micrograph of cast-forged -T6 HT samples after polarization (1000X magnification)

4.3.3. Extruded-forged without T6

Values of open-circuit-potential (OCP) for a forged-extruded condition without T6 were started at -0.76 V /SCE ± 0.01 V and held until the end of 24 hours of acquisition. No important corrosion or passivation mechanisms were apparent during the entire test. Maximal variations during acquisition of all the results were inside an interval of 0.4 V *(Figure 4.33)*. This could be explained by the presence of a protective layer at the surface of this material type. For instance, the peripheral grain layer structure, or the presence of extremely fine dissolved Mg_2Si in the matrix, could play a role on the immunity phenomenon.
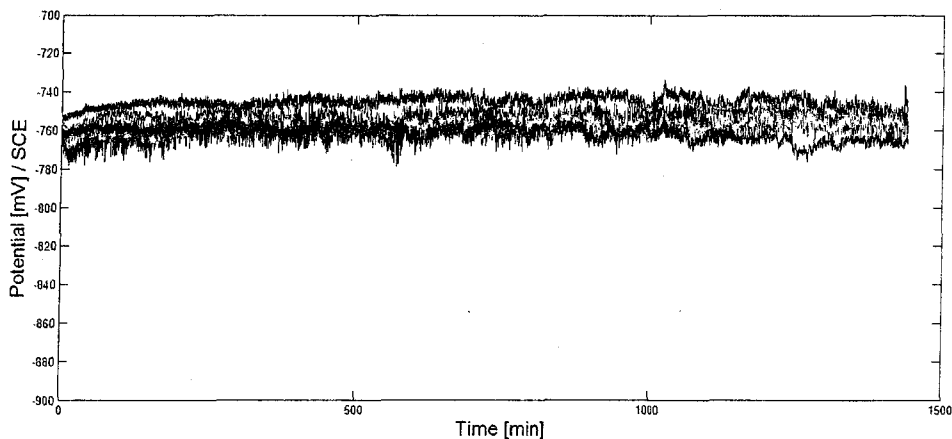
Figure 4.33: Five OCP curves of extruded-forged samples in a deaerated 3.5 w/v% NaCl during 24 h.

At the beginning of each polarization curves, non stable traces are produced by a cathodic polarization noise where the potential was started under the last OCP measurement *(see page 75)*. After this transient zone, E_{pit} was determined for extruded-forged without T6 material at -0.57 V /SCE, where the current sharply increased (at $j > 0.1mA/cm^2$). No continuous pitting was detected on the polarization graph for this metallurgical condition *(Figure 4.34)*.
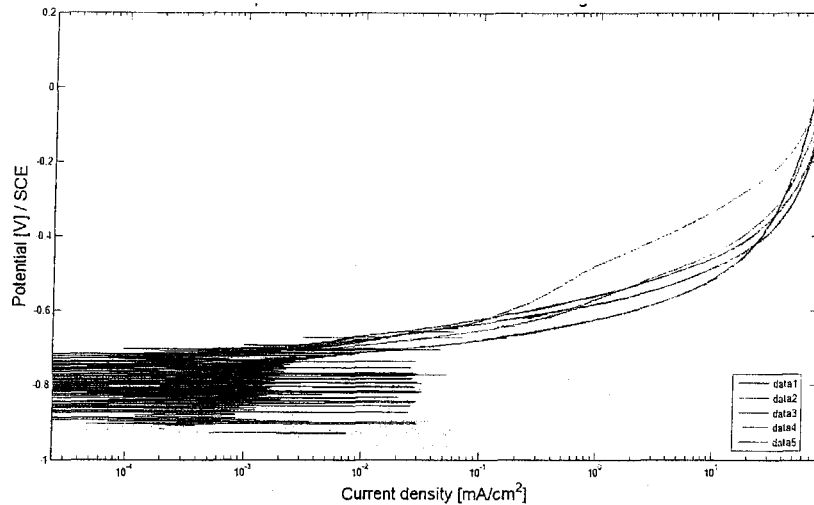
Figure 4.34: Anodic polarization curves of extruded-forged samples in a deaerated 3.5% NaCl solution during 24 h at a 2 mV/s scan rate

Optical and SEM imaging on polarization test specimens

Microscopical observations of corroded samples by electrochemical polarization have permitted to identify a localized corrosion aspect with a lengthened form *(Figure 4.35)*. This asymmetrical form of corrosion seems to follow deformation pattern lines or surface defects produced by the extrusion process. This corrosion presence is not uniform on the surface of samples **(Figures 4.36a and 4.36b)**. Indeed, it is possible to distinguish corrosion spots having significant dimensions ($\approx$ 500 µm) with others that are smaller. With SEM, it was observed that localized pits have low depths **(Figure 4.37)**.
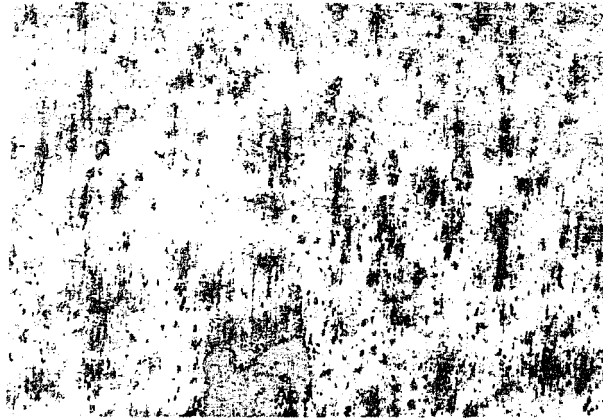
Figure 4.35: Optical macrograph of extruded-forged samples after anodic polarization (8X magnification)

(a)   (b)
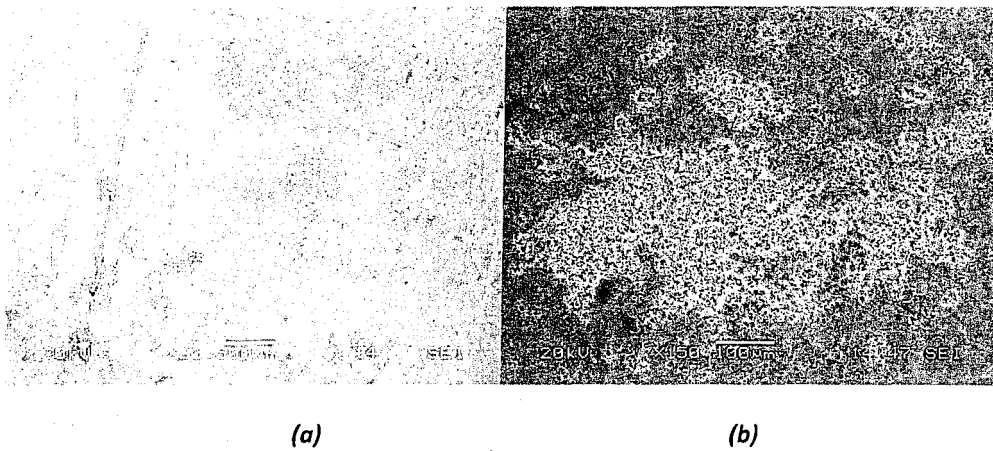
Figure 4.36: SEM micrographs of extruded-forged samples after anodic polarization (a) 30X and (b) 150X
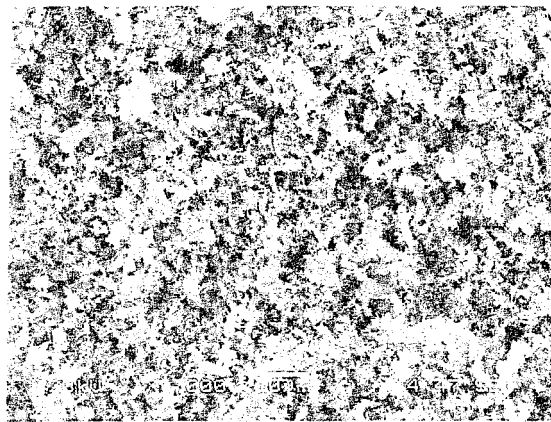
Figure 4.37: SEM micrograph of extruded-forged samples after anodic polarization (1000X magnification)

4.3.4. Extruded-forged with T6

The last condition tested to analyze the evolution of the corrosion phenomenon during 24 hours was the extruded-forged material with T6 heat treatment. Acquisition of five curves made it possible to detect a different tendency than those previously evaluated. The potential start was close to -1.07 V /SCE ± 0.23 and decreased until a maximum of -1.28 V /SCE was reached during the first 30 minutes *(Figure 4.38)*. After this reduction of electrochemical potential, which represents an important phenomenon of corrosion during the specimen immersion time, an increase of potential was carried out to reach equilibrium. In fact, this surface layer stability is explained by the passivation of aluminum where the oxidation phenomenon was too important and created a protective oxide layer. Four out of five curves stabilized E_{corr} at -0.8 V /SCE ± 0.06.

The last curve at **Figure 4.38** did not reach the E_{corr} potential and finished at -1.06 V /SCE. This more negative result is explained by the fact that the test did not have enough time to reach the electrochemical equilibrium after 24 hours of data acquisition. This significant duration obtained (greater than 24 hours) to stabilize E_{corr} of the extruded, forged and heat treated material may be caused by a change in the peripheral coarse grain layer (PGL). Grain size, precipitates or defects in this zone can be modified during the heat treatment step.
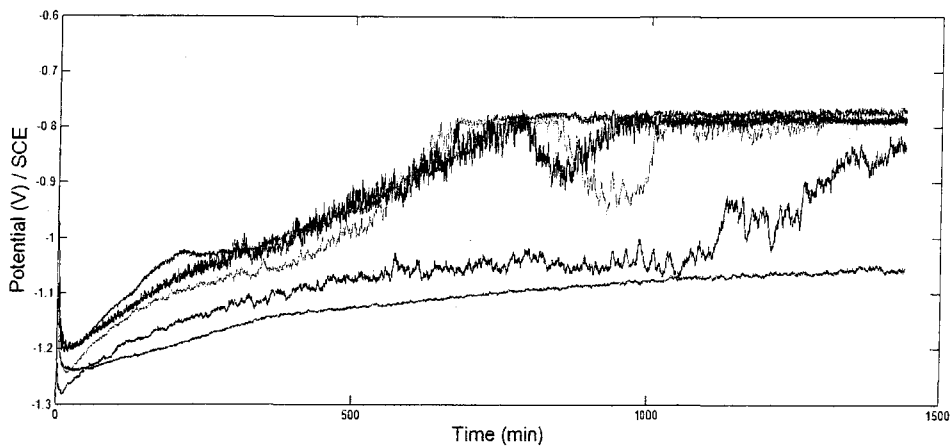
Figure 4.38: Five OCP curves of extruded-forged -T6 HT samples in a deaerated 3.5 w/v% NaCl solution during 24 h

The polarization voltage initiated at the last OCP result (approximately -0.8 V /SCE for samples) was increased to attain E_{pit} for the extruded-forged with T6 material at -0.58 V /SCE where the current quickly increased (j > 0.1 mA/cm^2). No pitting instability was visible on these five curves *(Figure 4.39)*.
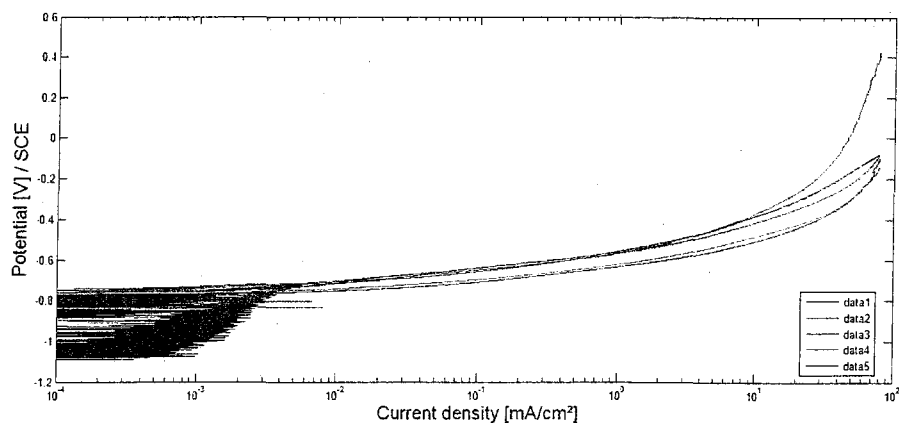
Figure 4.39: Anodic polarization curves of extruded-forged –T6 HT samples in a deaerated 3.5 w/v% NaCl solution during 24 h at a 2 mV/s scan rate

<u>*Optical and SEM imaging on polarization test specimens*</u>

Optical macrographs of anodic polarization for extruded-forged-T6 HT samples revealed a non-uniform aspect of oxidation with large and other smaller spots in the same area **(Figure 4.40)**. The detected large spots have a diameter higher than 500 microns and the corrosion forms resemble metallurgical grains. The SEM micrographs revealed the presence of small localized pits with low depths around the large corroded spots *(Figures 4.41 and 4.42)*.
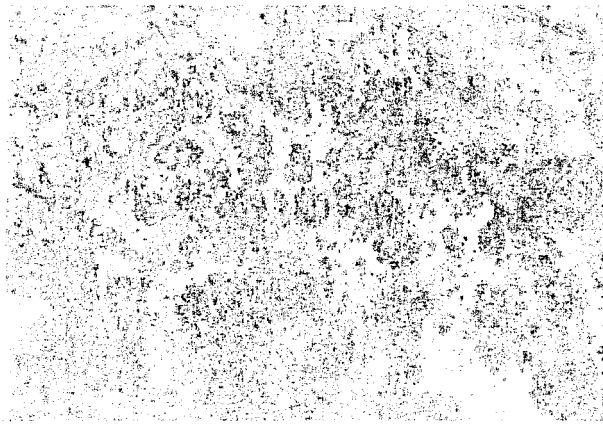
Figure 4.40: Optical macrograph of extruded-forged -T6 HT samples after polarization (8X magnification)
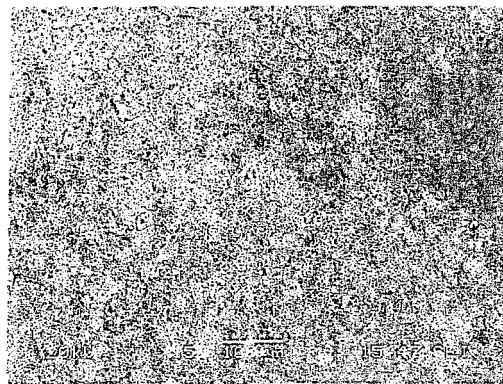
Figure 4.41: SEM micrograph of extruded-forged -T6 HT samples after polarization (250X magnification)
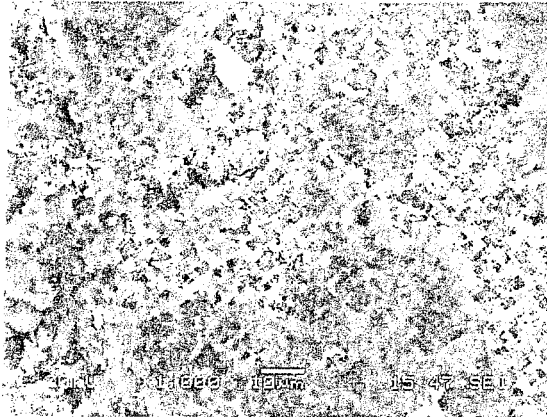
Figure 4.42: SEM micrograph of extruded-forged -T6 HT samples after polarization (1000X magnification)

4.3.5. Comparative evaluation of electrochemical corrosion test results of forged products

Some statements can be drawn from the OCP and polarization corrosion experiments.

i) E_{corr} potentials acquired at the end of the OCP results for the four metallurgical conditions were almost similar between -0.76 V and -0.8 V /SCE. The OCP evolutions were found different for the cast and extruded materials. The cast materials presented a sequence of corrosion-passivation phenomena on the curves. In contrary, extruded materials presented two kinds of sequences: one specific without T6 and one with T6 heat treatment. The extruded-forged materials without T6 had no important potential variations during the OCP test and revealed to be already passivated and not attacked by a sodium chloride solution. After the T6 heat treatment, extruded-forged materials tended to have the same sequence of cast materials, i.e., a corrosion-passivation phenomenon.

ii) A minimum passivation time was established for each metallurgical condition. Due to corrosion, the cast-forged materials without T6 and with T6 necessitated respectively 750 and 900 minutes to be passivated and stabilized. The extruded-forged materials without T6 were already found to be in a passive state.

iii) Anodic polarizations of impressed voltage permitted identifying similar E_{pit} for all conditions between -0.63 to -0.54 V/SCE. Cast feedstock conditions showed a continuous pitting phenomenon after E_{pit}. The cast feedstock T6 condition seemed to have a slightly better pitting resistance when the voltage was applied with the nobler E_{pit} result at -0.54 V/SCE (nobler).

iv) Optical imaging revealed uniform round corroded pit patterns of cast-forged conditions (bigger for non heat treated and smaller for heat treated conditions). Also, extruded materials showed an asymmetrical corrosion aspect with big corrosion spots similar to metallurgical grain forms. Some corrosion spots tended to follow the defects produced by previous deformation processes (extrusion or forging). SEM imagings suggested the high depth of the pits for the cast materials.

4.4. Salt fog corrosion exposure test

The next section illustrates the corrosion results of four metallurgical conditions in a salt fog spray apparatus. Cast-forged and extruded-forged materials with heat treatment effects were tested to determine their corrosion susceptibility.

4.4.1. Cast-forged without T6

Samples for each metallurgical condition tested were in contact with the salt spray fog apparatus during 4 weeks (672 hrs). An additional setup of specimens was removed after two weeks in the corrosive atmospheric environment to analyze the evolution of the corrosion phenomenon at half time. The area percentage of pits on the surface of cast-forged materials without T6 increased from 8.57% to 13.46%, a gain of 4.89% in two weeks *(Table 4.1)*. The pits count number evolved from 259 to 390 after 4 weeks of testing. The pit dimensions were found similar for both duration times with 185 μm long by 118 μm wide. Metallographical sectioning and polishing of the perpendicular surfaces permitted to evaluate a pit depth of 161.18 μm at the end.

Table 4.1: Image analysis results of AA6082 cast-forged material during four weeks of salt fog cabinet exposure in a 3.5 w/v% NaCl solution at 2°C

Time Duration	Data	Number of fields Analyzed	Area Percentage of Pits (%)	Pit Counts	Aspect Ratios	Pit Areas (μm^2)	Pit Lengths (μm)	Pit Widths (μm)	Pit Depths (μm)
2 weeks	Mean	29	8,57	259	1,5	24612,5	184,3	118	
	Std Dev		4,38	145	0,335	98421,3	208,9	118,2	
4 weeks	Mean	30	13,46	390	1,51	25695	185,5	118	161,18
	Std Dev		6,02	159	0,337	103141,5	231	135	111,39

<u>*Optical imaging on salt spray corroded specimen surfaces*</u>

Salt spray corrosion macrographs *(Figures 4.43a and 4.43b)* of cast-forged samples exposed important

pitting phenomena on their surfaces for both duration times (two and four weeks).

| (a) Two weeks duration time | (b) Four weeks duration time |
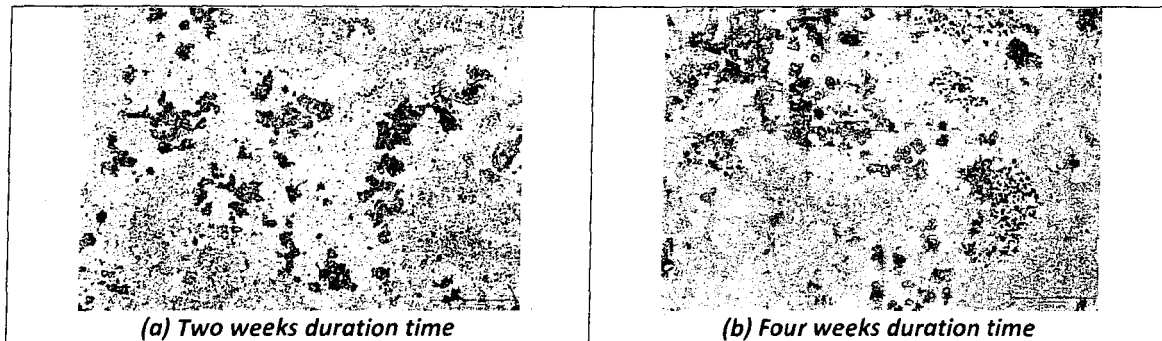
Figure 4.43: Optical macrographs of salt spray corroded specimens for the cast-forged condition (8X

magnification)

<u>*SEM imaging on salt spray corroded specimen surfaces*</u>

Microanalysis of localized corrosion by SEM allowed identification of many micro-pits inside large pits.

Theses micro-holed sites at the base of large pits seem to play a role in the initiation and propagation

mechanism of corrosion in the AA6082 cast-forged with T6 aluminum alloy *(Figure 4.44)*.

| (a) Four weeks duration at 150X | (b) Four weeks duration at 500X magnification |
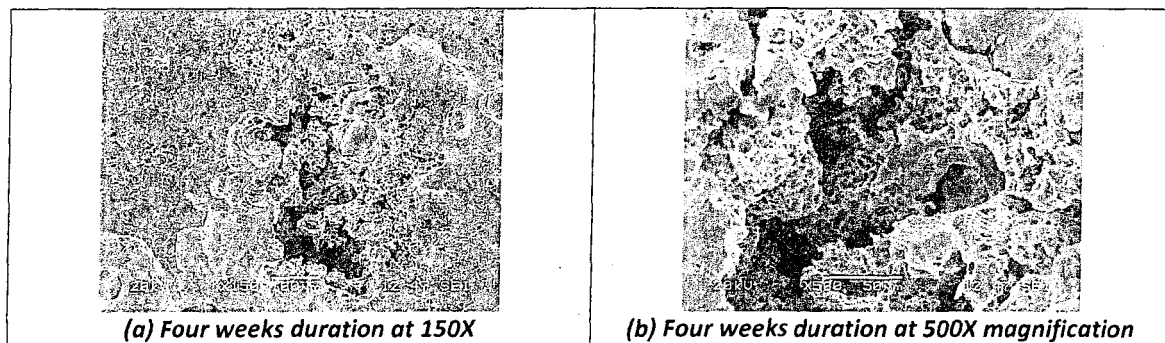
Figure 4.44: SEM micrographs of salt spray corroded specimens for the cast-forged condition

4.4.2. Cast-forged with T6

Evaluated by an image analyzer, this condition demonstrated an area percentage increase from 1.56% to 3.62% *(Table 4.2)*. The aspect ratio parameter revealed a difference of 0.08 between the two and four weeks time duration showing elongated pits. The pit dimensions changed from 80.5 x 49.6 after two weeks to 140 x 91.2 microns at the end of the test. Profile of the corroded surface gives a pit mean depth of 37.27 μm after four weeks.

Table 4.2: Image analyses results of AA6082 cast-forged –T6 HT material during four weeks of salt fog cabinet exposure in a 3.5 w/v% NaCl solution at 21°C

Time Duration	Data	Number of Fields Analyzed	Area Percentage of pits (%)	Pit Counts	Aspect Ratios	Pit Areas (μm²)	Pit Length (μm)	Pit Widths (μm)	Pit Depths (μm)
2 weeks	Mean	38	1,56	489	1,56	3778,6	80,5	49,6	
	Std Dev		0,378	135	0,378	11641,5	100,5	58,1	
4 weeks	Mean	30	3,62	227	1,48	11869	140	91,2	37,27
	Std Dev		2,19	104	0,333	29499,3	120,9	67,4	15,80

Optical imaging on salt spray corroded specimen surfaces

Optical corroded figures showed the presence of some small and round pits *(Figure 4.45)*. At higher magnifications, it was possible to have a better resolution on a group of micropits less than 10 μm. Also, some large darkened spots, corresponding to a low corrosion surface phenomenon, were distinguished.

(a) Four weeks duration at 8X magnification | (b) Four weeks duration at 20X magnification
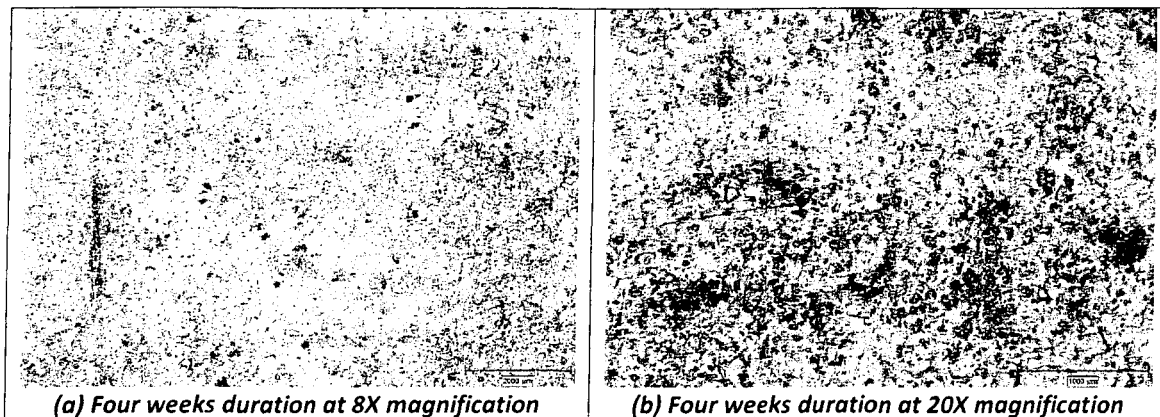
Figure 4.45: Optical macrographs of salt spray corroded specimens for the cast-forged –T6 HT condition

<u>*SEM imaging on salt spray corroded specimen surfaces*</u>

Using the SEM microscope permitted to discover two corrosion aspects on corroded samples of cast-forged with T6 material: the presence of small pits with different forms, and some grain boundary attacks *(Figures 4.46a and 4.46b)*.

(a) Four weeks duration at 150X | (b) Four weeks duration at 500X magnification
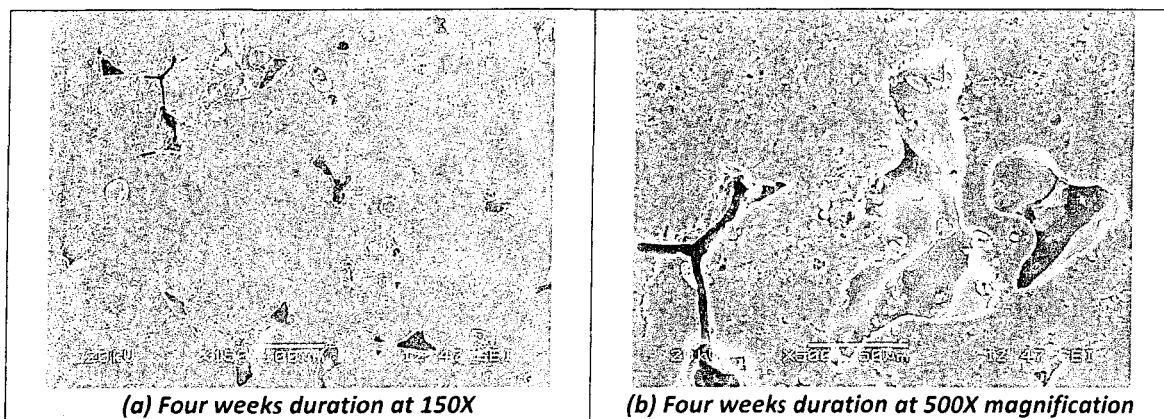
Figure 4.46: SEM micrographs of salt spray corroded specimens for the cast-forged -T6 HT condition

4.4.3. Extruded-forged without T6

The corroded material from the extrusion process was tested with the same parameters by an image analysis software *(Table 4.3)*. As presented in the preceding sections, area percentages attained 4,62% against 6,77% after 4 weeks for the extruded-forged stock without the T6 condition. The aspect ratios were nearly the same for both times and pit dimensions increased in function of time. Metallographically cut profiles gave a pit mean depth of 180,31 μm.

Table 4.3: Image analyses results of AA6082 extruded-forged material during four weeks of salt fog cabinet exposure in a 3.5 w/v% NaCl solution at 21° C

Duration	Data	Number of Fields Analyzed	Area Percentage of Pits (%)	Pit Counts	Aspect Ratios	Pit Area (μm^2)	Pit Lengths (μm)	Pit Widths (μm)	Pit Depths (μm)
2 weeks	Mean	47	4,62	235	1,51	13705,8	158	101,2	
	Std Dev		3,6	170	0,358	21106,8	130,3	71,2	
4 weeks	Mean	29	6,77	215	1,5	23471,1	187,2	120,5	180,31
	Std Dev		3,48	70,5	0,323	84093,9	192,2	112,2	72,96

Optical imaging on salt spray corroded specimen surfaces

Macro observations on the extruded material after two weeks in the corrosive media showed a localized pitting aspect where the pits seemed to be gathered together at the same place. Small pits seem to be located close to large white corroded spots. After 4 weeks of test duration, the pit dimensions have increased to form very important pit areas in the same place *(Figure 4.47)*.

(a) Two weeks duration at 8X magnification | (b) Four weeks duration at 8X magnification
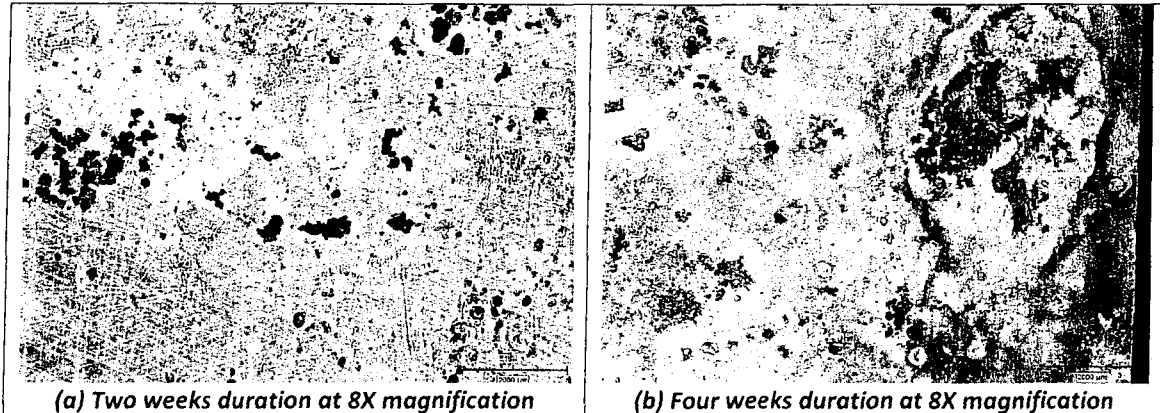
Figure 4.47: Typical macrographs of salt spray corroded specimens for the extruded-forged condition

SEM imaging on salt spray corroded specimen surfaces

Micro-observations with the SEM technique permitted to appreciate the morphology, dimensions and depths of the pits after 4 weeks in a corrosive environment. Cavities tended to obtain an elongated pattern during the corrosion phenomenon and pit depths had the highest result with 180,31 µm *(Figure 4.48)*. It was impossible to inspect the bottom of the pits as it was too dark, even with a maximum of brightness.

(a) Four weeks duration at 150X | (b)Four4 weeks duration at 500X magnification
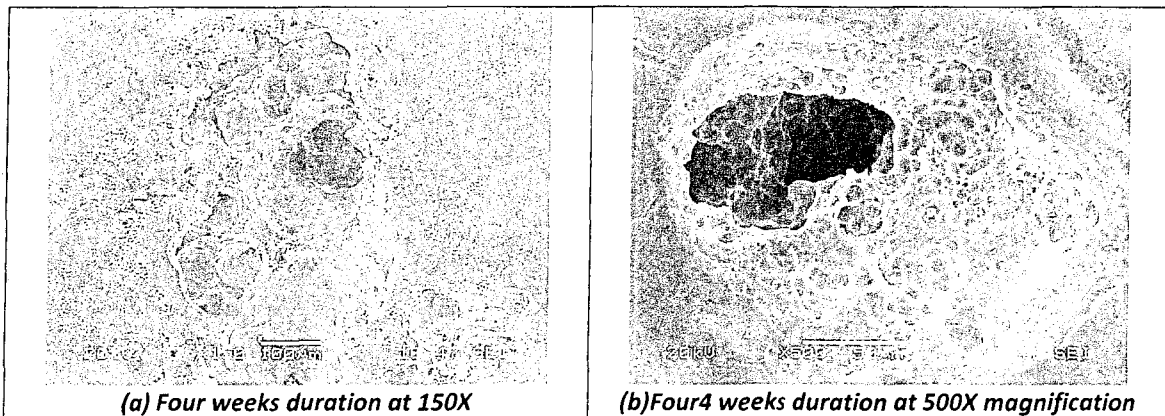
Figure 4.48: SEM micrographs of salt spray corroded specimens for the extruded-forged condition

4.4.4. Extruded-forged with T6

The last condition practiced with the salt spray corrosion apparatus revealed a pit area percentage of 3.6% compared to 3.68% after 4 weeks of test routine *(Table 4.4)*. The aspect ratio was nearly the same for both duration time periods and the pit dimensions increased two more times. Finally, the metallographical preparation of the corroded samples permitted to measure a pit depth of 40.91 µm.

Table 4.4: Image analyses results of AA6082 extruded-forged –T6 HT material during four weeks of salt fog cabinet exposure in a 3.5 w/v% NaCl solution at 21°C

Duration	Data	Number of Fields Analyzed	Area Percentage of pits (%)	Pit Counts	Aspect Ratios	Pit Areas (μm^2)	Pit Lengths (μm)	Pit Widths (μm)	Pit Depths (μm)
2 weeks	Mean	21	3,6	556	1,55	4403	86,3	52,2	
	Std Dev		2,57	423	0,648	11671,9	115,3	49,6	
4 weeks	Mean	32	3,68	134	1,54	204401,3	177,2	110,3	40,91
	Std Dev		4,08	137	0,377	70455	186,8	105,2	22,09

Optical imaging on salt spray corroded specimen surfaces

Optical macrograph analyses on extruded-forged stock with T6 condition showed the presence of non uniform pits *(Figure 4.49)*. There was an important dissimilarity for the maximum pit area parameters where they increased from 4 403 after two weeks to 204 401 μm^2 after 4 weeks of corrosion testing. This can be demonstrated by next Figures 4.49 a) and b) of corroded samples where there were large corroded zones with multiple pits.

(a) Two weeks duration at 8X magnification | (b) Four weeks duration at 8X magnification
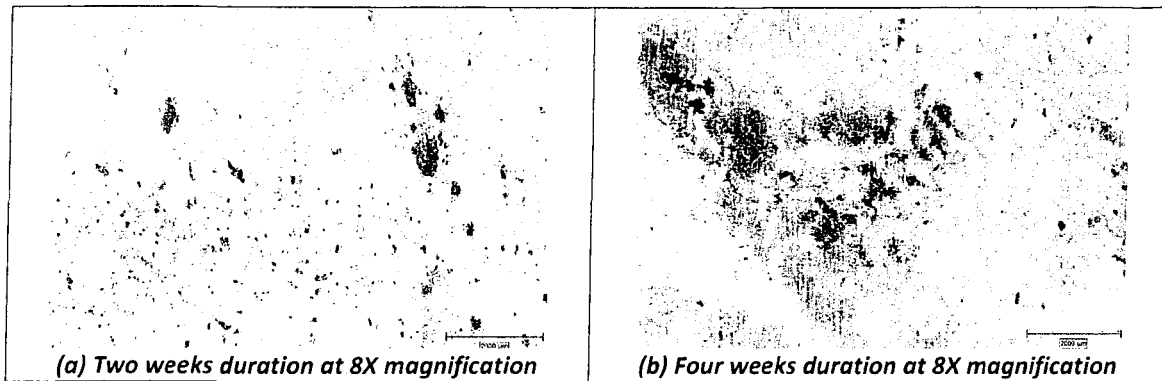
Figure 4.49: Typical macrographs of salt spray corroded specimens for the extruded-forged -T6 HT condition

SEM imaging on salt spray corroded specimen surfaces

Surface observations of large corroded zones by the SEM method exposed multiple pits in the same zone with elongated orientations (Figure 4.50). At a higher magnification, it was possible to identify another type of corrosion with branch forms around the deep elongated pits. That could be the initiation of the corrosion phase for these deep and elongated pits in the large zones.

(a) Four weeks duration at 150X | (b) Four weeks duration at 500X magnification
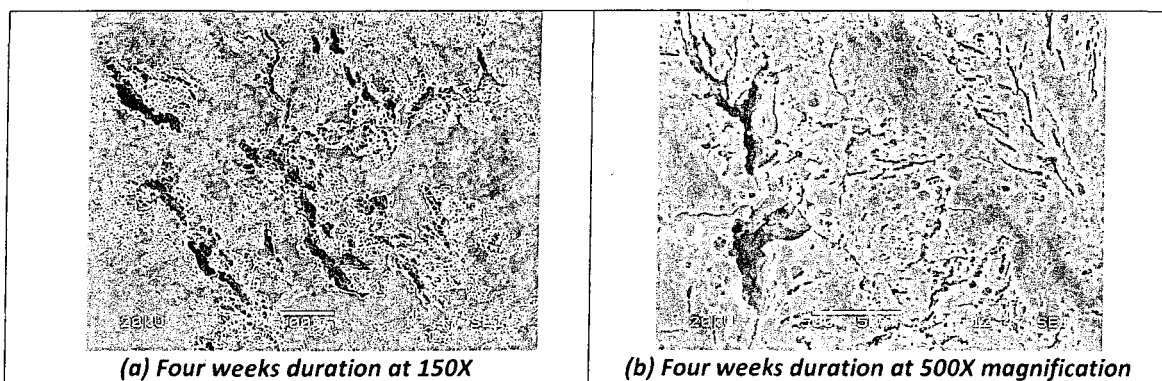
Figure 4.50: SEM micrographs of salt spray corroded specimens for the extruded-forged –T6 HT condition

4.4.5. Comparative evaluation of salt spray corrosion test results of forged products

The following statements can be given for the salt spray corrosion results of forging stocks.

i) In general, the relative area percentage of pits for conditions without T6 had higher results than after this treatment *(Figure 4.51)*. Without T6, the cast-forged condition presented a pit area twice as more significant than the extruded-forged materials (13.45 % vs 6.77 %). With T6, both conditions with forging (cast and extruded) revealed similar corrosion pit areas (3.62 % vs 3.68 %) after 4 weeks. An interesting fact concerning these metallurgical conditions is that the two to four weeks pit evolution was continuously on the cast-forged materials (1.56% to 3.62%) against a stagnant percentage for the extruded-forged materials (3.6% to 3.68%). A passivation or exfoliation mechanism by the Peripheral Grain Layer could explain these results on the extruded-forged materials.
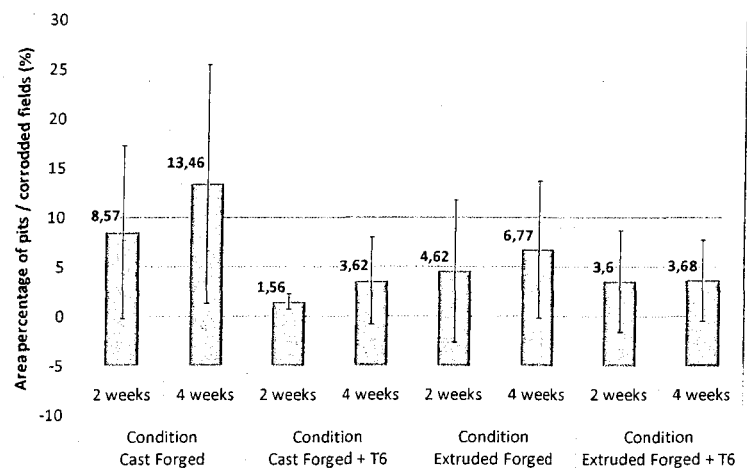
Figure 4.51: Relative area percentage of corrosion pits (%) per corroded field analyzed for different metallurgical conditions during salt fog spray testing

ii) The number of pits detected *(Figure 4.52)* and their total specific area *(Figure 4.53)* represent detailed and useful information. These bar charts explain the inverse proportional relation between the number of pits with specific surface areas for both types of materials. For example, the extruded-forged-T6 condition has the minimum pit count (134 pits) with the higher corroded surface area of 0.07 mm^2. This fact can be justified by the corrosion of specific grain located in the PGL zone. Some metallurgical grains with high dimensions seem more susceptible to corrosion after static recrystallization produced by the final heat treatment. Other interesting fact after 4 weeks of testing, the corrosion pits density of heat treated materials decreased **(see Figure 4.52)** but theirs dimensions increased **(see Figure 4.53, 4.54 and 4.55)**. This could be explained by the agglomeration of pits together.
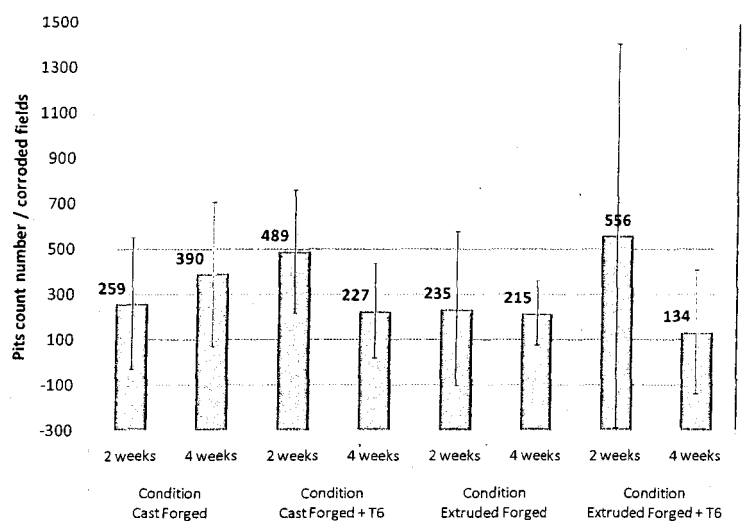
Figure 4.52: Pit count number per field analyzed for different metallurgical conditions
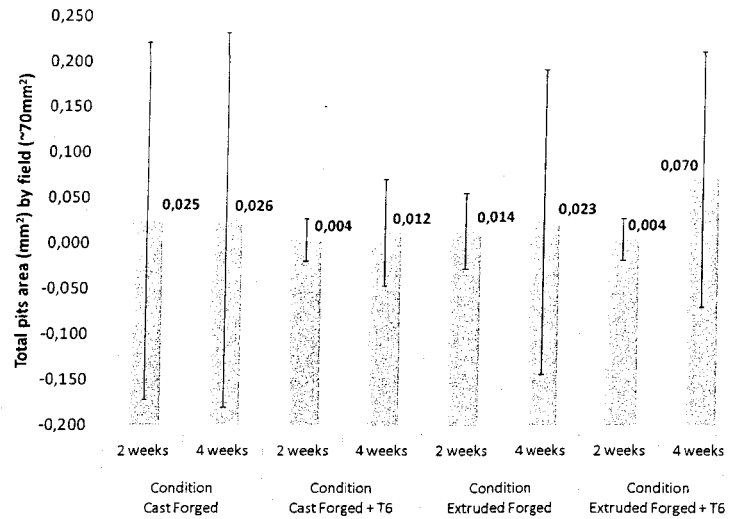
Figure 4.53: Field area of corrosion pits (μm) per field analyzed for different metallurgical conditions

iii) A 2D dimensional image analysis of pits on corroded surfaces has indicated that the length *(Figure 4.54)* and width *(Figure 4.55)* parameters seem to be similar for both materials without a –T6 treatment after four weeks of corrosion testing (cast-forged: 185.5 x 118 μm against extruded-forged: 187.2 x 120.5 μm). On the other hand, the T6 cases show larger pit dimensions for the extruded-forged material (177.2 x 110.3 μm) compared to its cast-forged opponent (140 x 91 μm)..
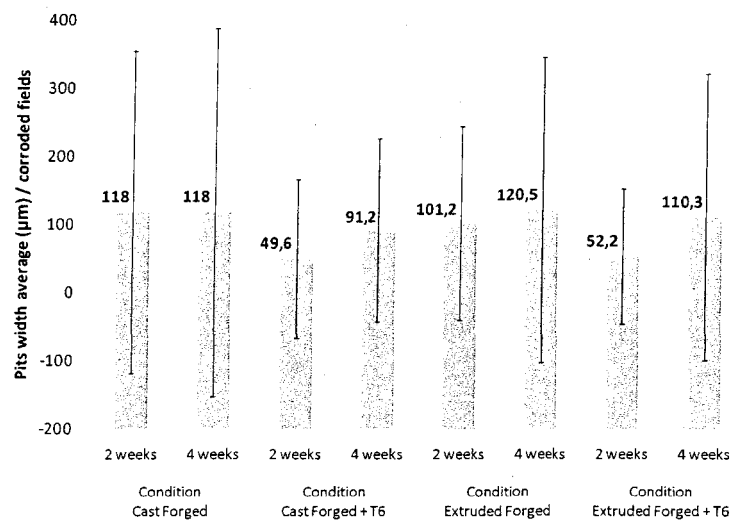
Figure 4.54: Pit width averages (μm) for different metallurgical conditions tested during four weeks
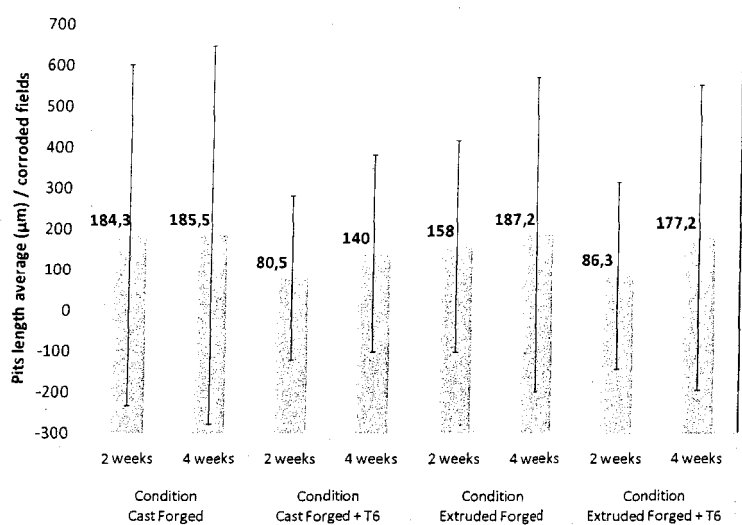
Figure 4.55: Pit length averages (μm) for different metallurgical conditions tested during four weeks

iv) Pit depth profile analyses for both conditions after four weeks permitted to show minor differences between cast and extruded materials before and after T6 heat treatments *(Figure 4.56)*. Depths measured for extruded-forged materials were higher than their cast material opponents in both cases.
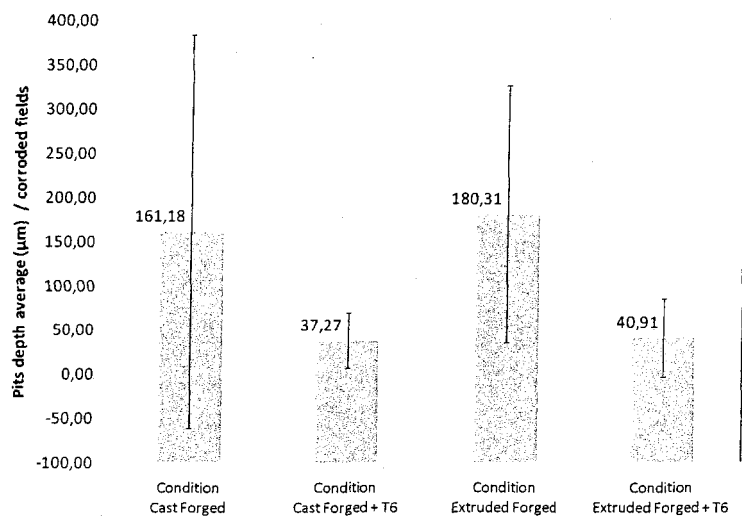
Figure 4.56: Individual pit depths for different metallurgical conditions after 4 weeks of salt spray testing

v) Sectional profiles of pit analyses revealed specific corrosion forms for each cast and extruded-forged materials. As can be seen on **Figures 4.57a and 4.57b**, the cast-forged material presents a round aspect and the deformed extruded stock displays a horizontal pattern for corrosion pits. This specific pattern for the second material could be explained by a corrosion exfoliation mechanism under the PGL layer of the extruded residual structure.

| (a) Cast-forged-T6 pit forms | (b) Extruded-forged-T6 pit forms |
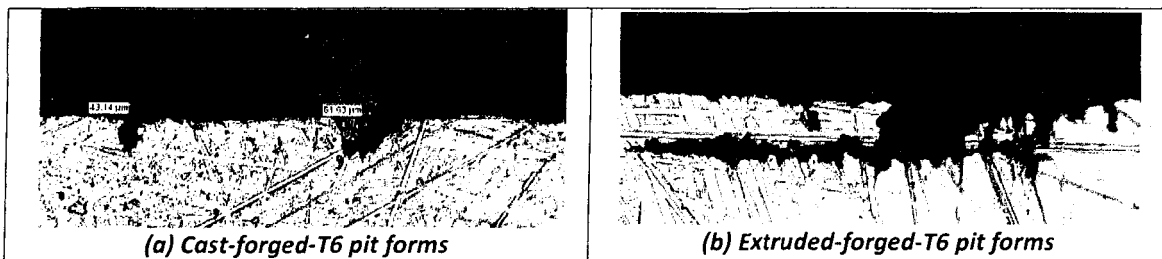
Figure 4.57: Typical profile of corroded sections with pit depths and forms after four weeks of duration periods (100 X magnification)

4.5. Reverse bending corrosion-fatigue test

The last two sections of results have discussed traditional corrosion tests (electrochemical polarization and salt fog spray chamber) that exposed the corrosion susceptibility of different materials with different metallurgical conditions. These tests were always carried out in a mechanical unconstrained medium, while aluminum parts were often subjected to important stress corrosion crackings due to their specific properties. For this reason, there was a third test to evaluate the impact of mechanical cyclic stresses combined to the same sodium chloride corrosive environment. The following paragraphs show fatigue results for both cast and extruded-forged materials in different environments (air and sodium chloride solution).

4.5.1. Fatigue trials in air environment

As explained in the experimental section, 3.2.3, page 57, many specimens were tested with similar stress magnitudes (between 50 to 150 MPa) to obtain a good repeatability of results. The bench setup allows for four samples at the same time during the cyclic cantilever test. *Figure 4.58* shows the raw data acquired from fatigue tests in the air medium. Only the forged T6 heat treatment condition materials were tried as this is the final metallurgical state in its industrial application.
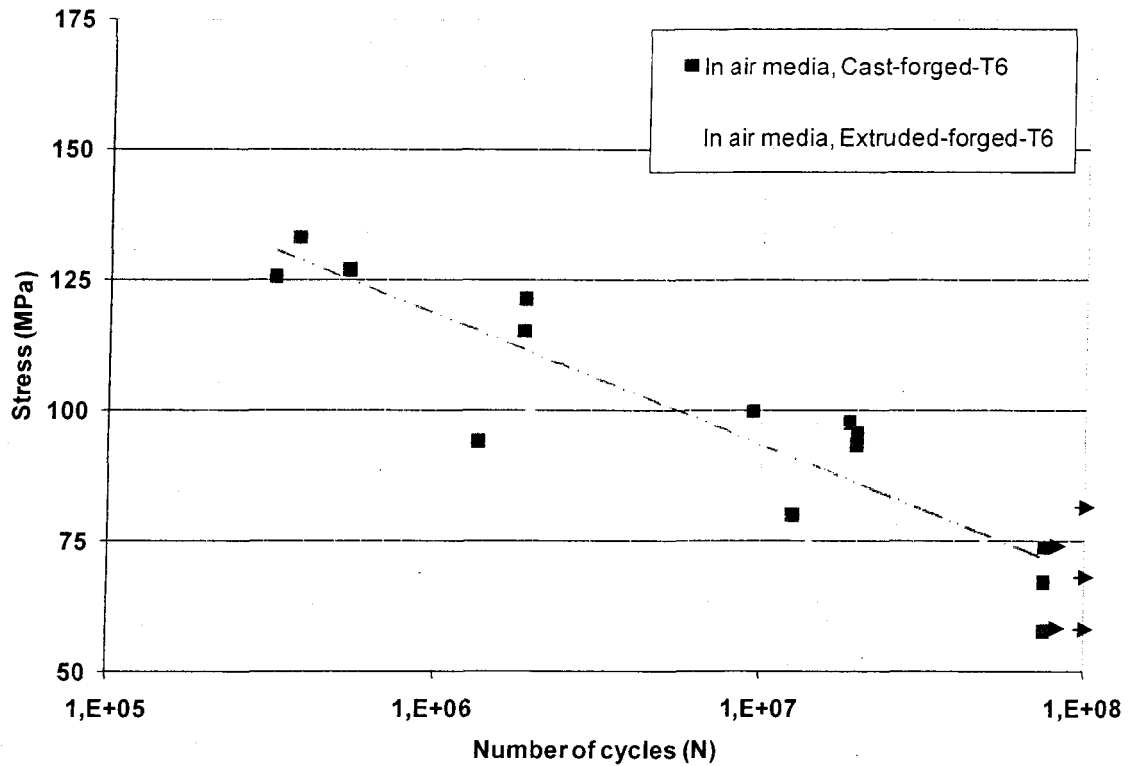
Figure 4.58: Reverse bending fatigue stress-life in air medium of both forged –T6 HT materials

This graph demonstrated different cases when low stresses and high stresses were applied on forged materials. First, low fatigue stresses located between 60 and 100 MPa, allowed the cast-forged-T6 conditions to obtain higher fatigue endurances. A difference of approximately 8 million cycles was attained for a specific test when compared with similar extruded-forged specimens. The case where high stress magnitudes were applied (≥ 100 MPa) gives life endurance results twice as high for the extruded-forged materials.

4.5.2. Fatigue trials in a 3.5 w/v% NaCl solution

The same materials and conditions were used in a 3.5 w/v% sodium chloride solution. An addition of corrosive salts can modify or accelerate the initiation and propagation fatigue mechanisms compared to the air media. **Figure 4.59** displays reverse bending fatigue results with corrosion effects on stress-life endurance.

Figure 4.59: Reverse bending fatigue stress-life in a corrosive medium of both forged –T6 HT materials
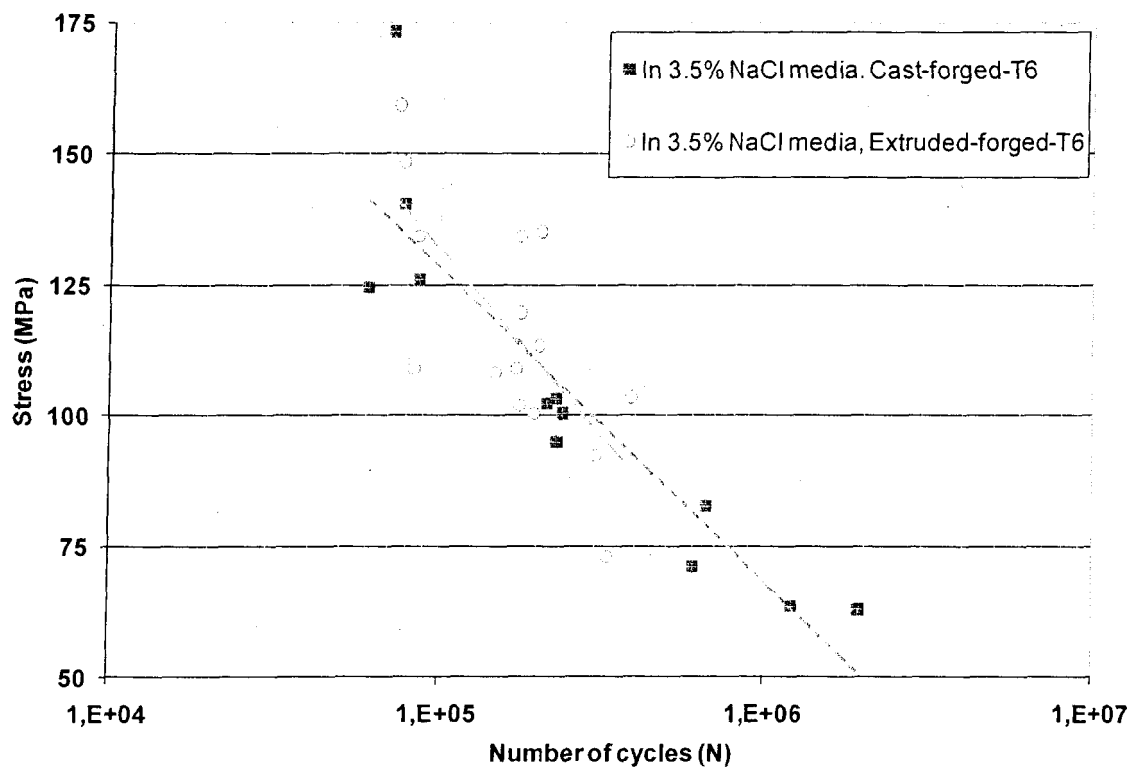
A general observation was established for these fatigue results with a corrosive effect. The number of cycles in an air environment was approximately 1×10^3 higher than in a 3.5 w/v% NaCl environment. Similar results were obtained for low and high stresses applied. At high stress levels, the performance of extruded-forged material seemed greater with an upper fatigue life limit. The best example to examine this fact was obtained at 135 MPa where fatigue specimens from extruded materials resisted a minimum of two life durations to the cast materials' one life duration. Otherwise, the cast-forged materials were found to be better when low stresses under 100 MPa were applied.

4.5.3. Fatigue fracture surfaces and macroscopic features

A macroscopic analysis of fatigue fracture surfaces can reveal important facts about feedstock materials used such as orientations, dimensions, stress intensities, initiation sites and crack profiles. A fundamental approach can explain mechanisms of fracture such as the necessary energy and rupture modes during the fatigue-corrosion phenomenon. For instance, typical fatigue specimen failures normally show three distinct zones: 1) the crack nucleation stage, 2) the Benchmark crack growth stage and 3) the final rupture of the specimen. As explained in the literature section, *Corrosion forms 2.2.3*, pages 34 to 36, many publications *[21,35,36,37,38]* make reference to macrographs as typical rupture patterns with stress and notch effects on the fractured surfaces.

Fatigue S-N curves of forged feedstock materials exhibited two major cases where stress magnitudes (low and high) had a strong influence on the results. The low stress case values regrouped all specimens fractured under 100 MPa during the fatigue tests and the high stress cases were superior to this specific data. Macroscopic features of fatigue specimens in the fractured regions were taken by a JEOL scanning electron microscope at 25X magnification.

To create a standard for all pictures, the tops of each SEM sample were acquired as the milled surface and the bottoms as the forged surface for fatigue specimens *(Figure 4.60)*. This standard can relate the origin of initiation site(s).

```
┌─────────────────────┐      ┌───────────────────────────┐
│  Fractured fatigue  │ ───▶ │   Milled surface side     │
│  specimen surface   │      └───────────────────────────┘
│                     │      ┌───────────────────────────────┐
└─────────────────────┘ ───▶ │  Original forged surface (skin) │
                             └───────────────────────────────┘
```
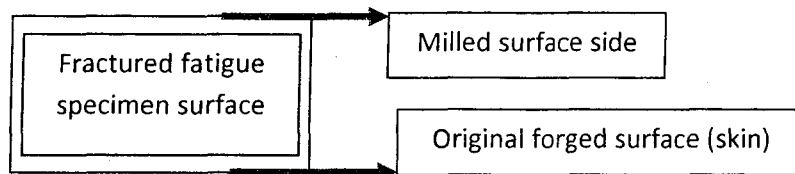
Figure 4.60: Fracture surface orientation to distinguish milled and forged surfaces on fatigue macrographs

The first case was analyzed for low fatigue stressed specimens with similar fatigue conditions. The SEM macrographs revealed some differences between fractured surfaces of cast and extruded-forged specimens. In *Figure 4.61*, flat and grainy facies of cast-forged samples were observed in contrary to irregular levels and important cleavage zones for the extruded-forged surfaces. Microstructural types and grain sizes might have important roles on the fracture mechanisms. Indeed, the "metallographical analyses of forged products" section revealed fine and elongated microstructures for the cast-forged materials against coarse and recrystallized grains for the extruded-forged conditions with T6.

The addition of a corrosive environment around the fatigue specimens did not change the rupture pattern of both deformed feedstock materials. As described above, these samples have three zones found typically on fatigue specimens. In an air environment, several initiation sites were identified near the sharp corners where the stress concentration factor was higher due to the specimen configuration *(Figures 4.61a and 4.61c)*. In a chloride corrosive environment, some fatigue samples revealed initiation sites in the center zone where corrosion pits were found for both forged materials *(Figures 4.61b and 4.61d)*.

a) **Cast-forged-T6 material with a low cyclic stress applied in an air environment**

b) **Cast-forged-T6 material with a low cyclic stress applied in a 3,5 w/v% NaCl environment**

c) **Extruded-forged-T6 material with a low cyclic stress applied in an air environment**

d) **Extruded-forged-T6 material with a low cyclic stress applied in a 3,5 w/v% NaCl environment**
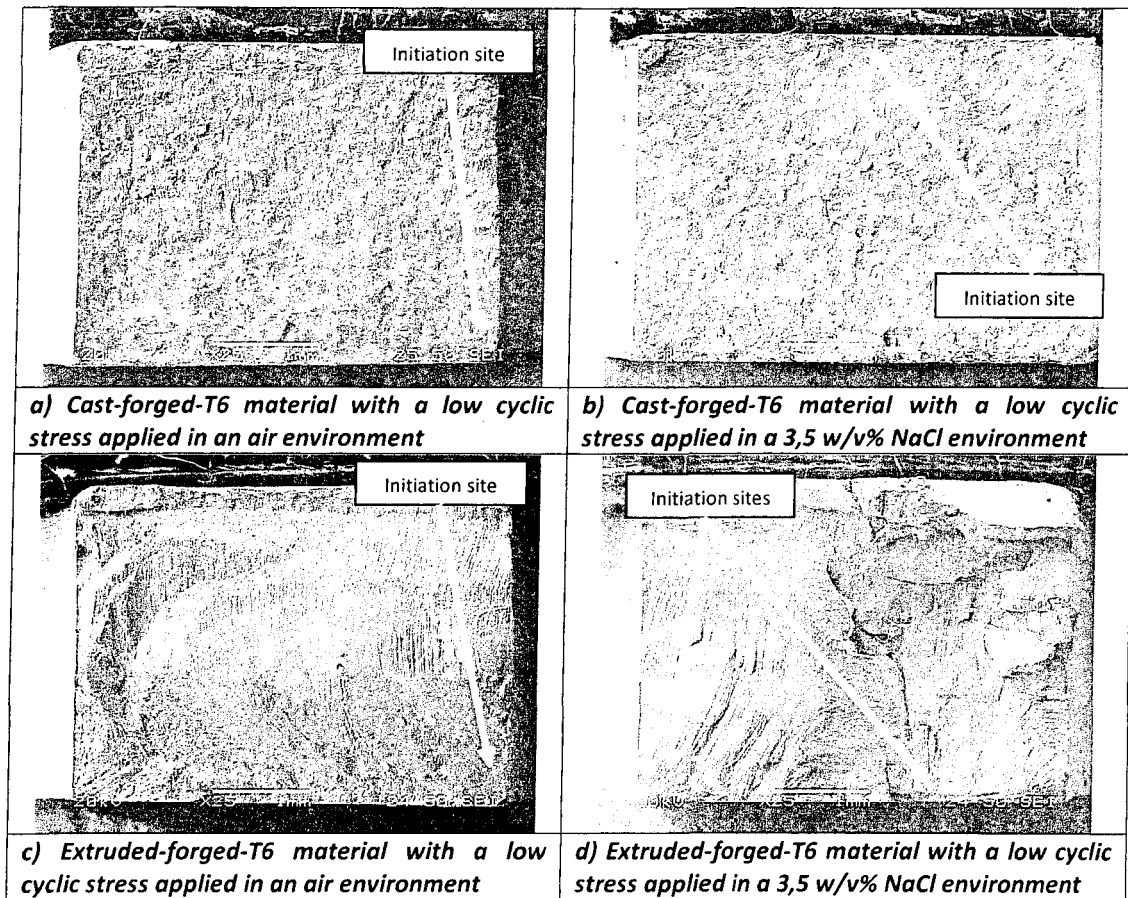
Figure 4.61: SEM macrofractographies of AA6082 forged-T6 materials with low fatigue stresses applied (≤

100 MPa) (25X magnification)

The second case described with high fatigue stresses applied (> 100 MPa) showed similar correlations with the "low fatigue stress case". The major crack growth path for the cast-forged-T6 material was still flat, rougher and perpendicular to the maximum tensile stress. At short crack lengths where the crack tip plastic zones were small, the crack path was usually flat. The extruded-forged-T6 fracture pattern showed brittle planes that turned to 45 degrees during the propagation stage and represented a shear mode failure.

With a high stress applied (≥ 100 MPa), the benchmark densities were significantly reduced on fracture patterns, and cracks lengths were longer during the propagation stage. For instance, cast-forged specimens revealed some important cracks that were not visible during the first case *(Figures 4.62a and 4.62b)*. Propagation and rupture zones increased as high fatigue stresses were applied and accelerated the crack growth rate. The final rupture zones were more considerable for the extruded-forged materials since this applied pressure was more difficult to retain *(Figures 4.62c and 4.62d)*.

a) Cast-forged-T6 material with high cyclic stress applied in an air environment	b) Cast-forged material with high cyclic stress applied in a 3,5 w/v% NaCl environment
c) Extruded-forged-T6 material with high cyclic stress applied in an air environment	d) Extruded-forged-T6 material with high cyclic stress applied in a 3,5 w/v% NaCl environment
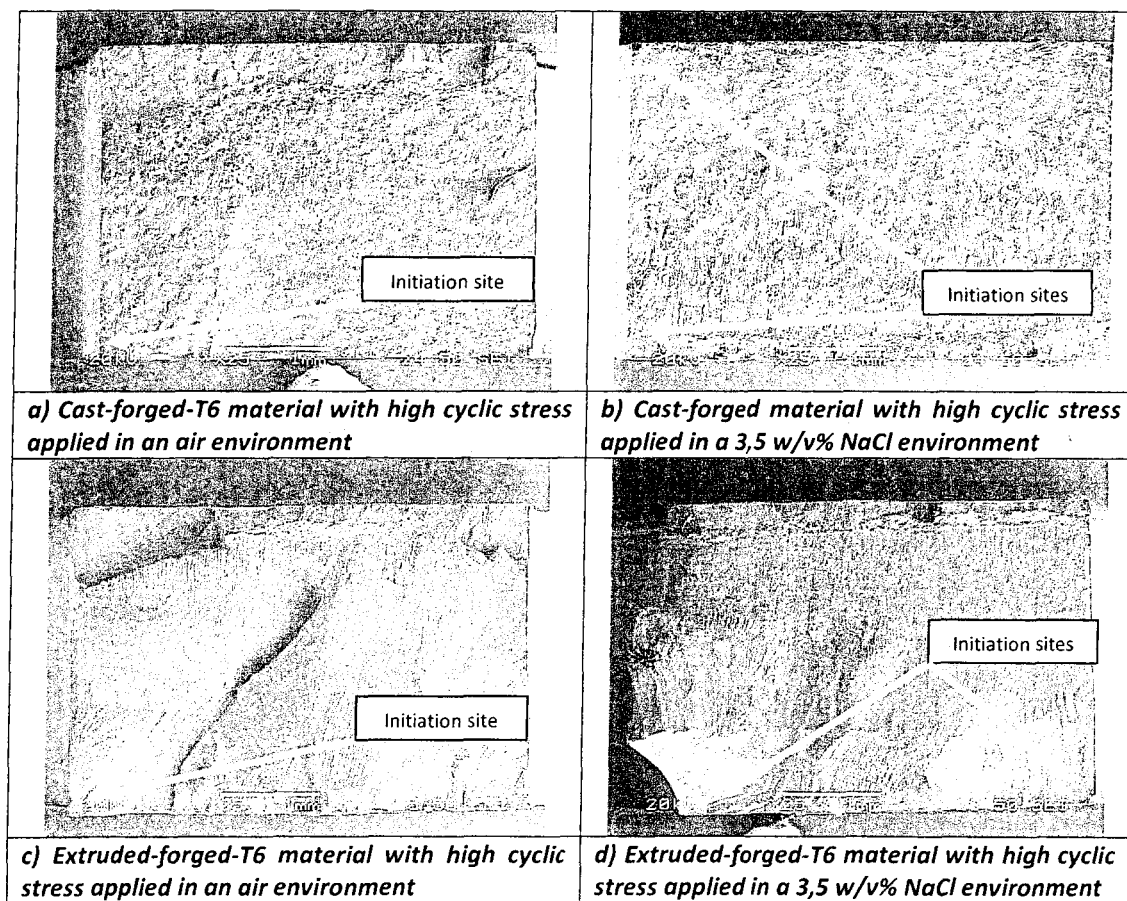
Figure 4.62: SEM macrofractographies of AA6082 forged-T6 materials with high fatigue stresses applied (≥ 100 MPa) (25X magnification)

4.5.4. Fatigue mechanisms and microscopic features

An electron microscopic analysis of fractured surfaces can reveal a wide range of fatigue crack information such as initiation mechanisms, propagation and rupture modes. The following paragraphs will treat these subjects individually.

- *Fatigue crack initiation*

Crack initiation is the major component of the fatigue performance. Therefore, identification of the crack locations and the nature of their origin site(s) is important. Some SEM pictures of fatigue specimens from origin sites were taken to understand the first stage of rupture initiation. *Figures 4.63a to 4.63d* present the main initiation sites for each condition tested.

As discussed in the macrofractograph section 4.5.3, crack initiation sites for both forged materials were identified near to sharp corners of samples in air medium for the low stresses applied. Microcracks called "ratchet marks", described in the literature section 2.2.3, Figure 2.29, page 37, were present at the surface of components that produced typically flat triangles in the corner of plate products *(Figures 4.63a, 4.63c and 4.63d).* These were essentially perpendicular to the surface from which the fatigue fracture originated and where a high local stress concentration had been applied. In a specific corrosive environment, both forged material showed the presence of corrosion pits during the initiation stage **(see arrows on Figures 4.63b and 4.63d)**. Fatigue specimens submitted to high cycling stresses showed similar crack initiation behaviours as described above.

a) Cast-forged-T6 material with a low cyclic stress applied in an air environment	b) Cast-forged-T6 material with a low cyclic stress applied in a 3,5 w/v% NaCl environment
c) Extruded-forged-T6 material with a low cyclic stress applied in an air environment	d) Extruded-forged-T6 with a low cyclic stress applied in a 3,5 w/v% NaCl environment
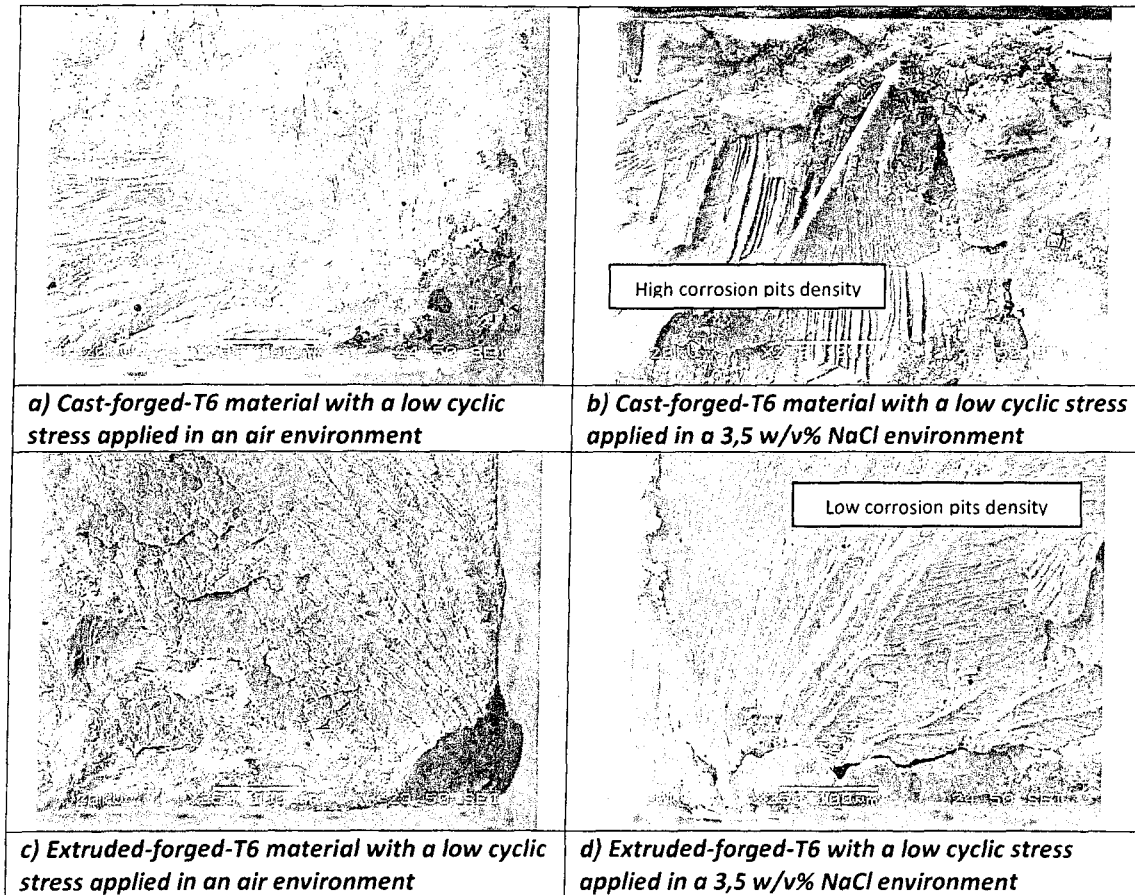
Figure 4.63: SEM microfractographies of crack initiation zones at low fatigue stresses applied (≤ 100 MPa) on AA6082 forged-T6 fatigue specimens (250X magnification)

However, the «cast-forged 3,5 w/v% NaCl» condition revealed important pits in the middle surface area with diameters of over 100 microns *(Figure 4.63b)*. These pits can act as stress raisers during the fatigue phenomenon to help nucleation of new cracks. Energy dispersive spectrometry detected the presence of AlFeSi constituents near the surface cracks *(Figure 4.64)*. This microgalvanic couple between the aluminum matrix and the AlFeSi constituent could intiate pits on cast-forged specimens.

Related to *Table 2.2*, the dissolution potential of the silicon ($\approx$ -0.17V) and iron phases ($\approx$ -0.47V) were more positive (noble) on the oxidation electrochemical scale and potential differences with the aluminum matrix were important ($\approx$0.75V). Therefore, microgalvanic couples between these elements were possible and could create pit initiations using this mechanism at the surface of cast feedstock materials.
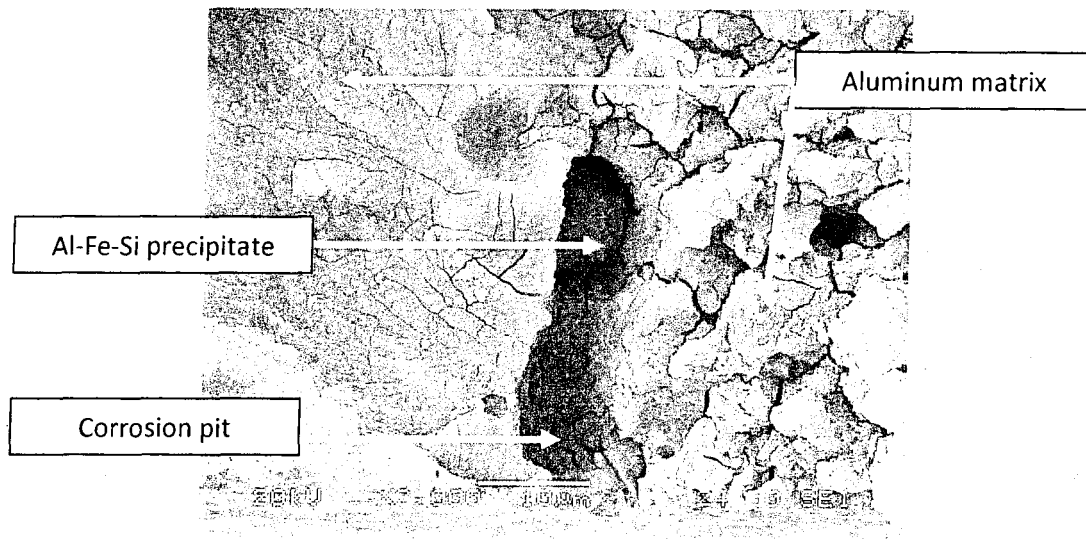
Figure 4.64: AA6082 cast-forged SEM microfractograph of an initiation site with a microgalvanic couple AlFeSi phase – Aluminum matrix (2000X magnification)

- *Fatigue crack propagation*

Progressive cycling growth of cracks had a significant area on broken fatigue specimens. Explanations on crack proliferations and their morphologies can be useful to understand their mechanisms and propagation stages. For instance, striation formation, microvoid coalescence and microclevage are three possible modes of crack propagations. All metallurgical conditions tested developed the same crack propagation mechanism of striation where persistent shear bands (PSB) called «intrusion-extrusion bands» were created *[21,35]*. All tested metallurgical conditions in fatigue seem to be affected especially in a corrosion medium where it had a grainy consistency *(Figure 4.65)*.

a) Cast-forged-T6 material with a low cyclic stress applied in an air environment	b) Cast-forged-T6 with a low cyclic stress applied in a 3,5 w/v% NaCl environment
c) Extruded-forged-T6 material with a low cyclic stress applied in an air environment	d) Extruded-forged-T6 material with a low cyclic stress applied in a 3,5 w/v% NaCl environment
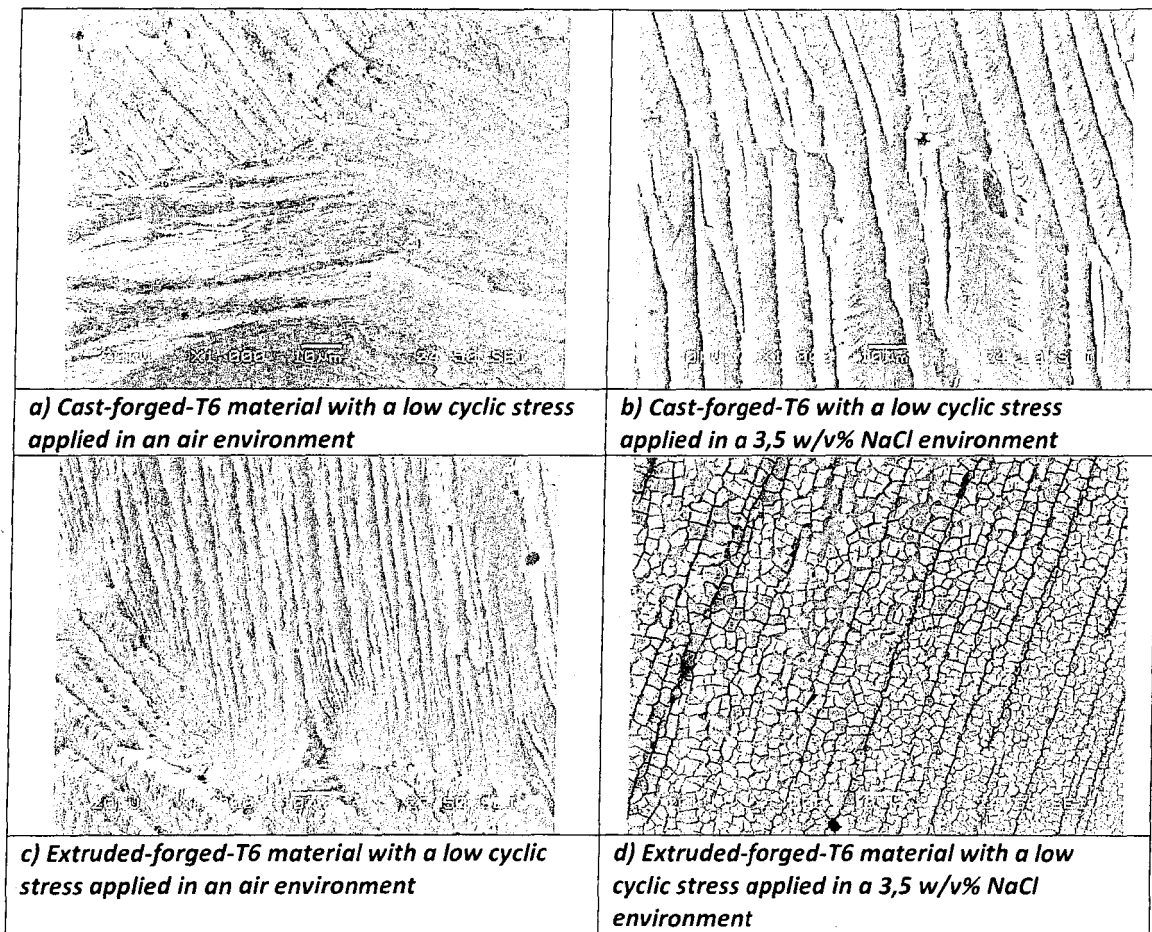
Figure 4.65: SEM microfractographies of crack propagation zones with low fatigue stresses (≤ 100 MPa) applied on AA6082 forged-T6 materials (Magnification at 1000X)

- *Final fatigue fracture appearance*

Fatigue fracture normally has a brittle and rougher appearance at small magnification due to severe and quick plastic deformations (similar to impact fractures). Low fatigue stresses will normally decrease the final overload area and vice-versa *(Figure 4.66)*. This rupture will occur when the last stress cycle cannot sustain the applied load by fatigue. In fact, a higher magnification imaging can exhibit different morphologies and characteristics than a brittle appearance.

In general, the area of fatigue fractured surface areas increased for all metallurgical conditions with higher stresses *(Figure 4.67)*. In particular, fatigue specimens with severe stresses demonstrated two zones into the fractured area: a ductile transition zone with dimples connected with the propagation zone and, a final brittle zone with a cleavage pattern and less deformation. For instance, *Figure 4.66a* illustrates these two possible zones which appear together in the fractured zone.

| Stress magnitude	Fatigue test specimens in an air medium	Fatigue test specimens in a 3,5 w/v% NaCl environment
Low cyclic stress cases (≤ 100 MPa)	a) Cast-forged-T6 material with a low cyclic stress	b) Cast-forged-T6 material with a low cyclic stress
	c) Condition Extruded-forged-T6 material with a low cyclic stress	d) Extruded-forged-T6 with a low cyclic stress
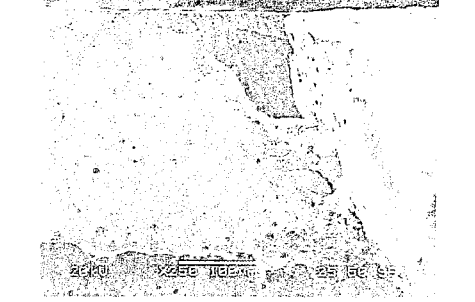
Figure 4.66: SEM microfractographies of fractured zones with low fatigue stresses applied on AA6082 forged-T6 materials (Magnification at 250X)
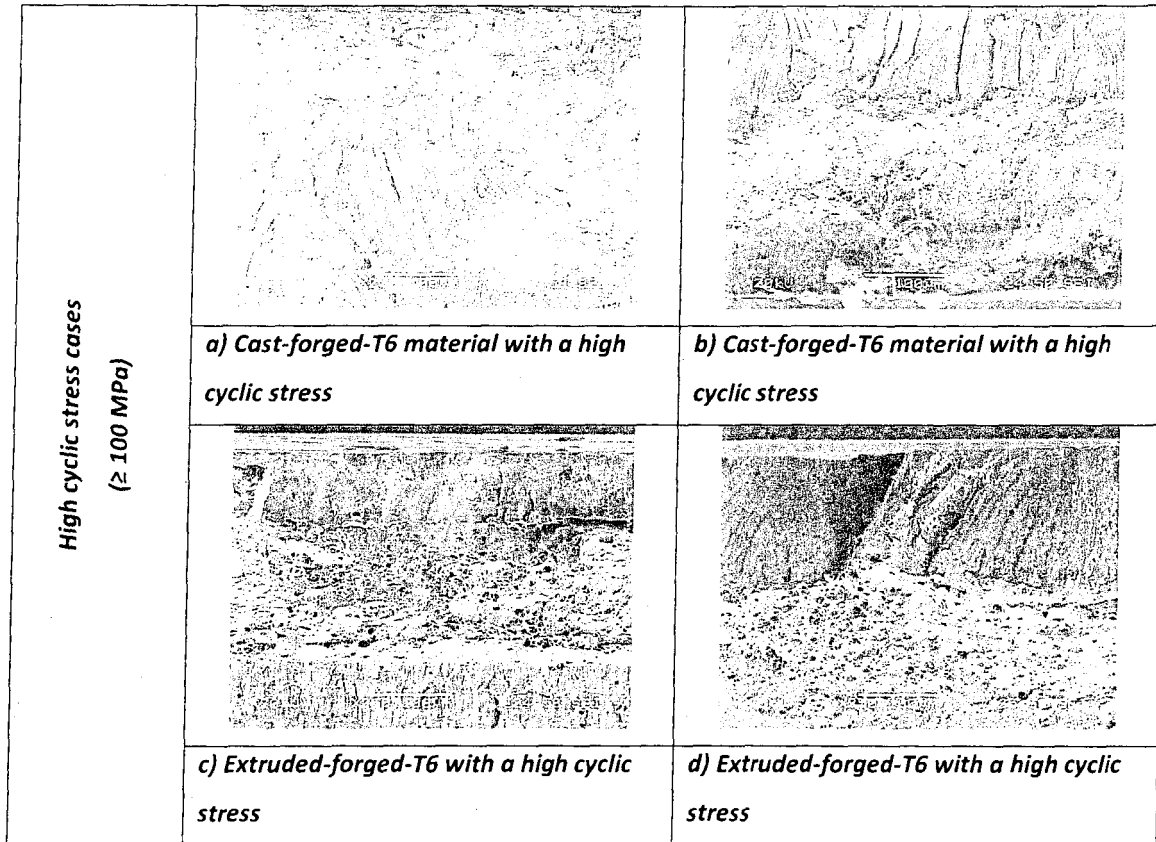
Figure 4.67: SEM microfractographies of fractured zones with high fatigue stresses applied on AA6082 forged-T6 materials (Magnification at 250X)

4.5.5. Comparative evaluation of reverse bending fatigue test results on forged-T6 products

Seven tendencies can be extracted from the fatigue test results.

i) The synergistic effect between a cyclic mechanical load and a corrosive medium has produced lower S-N results with a decreasing factor of 1000 versus "in an air environment". These results were identical for both forged materials.

ii) In the air environment, fatigue S-N curves established two cases for both forged materials: cast-forged material showed a better fatigue resistance at low stresses and the extruded-forged material revealed an improved fatigue resistance during high stress application.

iii) Macroscopic fatigue fracture analyses revealed flat and grainy facies of cast-forged samples in contrary to irregular levels and important cleavage zones for the extruded-forged surfaces *(Figures 4.61 and 4.62)*. This can be explained by crack propagation in tensile for the cast-forged material and tensile-shearing growth paths for the extruded-forged material. Microstructural types and grain sizes might have important roles on these crack propagation modes.

iv) The addition of a corrosive environment around the fatigue specimens did not change the propagation and rupture patterns of both deformed feedstock materials. In the same environment, some fatigue samples revealed initiation sites in the center zone where corrosion pits were found for both forged materials.

v) Microscopic fatigue fracture analyses showed that initiation sites were often near the sharp corners in the air medium. In a 3.5 w/v% NaCl solution, the «cast-forged-T6» condition revealed many corrosion pits on the surface compared to the extruded-forged-T6 material.

vi) All conditions seemed to have the same striation propagation mechanism with persistent shear bands (PSB). The texture of these bands seemed to be affected especially in a corrosion medium where a smooth surface was produced on extruded-forged striations inversely to coarse cast-forged striations.

vii) Fatigue specimens demonstrated two zones in the final fractured area: a ductile transition zone with dimples connected with the propagation zone and, a final brittle zone with a cleavage pattern and less deformation.

5.

CONCLUSIONS AND RECOMMANDATIONS

5.1. Conclusions

The goal of this work was to study the corrosion behaviour of AA6082 forging materials to evaluate their intrinsic corrosion susceptibility after forging. _**The main conclusion of this comparative study is that no significant difference in corrosion susceptibilities has been measured between the two forging feedstocks that could have a possible negative impact on the final product. Aluminum forged parts without a T6 heat treatment have a lower corrosion resistance than treated parts.**_

5.1.1. Characterization of AA6082 aluminum forging feedstock and forged materials

- Both microstructural feedstock analyses revealed specific microstructural features (structure patterns, grain sizes, intermetallic phases) for each cast and extruded materials that can have effects on the corrosion susceptibility, especially the presence of special layers at the surface. The cast material has an equiaxed grain structure with a surface layer rich in segregated alloying elements. Chemical analyses revealed α-AlFeSi, β-AlFeSi, Mg_2Si and eutectic silicon phases present in the inverse segregated regions. In contrast, the extruded material has a fibrous structure and a surface layer recrystallized with a fine grain structure. The Mg_2Si precipitates at extruded surfaces were all finely distributed in a high concentration, if compared with the bulk microstructure. This microstructural analyses put into perspective two materials that could have different affinities to the forging and corrosion assessment.

- The forged microstructures contain small Mg_2Si constituents at the grain boundaries with an elongated structure. Heat-treated with a solution and then artificially aged, the cast-forged materials produced a supersaturated solid solution that involved the formation of finely dispersed precipitates during this thermal process. The thermomechanically processed material from the initial extruded feedstock already had a fibrous macrostructure where the subsequent forging process contributed to amplify grain flattening and elongating tendencies. After the T6 heat treatment, the elongated texture generated by the forging step changed to a recrystallized fine microstructure for the cast feedstock. The following T6 temper affected the extruded-forged material by creating a regenerated microstructure with high dimensioned grain structures.

5.1.2. Corrosion tests

Corrosion tests were conducted on the AA6082 aluminum. Three tests show slight variations on the corrosion results but not enough to distinguish a better feedstock material.

- *Electrochemical tests:* The OCP curves showed that the time necessary for a passive state equilibrium of cast-forged material was longer than the extruded-forged material after a 24-hour immersion in a 3.5 w/v% NaCl solution. Similar anodic polarizations of impressed voltage permitted to identify E_{pit} between -0.63 to -0.54 V/SCE for all conditions. Cast feedstock conditions showed a continuous pitting phenomenon after E_{pit}. The cast feedstock T6 condition seemed to have a slightly better pitting resistance when the voltage was applied with the nobler E_{pit} result at -0.54 V/SCE.

Optical imaging analyses revealed uniform round corroded pit patterns for metallurgically cast-forged conditions. Also, extruded material showed an asymmetrical corrosion aspect with big corrosion spots similar to a metallurgical grain form.

- **Salt fog spray test:** Image analyses by CLEMEX on salt spray corroded specimens identified a better resistance of the extruded-forged material without subsequent solutionizing and aging heat treatments when compared with the same cast-forged condition (13.46% cast-forged-T6 vs 6.77% extruded-forged-T6). The T6 thermal treatments on both forged materials appear to have obtained the same percentage of area affected by the pitting corrosion (3.62% cast-forged-T6 vs 3.68% extruded-forged-T6) in the cabinet exposure test.

- **Fatigue-corrosion test:** The devastating effect of the addition of a corrosive environment during corrosion-fatigue resulted into a decrease in the number of cycles by a factor of $1x10^3$ on both types of forged-T6 materials. No significant variation in the corrosion-fatigue resistance was identified between the two types of materials. In an air environment, the S-N fatigue curves established two cases for both forged materials: the cast-forged material showed a better fatigue resistance at low stresses and, the extruded-forged material revealed an improved fatigue resistance during applied high stresses. The macroscopic fatigue fracture analyze revealed flat and grainy facies of cast-forged samples that differs to important cleavage zones found on the extruded-forged surfaces. Many fatigue specimens seemed to rupture with a striation propagation mechanism with persistent shear bands (PSB). The corrosion factor during the fatigue-corrosion tests had an impact on the softening of microscopic fatigue striations for both materials.

5.2. Recommendations

Based on corrosion susceptibility investigations conducted on two dedicated forging materials, some points remain to be intensified. The following recommendations allow understanding the subtleties of results.

- Assess the possibility to develop an efficient cleaning process on forged parts to remove residual lubricant graphite deposits without induced corrosion. Determine the corrosion susceptibility of this etched material with conventional corrosion tests and compare the results obtained.

- Perform additional electrochemical corrosion measurements to understand the divergence tendency of OCP results especially for the extruded-forged condition.

- Confirm the type and pit profiles for each forged material with metallographical analyses on salt spray corroded specimens. Establish a link between the horizontal pits found on the extruded-forged material with the PGL zone at the surface. Verify the exfoliation possibility on this material.

- Study and understand good fatigue resistances in air results for the extruded-forged with T6 material at high mechanical cyclic stresses.

- Evaluate the fatigue-corrosion behaviour of pre-corroded specimens to simulate a longer corrosion duration time. In the same field, explore the effect of anodic polarization on fatigue specimens during testing to accelerate the corrosion phenomenon.

- Obtain a general conclusion on the aluminum corrosion susceptibility of these feedstocks. Others aluminum series, particularly 2XXX and 7XXX series, where their corrosion susceptibility is poor due to important microgalvanic couples could be useful to validate these 6XXX series results.

REFERENCES

[1] W. Sterzl, *«Production of High Quality Forgings by Means of Cast Stock»*, Alcan Inc., International conference on Innovations in Metal Forming & ERC Reunion, Università degli Studi di Brescia, Italia, September 23rd-24th, 2004.

[2] Wagstaff inc., *AirSlip® Air Casting Technology, website http://www.wagstaff.com*

[3] Wagstaff Bob , Wagstaff news cast journal, *Advanced Technology for the Aluminum Casting Industry, Vol. 10 No. 2, April 2001,* page 1 of 6.

[4] Ma Qian, D.H. StJohn, S. Maloney and M.J. Couper. *As-Cast Microstructure in VDC Cast AA6082 Billet*, Material Science Forum, Vol 396-402, 2002, p. 191-196.

[5] D.G. Eskin, R. Nadella and L. Katgerman. *Effect of different grain structures on centerline macrosegregation during direct-chill casting*, Acta Materialia, 56, 2008, p. 1358-1365.

[6] R. Nadella, D.G. Eskin, Q. Du and L. Katgerman. *Macrosegregation in direct-chill casting of aluminum alloys*, Progress in Materials Science, 53, 2008, p. 421–480.

[7] Haug Einar, Hward J. Thevik. *Macrosegregation near a cast surface caused by exudation and solidification shrinkage*, Int J. of Heat Mass Tranfer, 1995,Vol. 38, No. 9, p. 1553-1563.

[8] M. Qian, J.A. Taylor, J.Y. Yao, M.J. Couper and D.H. StJohn, Journal of Light Metals, Vol 1, 2001, p. 187-193

[9] European Aluminum Association (EAA), TALAT, Chapter 3 Aluminum Machining and Forming, Section 3.5 Impact Extrusion of Aluminum, *3502 Impact Extrusion Processes*, 1999, 26 pages. http://www.eaa.net/eaa/education/TALAT/index.htm

[10] Pedersen, K.O. *Influence of texture and grain structure on strain localisation and formability for AlMgSi alloys*, journal of materials processing technology 200, Elsevier, (2008), pages 77–93.

[11] European Aluminum Association (EAA), TALAT, Chapter 3 Aluminum Machining and Forming, Section 3.4 Forging of Aluminum, *3401 - Forging Alloys*, 1999, 21 pages. http://www.eaa.net/eaa/education/TALAT/index.htm

[12] N.C.W. Kuijpers, W.H. Kool, S. van der Zwaag, Mater. Sci. Forum, 396-402, 2002, p. 675–680.

[13] S. Zajac, B. Bengtsson, Ch. Jonsson, Mater. Sci. Forum, 396-402, 2002, p. 399–404.

[14] N.C.W. Kuijpers, W.H. Kool, P.T.G. Koenis, K.E. Nilsen, I. Todd, S. van der Zwaag, Mater. Charact. 49, 2003, p. 409-420.

[15] Grazyna Mrowka-Nowotnik and Jan Sieniawski. *Influence of heat treatment on the microstructure and mechanical properties of 6005 and 6082 aluminum alloys*, Journal of Materials Processing Technology, 162-163, 2005, p. 367–372

[16] Vargel, Christian. *Corrosion of aluminum*, DUNOD, Paris, Industries et Techniques - Matériaux, 1999. 295 pages. ~

[17] Gaute Svenningsen, *Corrosion of Aluminum Alloys poster*, Norwegian Research Council and Hydro Aluminum, Department of Materials Technology, Norway, 1 page.

[18] Cast Nonferrous: *Stress Corrosion Cracking of Aluminum Alloys*, Key to Metals Databases, http://www.keytometals.com/Article17.htm

[19] Davis, J.R. *Corrosion of Aluminum and Aluminum alloys*. ASM international, 1999, p. 102-103.

[20] Elboujdaini M. and Ghali E. *Corrosion-fatigue of aluminum in chloride media*. Materials Science Forum, Vols. 44 – 45, 1989, p 153-168.

[21] Stephens, Ralph I. *Metal Fatigue in Engineering*, Wiley Interscience Publications, second edition, 2001, 472 pages.

[22] Wei, Robert. *Corrosion/Corrosion-Fatigue and Life-Cycle Management*. Material Science Research International, 2001, Vol. 7, No. 3, p. 147-156.

[23] G.S. Chen, M. Gao and R.P. Wei, Corrosion, 52, 1, 1996, p.8.

[24] Y. Kondo, Corrosion, 45, 1, 1989, p.7.

[25] Tokaji, Keiro and Goshima Yoji. J. Soc. Mat. Sci. Japan, 2002, Vol 51, No. 12, p. 1411-1416.

[26] Baboian, Robert. *Corrosion tests and standards*, ASTM manual series, ASTM International, 2005, p. 230.

[27] Stansbury, E.E. and Buchanan R.A. *Fundamentals of electrochemical corrosion*. The material information society ASM International, 2000, page 325.

[28] Danninger, Herbert. *Microstructural characterization*, Institute of Materials Physics, University of Vienna, 2000. http://www.univie.ac.at/hochleistungsmaterialien/mikrokrist/characterization.htm

[29] R.T. Foley, *Localized Corrosion of Aluminum alloys – A review*, Corrosion, Vol. 42, 1986, p. 277-288.

[30] G.C. Wood, W.H. Sutton, J.A. Richardson. T.N.K. Riley, and A. Malherbe. *The mechanism of pitting of aluminum and its alloys*, Localized corrosion NACE 3, National Association Corrosion Engineers, 1974, p. 526-539.

[31] M.F. Lopez and M.L. Escudero. *Corrosion behaviour of FeAl-type intermetallic compounds*. Electrochemica Acta, Vol. 43, No. 7, 1998, p. 671-678.

[32] Kiryl A. Yasakau, Mikhail L. Zheludkevich, *Role of intermetallic phases in localized corrosion of AA5083*, Electrochimica Acta 52, 2007, p. 7651–7659

[33] Rajan Ambat, Alison J. Davenport, GeoV M. Scamans, *Effect of iron-containing intermetallic particles on the corrosion behaviour of aluminum*, Corrosion Science 48 (2006) p. 3455–3471

[34] L.P. Borrego, L.M. Abreu, J.M. Costa, J.M. Ferreira, *Analysis of low cycle fatigue in AlMgSi aluminum alloys*, Engineering Failure Analysis, 11, 2004, p. 715-725

[35] Liu, Alan. *Mechanics and Mechanisms of fracture, an introduction*. The material information society ASM International, 2005, p. 133.

[36] G, Jacoby. *Fractographic methods in fatigue research*, Exp. Mech., Vol. 5, 1965, p. 65.

[37] N.W. Sachs, P.E. *Understanding the Surface Features of Fatigue Fractures: How They Describe the Failure Cause and the Failure History*. Journal of Failure Analysis and Prevention, The material information society ASM International, Volume 5(2), April 2005, p. 11-15.

[38] D.A., Meyn. Trans. ASTM, Vol 61. (No. 1), 1968, p. 52

[39] Princeton applied research, Electrochemical instruments division. *Applications notes: Electrochemistry and corrosion overview and techniques*, AMETECK Inc., 2004.
http://www.princetonappliedresearch.com/products/appnotes.cfm

[40] Cramer Stephen and Covino Bernard. *Evaluating corrosion-fatigue*, ASM International, ASM Handbook Volume 13A Corrosion fundamentals, testing and protection, 2003, page 625.

[41] T.W. Crooker, B.N.Leis , Corrosion-Fatigue, STP 801, ASTM, *Proceedings of the Symposium on Corrosion -Fatigue: Mechanics, Metallurgy, Electrochemistry, and Engineering held in St. Louis*, MO21-22 OCT. 1981, Philadelphia, PA., 1983

[42] ASM International. Volume 9, *Metallography and Microstructures, Aluminum solidification*. 2000, p. 373.

[43] LIEURADE, Henri-Paul. *Essais de fatigue-corrosion*. Encyclopedia of Techniques de l'ingénieur. Volume M135, 1998, 29 pages

[44] Organisation for International Standardization, *ISO 11782 – Corrosion of metals and alloys – Corrosion fatigue test part 1*, august 1998, 16 pages.

[45] N.G. Thompson and J.H. Payer. *Corrosion Testing Made Easy: DC Electrochemical Test* , NACE, 1998, 120 pages.